Photoactive Layer Modulation for High Performance Polymer and Perovskite Solar Cells

A dissertation submitted in partial fulfilment of requirements for the degree of

Doctor of Philosophy

by

Maimur Hossain

Roll No. 156122037

Department of Chemistry

Indian Institute of Technology Guwahati

Guwahati-781039, Assam, India

October 2021

Abstract

Multiple sources have been discovered and methods developed in quest of renewable energy to overcome the energy crisis and reduce carbon emission. Solar energy is considered as the most preeminent renewable energy source owing to the huge amount of energy supply from the sun to the earth. Among photovoltaic technologies, polymer solar cells and perovskite solar cells are one of the most promising due to their lower production cost and easy fabrication. Conjugated p-type copolymers are a key component in polymer solar cells as photon absorbers along with n-type acceptors. In recent time, perovskite has also emerged as efficient photovoltaic material due to its easy processibility and cost-effective nature like polymers ones. Due to the extensive research driven rapid growth in this class of new photovoltaic technology, in near future these may substitute its inorganic counterparts.

This thesis is broadly organized into two parts. The first part illustrates on the development of new terpolymers using third monomer incorporation to further advance the performance and ambient stability of polymer solar cells. The second part highlights the modulation of crystallization and mitigation of trap states in perovskite through additive engineering to achieve high efficiency, stability and reproducibility of perovskite solar cells. Firstly, with the aim to achieve high efficiency in the polymer solar cells and understand the structure property relationship, two terpolymers were synthesized by incorporating 2,5-difluorobenzene (FBZ) in popular PTB7-Th polymer backbone. The highest occupied molecular orbital (HOMO) was deepened for terpolymers with 5% and 10% FBZ containing M1 and M1′ polymers, respectively. As a result, the open circuit voltage (V_{OC}) was finely tuned for the terpolymers. The power conversion efficiency (PCE) was reached up to 8.78% (with V_{OC} = 0.85 V) for M1:$PC_{71}BM$ blend in comparison to 7.87% PCE for PTB7-Th:$PC_{71}BM$ blend (V_{OC} = 0.79 V) with device architecture of ITO/PEDOT:PSS/active layer/Cu. To further explore the impact of this method, By substituting 5% of 3-fluorothieno[3,4-b]-thiophene-2-carboxylate in the PTB7-Th backbone using monomers such as 2,5-difluorobenzene, 2,3-difluorobenzene, and 2,3,5,6-tetrafluorobenzene, random terpolymers M1, M2, and M3 were synthesized, respectively. The power conversion efficiency (PCE) for M1- and M2-based PSCs reached up to 9.48 and 8.80% from 8.19% for the PTB7-Th:$PC_{71}BM$ blend, respectively. However, M3-based blend exhibited an inferior PCE of 8.13% majorly due to its weaker absorption in the higher-wavelength region and lower carrier mobility. Moreover, the

fluoroarenes induced intra/intermolecular non-covalent interactions in blend films. These interactions acted as a conformational lock to tune the morphology that also improved the phase domain stability. M1:$PC_{71}BM$-based PSC displayed superior capability to sustain under ambient conditions and it retained 82% of its initial PCE after 1000 h of ambient exposure in comparison to 51% of the PTB7-Th blend under a relative humidity of 45 ± 5%.

Later, with the objective to modulate the crystallization process that could provide smooth perovskite films for stable and efficient photovoltaics, hydrophobic fluoroarene derivatives (4-fluoroaniline (FA), 2,4,6-trifluoroaniline (TFA), and 2,3,4,5,6-pentafluoroaniline (PFA)) were introduced on the perovskite surface. Among these fluorinated aromatic amines, PFA most proficiently improved the efficiency along with the moisture and thermo-stability of $MAPbI_3$ based PVSCs. PFA significantly passivated the defects and assisted better charge transport in the devices. The power conversion efficiency (PCE) was enhanced beyond 20% for the PFA passivated device, compared to the 15.08% of the pristine device without any passivation. Moreover, the PFA passivated device retained up to 87% PCE, compared to 26% for the pristine device when exposed to relative humidity ~50% for 1000 h. Further, a multifunctional passivation additive, 5-fluoropyrimidine-2,4(1H,3H)-dione (FPD), widely used as a cancer drug, was incorporated into the perovskite-based photoactive layer to enhance its photovoltaic efficiency along with its ambient stability. When this biologically active cancer drug molecule was utilized as a passivation additive, significant improvement was achieved in all the photovoltaic parameters, which collectively contributed to the enhancement of photovoltaic efficiency. The efficiency of PVSCs was elevated up to 20.22% for the FPD-passivated devices from 15.10% for the pristine device without any passivation. Furthermore, the incorporation of FPD also improved the long term durability of PVSCs by suppressing defects and enhancing the hydrophobicity of the perovskite surface. The FPD-passivated device maintained the PCE up to 89% in comparison to 27% for the pristine devices when PVSCs were exposed to a relative humidity of ~50% for 1000 h.

The efforts made in this thesis highlights the utility of polymer backbone engineering as well as additive engineering of perovskites and provides the basis for facilitating the commercialization of polymer and perovskite solar cells in the near future.

Dedicated to My Parents

Statement

I do hereby declare that the work incorporated in this thesis entitled, "**Photoactive Layer Modulation for High Performance Polymer and Perovskite Solar Cells**" is the result of investigations carried out by me under the guidance of Prof. Parameswar Krishnan Iyer, Department of Chemistry, Indian Institute of Technology Guwahati, Guwahati, Assam, India.

In keeping with the general practice of reporting scientific observations, due acknowledgements have been made wherever the work described is based on the findings of other investigators. I further declare that this work has not been submitted in part or full to any other university or institute for award of any degree or diploma.

IIT Guwahati **Maimur Hossain**

October 2021

Dr. Parameswar K. Iyer
Professor, Department of Chemistry and
Center for Nanotechnology
Indian Institute of Technology Guwahati
Guwahati-781039, Assam, India
http://www.iitg.ac.in/chemistry/fac/pki/

Phone : +91-361-2582314
Fax : +91-361-2690762
:+91-361-2582349
E-mail : pki@iitg.ac.in

Certificate

This is to certify that the work included in this thesis entitled "**Photoactive Layer Modulation for High Performance Polymer and Perovskite Solar Cells**" by Mr. Maimur Hossain, Department of Chemistry, Indian Institute of Technology Guwahati has been carried out under my supervision. I further certify that this work has not been submitted to any other University or Institution in part or full for the award of any degree or diploma.

IIT Guwahati

September, 2021

Prof. Parameswar Krishnan Iyer

Thesis supervisor
Department of Chemistry
Indian Institute of Technology
Guwahati, Guwahati – 781039, Assam, India

Acknowledgements

I feel delighted to express my sincere appreciation and gratitude to those who have contributed to this thesis and assisted me in one way or the other during this truly unforgettable and overwhelming journey. It is really hard to list all who sincerely assisted me, and I would like to thank all of them who have made this thesis possible.

First of all, I am extremely grateful to my supervisor Prof. Parameswar K. Iyer for providing me a great opportunity to work in his group. His constant support, scientific guidance, insights, patience and impetus encouraged me to take up the tasks that otherwise were difficult and demanding. I sincerely thank him for having trust in me and giving me total freedom in choosing the dimension of my research. I feel privileged to having him as my mentor who always motivated me with his hard work, dedication and buoyancy.

Besides my supervisor, I am highly indebted to my doctoral committee members, Prof. Aditya Narayan Panda, Dr. Kalyan Raidongia, and Dr. Uday Narayan Maiti for assessing my research work regularly. Their insightful advices, suggestions and crucial comments helped me to widen my research from various perspectives and improve my thesis.

I am also thankful to all the researchers and the staff of the Department of Chemistry, Center for nanotechnology, Central Instrument Facility, IIT Guwahati for their kind cooperation and support. I am indebted to the staff of student affairs, academic affairs and finance sections of IIT Guwahati for being kind enough to advise and help in their respective roles. My special thanks to Debasish (from Tezpur), Ritesh, and Ankur for their assistance to analyze different samples.

Without an iota of doubt, my research team deserves the best and utmost respect for their hard work, diligence and indispensable input into the overall research work. I would like to thank Adil bhai, Ritesh, Rabindra, Rahul bhai, Chandan, and Mayur. I would like to thank all my past and present labmates Priyanka di, Himani di, Ekta di, Radha bhaiya, Bhim bhaiya, Suresh bhaiya, Anamika di, Ashish bhaiya, Sameer bhai, Akhtar bhai, Arvin bhai, Sayan da, Dipjyoti bhai, Anamika Kalita di, Gopi bhai, Niranjan bhai, Rahul bhai, Raman bhai, Indrani, Subrata, Ramesh ji, Debasish, Rabindra, Chandan, Nehal, Ritesh, Retwik, Anwesha, Nasima, Biki, Anita, Kavita, Rajdikshit, Paromita, Muzaffer bhai, Tamal, Priyam, Debika, Soumalya, Sayantani, Hirak, Mayur, Sushant, Atonu, Himangshu, and Dibash for their timely help and support. I

would also like to thank them for creating a pleasant and vibrant laboratory atmosphere and making my days memorable. I especially thank Adil bhaiya, Rahul bhai, and Akhtar bhaiya for sharing their enormously broad knowledge and showing endless patience. They taught me all the basics, experiments and techniques that were needed.

I extend my sincere thanks to my friends Tousif, Atikur, Papai, Imran, Habibur, Pritam, Talha, Hasan, Rukhsar, Huzaifa, Anam, Sanavil, Furqan bhai, Abid, Suhail bhai, Shahab bhai, Aslam, Alim, Saddam, Ishtiyak, and other friends for their constant unfailing support, their encouragement and all the help they extended whenever required.

My sincere thanks to Dr. Sameer Hussain, Dr. Adil, Dr. Rahul, and Dr. M Shaad Ansari for their brotherly caring nature, sharing all kinds of moments and helping to improve my thinking approach.

I sincerely express my gratitude towards entire fraternity from my school and university especially Mir Mainul Hoque Sir, Mrs. Shamsun Nahar Ma'am, Prof. Aminul Islam, and Prof. Suhail Sabir Sir for imbibing good values and knowledge in me.

A special thanks to all my seniors and juniors from AMU; Palash da, Ajaz bhai, Sameer bhai, Akhtar bhai, Sahnawaz bhai, Wajid bhai, Kripa bhai, Zia bhai, Shaad bhai, Kafeel bhai, Mahboob bhai, Adil Rather, Akhtar Alam, Munendra, Suhaib bhai, Shavez bhai, Nehal, Saghir bhai, Tipu, Altaf, Tarik, and Masud for giving me unforgettable moments and delightful experiences.

I am really thankful to my wife, Mary Najmin Akter for her constant support and assistance during this long journey of research. My Ph.D. journey could not have been completed without the endless love, support, tolerance and blessings from my family. I am fortunate and blessed enough to have such a caring and supportive parents and younger brother, meherab. It is because of their prayers, sacrifice and struggle; I am able to live my dream to complete my higher education from a prestigious institute. I am also grateful to my sisters and brother for their eternal love, cooperation and emotional support which had immensely needed to complete this work. Finally, I thank almighty Allah for giving me a healthy life, strength to pursuit my dreams, and being with me in all my failure and success!

Maimur Hossain

Table of Contents

Abbreviations

2D	Two-dimensional
3D	Three-dimensional
AFM	Atomic force microscopy
Ag	Silver
CB	Conduction band
CdSe	Cadmium selenide
CdTe	Cadmium teluride
CIGS	Cadmium Indium Gallium Sulfide
CPE	Constant phase element
CV	Cyclic voltammetry
DCA	Deoxycholic Acid
DCM	Dichloromethane
DFT	Density functional theory
DMF	N,N-dimethylformamide
DMSO	Dimethylsulfoxide
DOS	Density of state
DSSC	Dye sensitizes solar cell
EIS	Electrochemical impedance spectroscopy
ETL	Electron transporting layer
eV	Electrovolt
FA	Formamidinium
FA	4-fluoroaniline
FBZ	2,5-difluorobenzene
FESEM	Field Emission Scanning Electron Microscope
FF	Fill factor
FPD	5-fluoropyrimidine-2,4(1H,3H)-dione
FTIR	Fourier-transform infrared spectroscopy
FTO	Fluorine-doped tin oxide, SnO2:F
GBL	Gamma butyrolactone
h	Hours
HOMO	Highest occupied molecular orbital
HRMS	High resolution mass spectrometry
HTL	Hole transporting layer
Hz	Heartz
ICT	Intramolecular charge transfer
ITO	Tin-doped indium oxide
LUMO	Lowest unoccupied molecular orbital
M	Molar
MA	Methylammonium
mA	milliampere
mg	milligram
mV	millivolt
mW	milliwatt

NBS	N-Bromosuccinimide
NiOx	Nickel oxide
NIR	Near infrared
nm	nanometer
NMR	Nuclear magnetic resonance
NREL	National renewable energy laboratory
ns	nanosecond
OLED	Organic light emitting diode
$PC_{61}BM$	[6,6]-Phenyl-C61- methyl ester
$PC_{71}BM$	[6,6]-Phenyl-C71- methyl ester
PCE	Power conversion efficiency
PEDOT:PSS	Poly(3,4-ethylenedioxythiophene)-poly(styrenesulfonate)
PFA	2,3,4,5,6-pentafluoroaniline
PL	Photoluminescence
PSC	Perovskite solar cell
Pt	Platinum
RMS	Root mean square
s	second
SEM	Scanning electron microscope
SSC	Steady state current
TCO	Transparent conducting oxide
TFA	2,4,6-trifluoroaniline
TFT	Thin film transistor
THF	Tetrahydrofuran
TiO_2	Titanium dioxide
TMTA	Trimethylolpropanetriacrylate
UV-Vis	Ultraviolet visible
V	Volt
v/v	Volume/volume
X	Halogen
XRD	X-ray diffraction
ZnO	Zinc oxide
µm	micrometer
Ω	Ohm

List of Figures

List of Tables

Chapter 1

Introduction

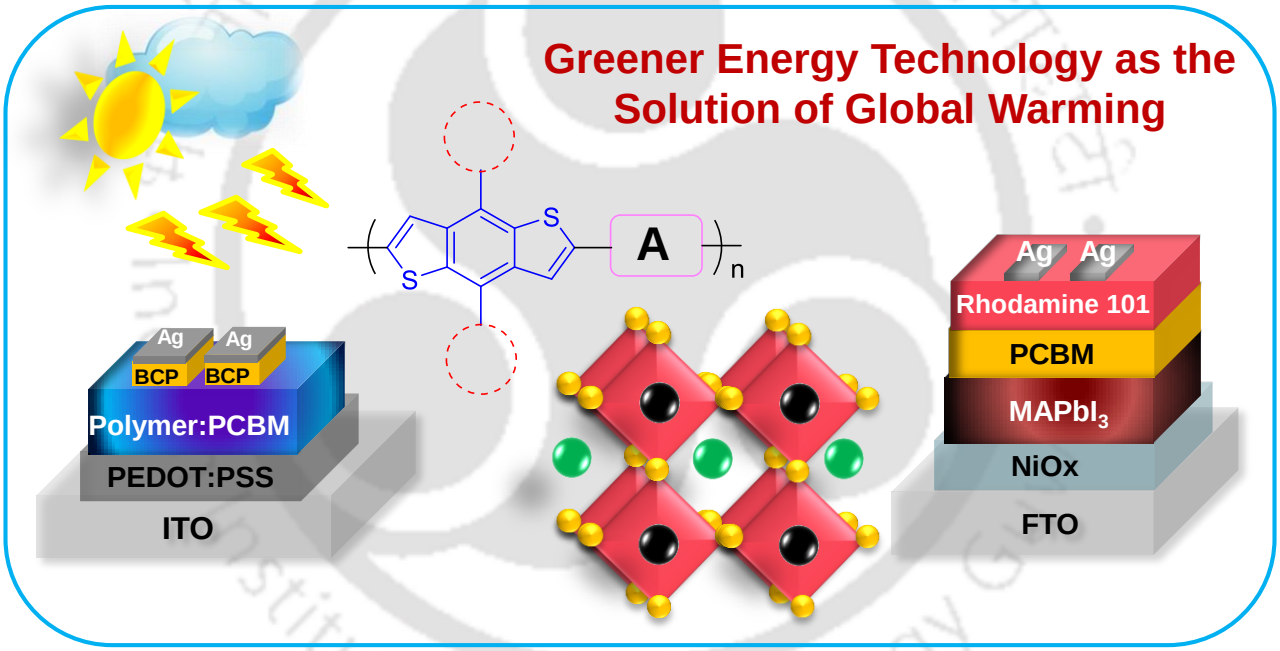

Abstract

Energy is a very important resource for our daily needs and economic activities. The natural energy resources are divided in two types viz., i) primary and ii) secondary. The fuels which generate energy in its raw form (without undergoing any conversion process) are termed as primary, e.g. fuel wood, coal, and natural gas. Secondary energy like petrol and electricity is made from the processing of primary fuels. The energy sources are further classified as non-renewable and renewable energy. The non-renewable energy sources like coal, petroleum and gas generally produces hazardous residues after its utilization. Contrarily, the energy sources like tidal, wind, and solar are considered as renewable due to its eco-friendly qualities. In the past two decades, the demand for energy in India is increasing exponentially due to rapidly growing economic activities like manufacturing, transportation, and other services. Therefore, the sustainable and eco-friendly energy technologies are attaining huge research attention to cope up with the demand of green energy. Hence, this chapter elaborates the development of technologies to generate renewable and green energy i.e., solar energy. In addition, the methods, materials, device architectures of polymer and perovskite solar cells were briefly discussed along with its varied measurement techniques. Further, a description about the engineering of polymer and perovskite materials is also presented. Finally, the chapter ends with a synopsis of this thesis.

1.1 Introduction

Rapid industrialization and growing economic activities have accelerated the energy consumptions globally. Till now, the cheap conventional energy sources like fossil fuels have somehow fulfilled the energy appetite of the modern world.[1] However, the adverse impacts of these polluting energy sources results in rising global warming at an alarming rate.[2] This has emerged as the prime concern for human society which has also built a global consensus to promote alternative energy sources like wind, hydropower, geothermal, biomass, and solar energy. These eco-friendly options offer efficient and economical alternatives of fossil fuels. Among these sources, solar technology has emerged as the most preeminent and sustainable choice which has the potential to cope up with the global demands. Enormous amount of energy falls on the earth as sunlight i.e., 3×10^{24} joule/year which is equivalent to ten thousand times more than what human society consumes every year. Consequently, solar technology is considered to be one of the best sustainable options for next generations.[3] Inorganic materials

(monocrystalline & polycrystalline silicon based, CdTe and CIGS based thin film technologies) based photovoltaics are dominant among commercially available ones.[4,5] However, the methods involved in fabrication of this class of solar technology are sophisticated, costly and requires high energy. Contrarily, the photovoltaic technologies like polymer solar cells (PSCs) and perovskite solar cells (PVSCs) are distinctively advantageous in comparison to silicon based inorganic solar cells. The different constituting layers involved in these solar cells can be modified to tune the photovoltaic efficiency of solar cells. The structural modifications of photoactive layer, electron transport layers (ETLs), hole transporting layers (HTLs) and interfacial layer can be used as a tool to enhance the power conversion efficiency (PCE) and stability.[6-8] Subsequently, the emergence of these new photovoltaic technologies has gained extensive research attention globally due to their unique advantages like easy processibility, cost effective, transparency, flexibility, color tunability, lighter weight, and relatively short energy payback time. The recent advancement of PSCs and PVSCs has challenged the dominance of commercially available inorganic counterparts.[9]

1.2 Polymer and Perovskite Solar Cells

PSCs have gained immense research attention due to its incredible qualities like easy fabrication method utilizing the cost effective solution processibility, semi-transparent, light-weight, flexible.[6,7] Recently, the PSCs achieved the PCE beyond 18% which has made it one of the potential technologies to challenge the dominance of inorganic counterpart.[10] The working principle of PSC involves multiple steps to convert the solar energy into electrical energy: i) absorption of photons, ii) exciton generation iii) diffusion of excitons at the interface of donor-acceptor (D-A), iv) polaron formation, v) charge dissociation, and vi) charge transport and collection.[11] A substantial loss in the photocurrents and photovoltaic efficiency occurs in the process of exciton generations, its diffusion and in charge carrier transport. These obstacles were overcome by the utilization of bulk heterojunction (BHJ) method in PSCs in which a blend is utilized as the photoactive layer with a particular D-A ratio.[12] This facilitated the mitigation of exciton recombination loss as domain sizes of the D and A materials reduced considerably. Further, the contact area between the D and A also enhances facilitating more excitons to dissociate into holes and electrons. In last decade, numerous materials were developed to be

utilized as D and A.[13] Properly matched energy band alignment, wide absorption range, and molecular planarity are some of the key factors to obtain high-performance PSCs.

Perovskite materials based on organometal halides have emerged as the most prominent light absorbing material for solar cells in the last decade. As a photon absorbing layer, perovskite materials satisfy almost every criteria to match performance of the silicon based inorganic solar cells. By motivating to develop more efficient light absorbers, Miyasaka and co-workers first developed perovskite-sensitized solar cells from 2006 to 2008.[14,15] $CH_3NH_3PbI_3$ and $CH_3NH_3PbBr_3$ were used as active layer with iodide/triiodide redox couple or a polypyrrole carbon black composite based hole conductor. The highest efficiency of 2% was achieved with these photovoltaic devices. Further, in a liquid-based dye-sensitized solar cells, the adsorption of $CH_3NH_3PbX_3$ (X= Br^-/I^-) perovskite on nano-crystalline TiO_2 achieved PCE of ~3–4%.[16] However, due to the instability of the liquid-based PVSCs, it did not receive much attention. To overcome the instability issue of these primitive PVSCs, solid hole conductor (*spiro*-MeOTAD) was introduced replacing liquid electrolyte.[17] The PCE reached >9% for this *spiro*-MeOTAD based PVSCs. Further, a non-sensitized PVSC was introduced in which mixed halide perovskite was utilized with mesoporous Al_2O_3 film and the PCE reached ~11%.[18] This class of PVSCs paved the way for rapid growth in research to develop stable and highly efficient solar cells for next generation. Since then, PVSCs have witnessed multi-fold rise in PCE which is assisted by continuous molecular and device engineering.

1.3 Device Architecture and Working Principle

1.3.1 Polymer Solar Cells

Conventional and inverted architecture are most explored choice to fabricate the PSCs which is presented in Figure 1.1 In the conventional architecture (Figure 1.1a), the layer stack is commonly deposited on indium tin oxide (ITO) coated substrate followed by a hole transport layer (HTL) poly(3,4-ethylenedioxythiophene):poly(styrene sulfonate) (PEDOT:PSS) and a photoactive layer. In this class of solar cells, a blend of donor and acceptors are used in optimum ratio to obtain the photoactive layer. Then, an electron transport layer (ETL) and metal electrode like Aluminum (as cathode with low work function) is usually deposited sequentially. In the

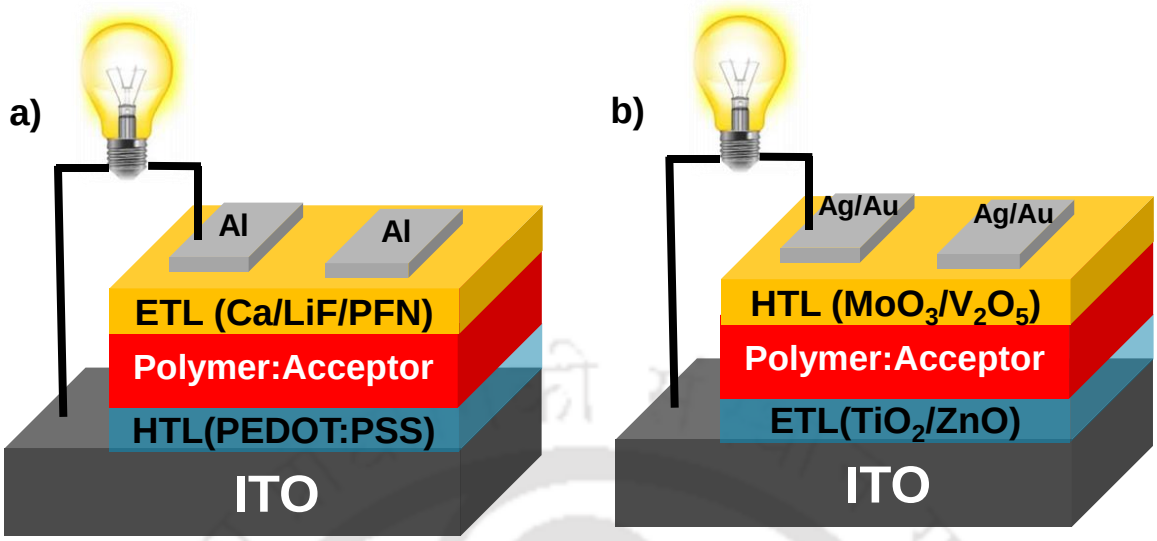

Figure 1.1: Device architecture of PSCs a) conventional and b) inverted.

inverted type of architecture (Figure 1.1b), the top metal electrode acts as a hole-collecting anode.

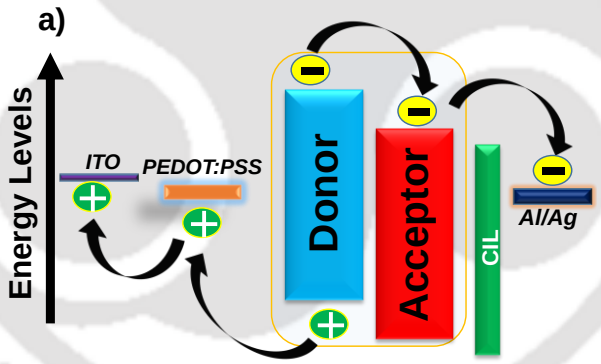

Figure 1.2: Schematic illustration of transport mechanism in PSCs**.**

ZnO and TiO_2 are most widely explored ETL to be utilized between ITO and the photoactive layer of inverted PSCs.[19] In inverted type device geometry, higher work function metals such as silver or gold are utilized. The charge transport mechanism of PSCs is presented in Figure 1.2.

1.3.2 Perovskite Solar Cells

Mesoscopic and planar heterojunction structure are most commonly utilized architecture for single junction PVSCs (Figure 1.3). In mesoscopic structure, perovskite infiltrates into a mesoporous metal oxide scaffold (Figure 1.3a).[18]

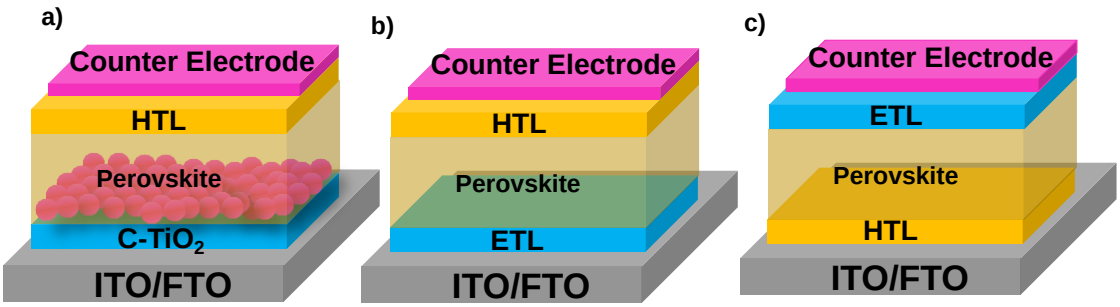

Figure 1.3: Device architectures of PVSCs a) mesoporous n-i-p, b) planar (n–i–p), and c) planar (p–i–n).

Moreover, to take benefit of ambipolar quality of perovskites, a planar configuration is also utilized. The planar devices can be fabricated by following (n-i-p)/inverted (p-i-n) configuration, depending on the type of contact (n-type or the p-type, respectively) incorporated towards the transparent electrode (Figure 1.3b-c).[20-21]

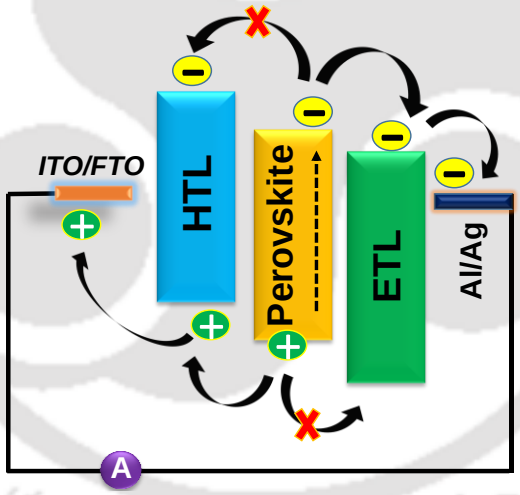

Figure 1.4: Schematic illustration of PVSC transport mechanism**.**

A PVSC is made of five layers, i.e. 1) transparent conducting oxide (TCO) 2) electron transporting layer (ETL), 3) perovskite active layer, (4) hole transporting layer (HTL), and 5) the counter electrode. The charge carrier transport operation of both the planar and mesoscopic PVSCs follow similar charge transfer mechanism. Firstly, the photoexcitation of perovskite layer by sunlight generates electrons and holes in active layer (Figure 1.4). Then, the electrons migrate towards the LUMO of ETL or conduction band. The holes are injected into the valance band or

highest occupied molecular orbital (HOMO) of HTL. Then, charge carriers move towards their respective electrode. Longer diffusion length of perovskite materials assists the efficient flow of charge carrier in PVSCs. However, the charge carrier recombination at the interface of different layers and grain boundaries can adversely impact the performance of the PVSCs. This harmful recombination can be minimized by device and active layer engineering. Defects suppression and modulation of active layer grain size can be effective in mitigating the charge carrier recombination.

1.4 Constituents of Polymer and Perovskite Solar Cells

1.4.1 Transparent Conducting Electrode

The PSCs and PVSCs are commonly fabricated on a transparent conducting substrates i.e. fluorine-doped tin oxide (SnO_2:F, FTO) or tin-doped indium oxide (ITO), which is deposited on a plastic or glass substrate. Due to its transparent nature, it allows maximum photons to reach the photoactive layer and its conductive quality assists the charge transport. ITO was utilized for all PSCs and FTO was used for all PVSCs here. Both the TCOs are mechanically robust, chemically inert, and display resistance to high temperature. These cost effective conducting oxides possess high abrasion resistance, lower absorption and reflection.

1.4.2 Electron Transporting Layer (ETL)

Electron transporting layer (ETL) has an important role in extracting and transporting the electrons in the device. It can also align the interfacial energy level which can mitigate the recombination of electrons and holes. Moreover, the ETL layer also acts as hole blocking layer. [6,6]-Phenyl-C61-methyl ester ($PC_{61}BM$) has been used as ETL for PVSC fabrication as it is one of the most widely utilized ETL in inverted PVSCs.[22]

1.4.3 Active Layer

The photoactive layer of a solar cell is the most important component which absorbs the photons and initiates the entire process of electricity production. The blend of various p-type donor polymers with n-type fullerene derivatives ($PC_{61}BM$ or $PC_{71}BM$) or newly developed non-fullerene acceptors (NFAs) were usually extensively explored for the PSCs. In this thesis, the structural modification in polymer backbone was utilized as a tool to tune the opto-electronic

property of polymers. On the other hand, in PVSCs, generally different perovskite materials are utilized as photoactive layer. However, to improve the PCE and durability of PVSCs, incorporation of additives are utilized to suppress the defect states and improve the film quality of perovskite active layer.

1.4.4 Hole Transporting Layer

The hole transporting layer (HTL) is utilized in PSCs and PVSCs to extract the holes and transport to the electrode. It also blocks the electrons to recombine with holes. The HTL should have high mobility ($>10^{-3}$ cm^2 $v^{-1}s^{-1}$).[23] Poly(3,4-ethylenedioxythiophene) poly(styrenesulfonate) (PEDOT:PSS) was used as HTL for first two works on PSCs (Chapter 2 and 3). However, for last two chapters (chapter 4 and 5) Nickel oxide (NiOx) was used as a cost effective HTL and relatively more efficient alternative for PVSCs.

1.4.5 Metal Electrode

As a back contact, the metal electrode completes the electrical circuit of a solar cell. It also provides voltage and current for the external electrical work. Generally, Al, Ag or Au are commonly used as counter electrode of PSCs and PVSCs. By thermal evaporation, the metal electrodes are deposited. The metal should possess optimum work function level to facilitate efficient charge transport. Moreover, interfacial layers are often utilized in both PSCs and PVSCs in order to modulate the work function level of metal electrode and improve the charge transport in the device.

1.5 Device Measurements

1.5.1 *J-V* Characterization

To estimate the efficiency of a photovoltaic device, the current density-voltage (*J-V*) measurement is one of the most important methods. The *J-V* measurements are conducted by illuminating the photovoltaic device under standard AM 1.5G illumination (=1 Sun illumination). To obtain *J-V* profile, the current density is recorded by sweeping the voltage across electrodes as shown in Figure 1.5. Following parameters are determined from the *J-V* profile:

Short circuit current density (Jsc)

J_{SC} is obtained from the *J-V* profile at short circuit condition. The J_{SC} value directly depends on the absorption properties, bandgap of active materials (polymer donor, acceptor and perovskite layer), charge transportation and collection in the photovoltaic device (Figure 1.5).

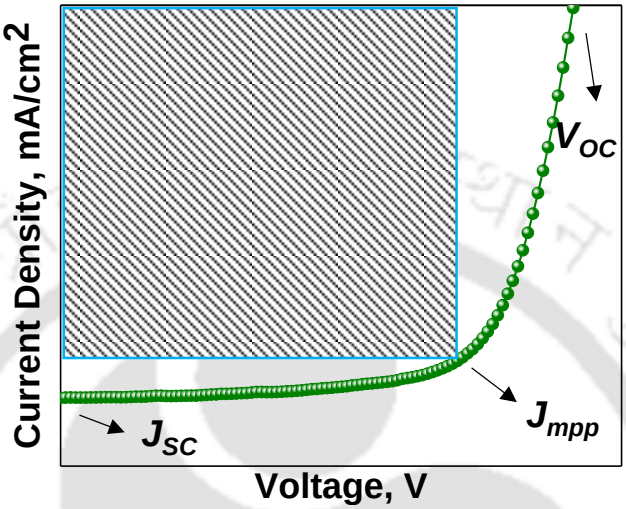

Figure 1.5: An example of standard *J-V* graph.

Open circuit voltage (Voc)

V_{OC} is estimated as the potential in the open circuit condition when no current flows in the electrical circuit. V_{OC} depends on the band alignment of active layer and the built-in potential. It is an estimation of the maximum voltage achieved in a solar cell (Figure 1.5).

Power conversion efficiency (PCE, η)

The PCE of a solar cell is defined as the ratio of maximum power extracted from solar cell to the power of incident light (P_{in}) and can be expressed as equation 1.1:

$$PCE\ (\eta) = \frac{P_{max}}{P_{in}} = (J_{SC} * V_{OC} * \mathrm{FF})/P_{in} \qquad (1.1)$$

The value of maximum power (P_{max}) can be obtained from the product of current and voltage at its maxima (J_{mpp} x V_{mpp}) as depicted in Figure 1.5. The *J-V* profile of PVSCs often depends on the scan direction as it exhibits hysteresis behavior. Therefore, the scan direction (forward or reverse) and the optimum scan rate is also important to obtain consistent photovoltaic parameters.

Fill factor (FF)

Fill factor is a device parameter which is used to assess the deviation of real solar cell efficiency from the maximum power output expected theoretically. High value of FF indicates good quality of solar cells. The FF of a photovoltaic device can be calculated using equation 1.2.

$$FF = \frac{J_{mpp}V_{mpp}}{J_{SC}V_{OC}} \qquad (1.2)$$

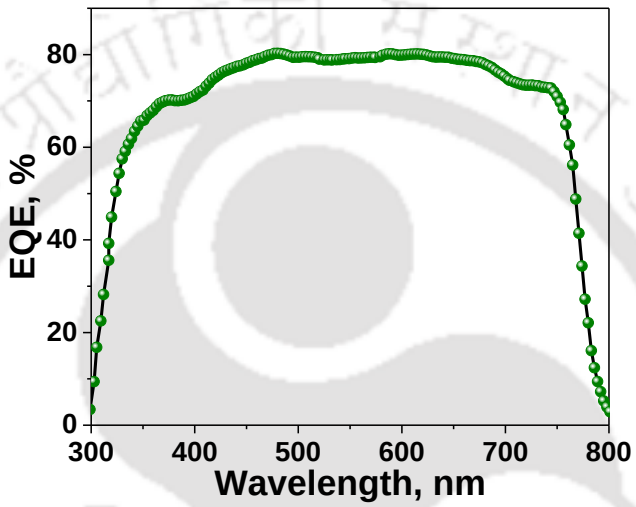

Figure 1.6: A standard EQE graph of a photovoltaic device.

1.5.2 External Quantum Efficiency (EQE)

EQE is the ratio of the number of charge carriers collected by the solar cell to the number of incident photons energy on the solar cell (Figure 1.6). It is a key parameter to estimate the conversion of incident photon into electricity. Integrated J_{SC} from EQE plot can be correlated with *J-V* profile of photovoltaic devices.

1.5.3 Impedance Spectroscopy Measurements

Impedance spectroscopy is a very useful study to elucidate charge carrier transport and kinetics of different process involved in a photovoltaic device.[24,25] The impedance spectroscopic measurement of PSCs and PVSCs is conducted in dark condition, generally in the frequency range of 1 Hz – 1 MHz with sinusoidal voltage amplitude of 10 mV. The impedance data can be presented in the form of either Nyquist plot or Bode plot. By fitting the impedance spectrum, different parameters like shunt resistance, sheet resistance, capacitance, and density of trap states can be evaluated.

1.5 Active Layer Engineering in Polymer and Perovskite Solar cell

Most crucial component of a photovoltaic device is the active layer which absorbs photon in UV-visible range and produce charge carriers. It was always a difficult task to develop suitable material for efficacious charge transport in PSCs and PVSCs. Researchers have utilized different building blocks to synthesize efficient donor and acceptor materials to enhance the efficiency of PSCs.[13] To improve the transport property of PVSCs, suppression of defects and trap states are very crucial. To mitigate the varied kinds of defect at the surface and grain boundaries of perovskite film, numerous methods were explored in PVSCs like compositional tuning, device engineering, molecular passivation, etc.[26-30]

1.5.1 Active Material Engineering for PSCs

The photoactive materials for efficient PSCs should possess some unique photo-physical virtues like 1) wider absorption, 2) well balanced mobility of charge carrier, 3) well matched energy levels of active materials, and 4) ideal aggregating nature of donor and acceptors to develop interpenetrating nano-morphology with proper phase separation in active layer. In 1995, first time $PC_{61}BM$ and conjugated donor polymer based bulk heterojunction PSCs was reported by Heeger and Co-workers.[12] Consequently, a huge transformation has happened in design and development of new materials in last two decades.

1.6.1.1 Development of Donor Copolymers

To achieve higher efficiency and device stability of PSCs, researchers have incorporated new building blocks with fused rings to improve the photon harvesting at higher wavelength region. Planar molecules with extended conjugation usually facilitate the smooth film formation through π-π stacking which improves the transport properties of the blend film. In early years of BHJ PSCs research, homo polymer like P3HT was utilized with fullerene derivatives as a blend of photoactive layer. However, in the last decade donor-acceptor (D-A) copolymers have emerged as suitable photoactive layer materials for PSCs. Due to the intramolecular charge transfer (ICT) in polymer backbone, D-A copolymers have certain advantages like broader absorption, lower band gap (LBG), suitable band alignment and higher charge carrier mobility.

The emergence of Benzodithiophene (BDT) derivatives have rapidly transformed the PSC research in the last decades (Figure 1.7).[31] BDT based copolymers have gained incredible attention because of the bigger π-conjugated planar structure of BDT moiety and the ability to

form ordered molecular packing in thin films.[32] Among numerous BDT containing polymers, one of the efficient donors to exhibit first promising PSC performance was PTB1. In 2009, it was developed by coupling alkoxy substituted BDT based core and thieno[3,4-b]-thiophene (TT) based monomers. As a building block, initially BDT and TT earned huge attention due to its ability of planar quinoid structure formation. PTB1 was blended with $PC_{61}BM$ and $PC_{71}BM$ to fabricate PSCs and the PCE reached > 5% for PTB1:$PC_{71}BM$ blend.[33] A fluorine atom was introduced on TT core of PTB1 to synthesize the PTB7 polymer.[34] Next, the alkoxy side chain on the BDT unit in PTB7 was substituted by a conjugated side chain of alkylated thiophene to develop PTB7-Th.[35] Because of the extended conjugation, PTB7-Th exhibited better absorption and charge transport property which assisted the PCE to reach 8-9% with $PC_{71}BM$. Further, PBDB-T was developed in 2012 by polycondensation of 1,3-di(thiophen-2-yl)-4H,8H-benzo[1,2-c:4,5-c′]dithiophene-4,8-dione (BDD) with BDT-Th based monomer. This highest PCE of 6.67% was recorded with PBDB-T:$PC_{61}BM$ blend.[36] Consequently, PBDB-TS was developed by further side chain engineering of PBDB-T.[37] Further, a linear alkylthio chain was introduced on thiophene conjugated side-chain of BDT core and the resulting polymer, PBDB-TS has the lower HOMO energy level than PBDB-T. This can be attributed to the presence of Sulphur atom on side alkyl chain which can impact distinctively due to the accepting ability of d electron. The relatively deeper HOMO energy level had significantly improved the V_{OC} of the PBDB-TS:ITIC based devices in comparison to PBDB-T:ITIC based PSCs. However, the inferior FF of 0.647 (FF of PBDB-T:ITIC based PSCs = 0.742) did not allow the PCE to cross 10% barrier for these devices. A fluorine atom was introduced on thiophene attached to BDT core along with an alkylthio chain to develop a new copolymer, PBDB-T-SF in 2017.[38] Due to its high electronegativity and ability to influence the inter/intra molecular interaction, fluorine atom can play a significant role in modulating the energy band alignments and in controlling blend morphology. Presence of fluorine atom simultaneously lowered the LUMO and HOMO level of PBDB-T-SF compared to PBDB-T without any significant change in energy band gap. PBDB-T-SF:IT-4F based blend achieved the PCE of 13.1%. For better understanding the impact of fluorine atom on opto-electronic property of D-A copolymers, PM6 copolymer was also developed by the introduction of a fluorine atom on thiophene conjugated side chain of BDT unit in PBDB-T.[39]

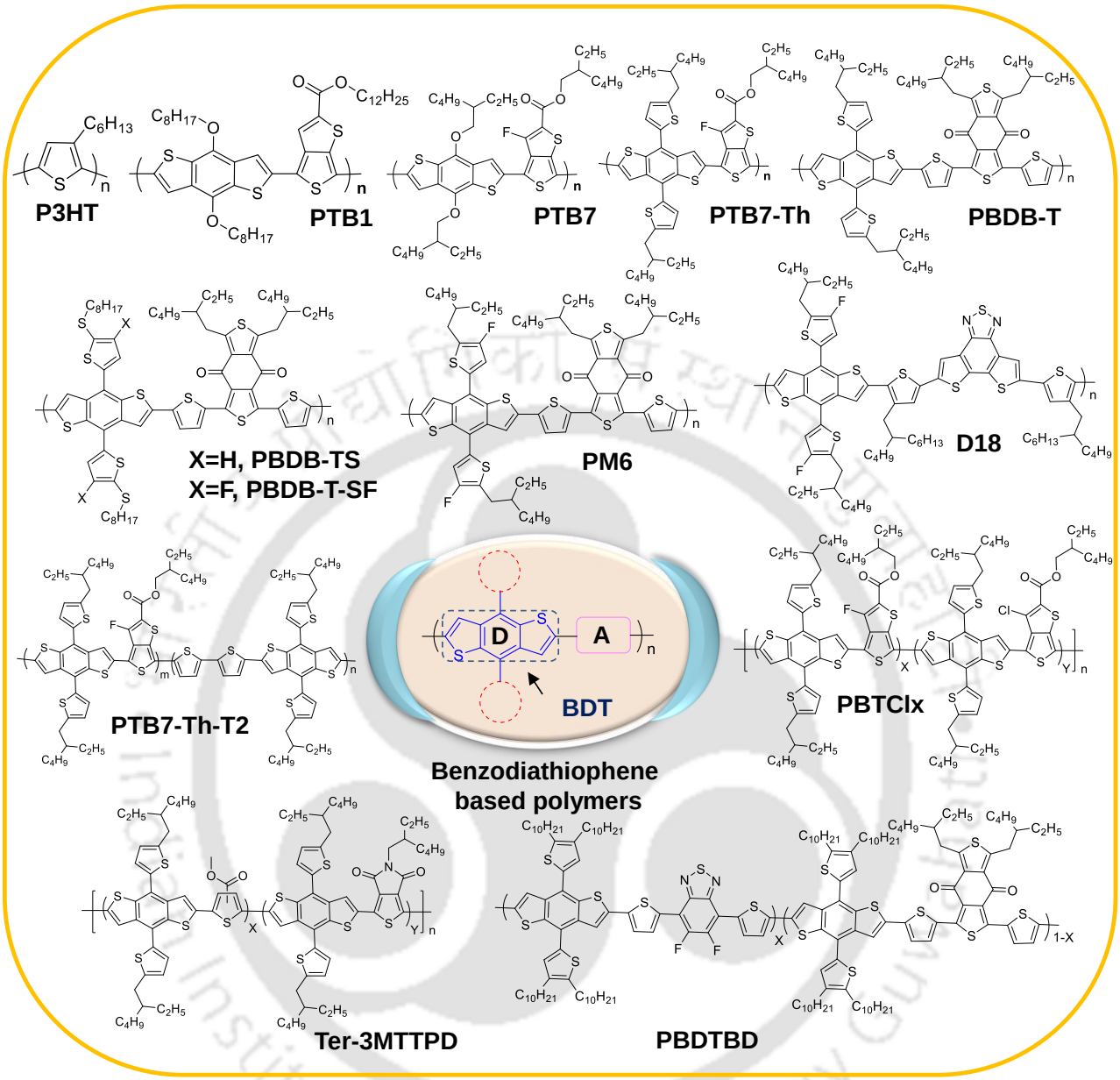

Figure 1.7: Chemical structure of Benzodiathiophene based Polymers.

Due to the presence of fluorine atom; PM6 has deeper HOMO level and stronger π-π interaction in thin film. When PM6:$PC_{71}BM$ blend film was processed in *o*-DCB without any additive, a very smooth film was formed with relatively poor phase separation. To fully utilize the potential of PM6 copolymer, IT-4F (acceptor) was incorporated to blend with PM6 and the PCE reached > 13.5%.[40] In recent times, new donor polymers L1, D16 and D18 were also synthesized by utilizing new building blocks. All these donor polymers are synthesized by incorporating new acceptor (A) monomers like tricyclic fused lactone core based DTP and DTTP utilized for L1

and D16 copolymer respectively.[41,42] Similarly, Benzothiadiazole (BT) based fused molecule was also used to synthesize DTBT, an acceptor monomer which was polymerized with BDT based donor monomer to synthesize D18 polymer.[10] These three polymer blends (L1:Y6, D16:Y6 and D18:Y6) displayed nano-fiber based very uniform film which assisted smooth charge transport and achieved higher PCE of 16-18%.

1.6.1.2 Donor Terpolymers

Although D-A copolymers are among successful class of materials, it is always a difficult task to finely tune its morphology and opto-electronic property. To avoid rigorous synthetic route to develop new polymer donor materials, often third molecule (donor or acceptor) is also incorporated to polymer backbone to synthesize new polymers which are classified as terpolymers.[43] The property of resultant polymers will be directly dependent on nature and quantity of third monomers. Bithiophene (BTh) was utilized as third monomer to substitute 25% of TT unit in popular PTB7-Th backbone to develop PTB7-Th-T2.[44] The introduction of BTh significantly modulated the optoelectronic properties of resultant terpolymer and improved the device performance (PCE = 8.19%). In AFM images, blend film (PTB7-Th-T2:$PC_{71}BM$) with DIO exhibited smooth and intermixed morphology which enhanced their transport property. In 2017, chlorinated TT unit was also introduced in PTB7-Th backbone in varied amount by replacing fluorinated TT to further regulate photophysical properties of PTB7-Th.[45] PBTCl25 (containing 25% Chlorinated TT) had improved device performance (PCE = 8.31%) than other polymers. AFM and TEM analysis indicated that gradual increment of chlorinated TT lowered the surface roughness but larger aggregates were formed in comparison to PTB7-Th films. PBTCl25 had well-balanced optoelectronic property and suitable morphology, hence; it had superior device performance than other blends. To further utilize the ter-polymerization as a technique to improve the photovoltaic performance and durability, Ter-3MTTPD was synthesized using this technique. 4,8-bis(5-(2-ethylhexyl)thiophen-2-yl)benzo[1,2-b:4,5-b′]dithiophene was utilized as a donor monomer and methyl thiophene-3-carboxylate (3MT) along with 5-(2-ethylhexyl)-4H-thieno[3,4-c]pyrrole-4,6(5H)-dione (TPD) as acceptor monomers (in ratio of 1:1) to synthesize the terpolymer. Ter-3MTTPD:NDI-Se blend achieved higher PCE of 7.66% with longer ambient stability compared to the copolymers (with one acceptor). The shelf-life of terpolymer was boosted by the stable morphology of the blend film.[46]

Multiple terpolymers containing 4,8-di(2,3-didecylthiophen-5-yl)-benzo[1,2-b:4,5-b′]dithiophene (BDT), benzo[1,2-c:4,5-c′]dithiophene-4,8-dione (BDD) and 4,7-di(thien-2-yl)-5,6-difluoro-2,1,3-benzothiadiazole (DTffBT) monomers were also developed for high-performance PSCs. When PBDTBD-50 (containing DTffBT:BDD =1:1) was blended with IT-4F, the PCE reached up to 10.03%.[47] In chapter 2 and 3, we have incorporated fluoroarenes as third monomer in the polymer backbone of PTB7-Th to improve photovoltaic performance and long term durability of PSCs.

1.5.2 Materials for Perovskite Solar Cells

Perovskites are a class of materials with a general chemical formula of ABX_3, where A and B are present as cations (size of A >B) and X is an anion. Perovskite has cubic geometry with a backbone of corner-sharing octahedral shaped by X atoms with B atom at the center and cuboctahedra voids occupied by the A-cations (Figure 1.8).

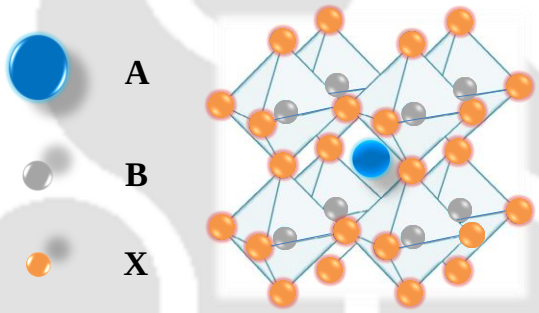

Figure 1.8: Schematic illustration of perovskite crystal unit cell.

Generally, it produces 3D networks of cells. There is a varied class of perovskite compounds out of which the $CH_3NH_3PbI_3$ (or $MAPbI_3$) has been most comprehensively explored. The photophysical property of these materials can be finely tuned by compositional tuning of constituting ions. Ease of fabrication, broader solar absorption, superior charge carrier mobility, longer diffusion length and lower non-radiative recombination rate have made perovskite as ideal material for optoelectronic applications.[48] However, the perovskite materials have several disadvantages like toxicity and instability under ambient condition. Due to this the perovskite thin film can undergo irreversible deterioration. Ultraviolet light and thermal stress can also instigate the degradation of perovskite materials along with heat, light, and moisture.[49] The quality of perovskite films, morphology, crystallinity, and defect density collectively influence the PVSC performance. Significant enhancement in the photovoltaic performance of PVSCs has been achieved through development of new methods for perovskite preparation.[17,50-52] The

molecular passivation is one of the most extensively explored method. Numerous additives are utilized to passivate the perovskite layer and efficiently tune the grain distribution, morphology, stabilizing the perovskite phase, adjust energy band alignment, mitigating non-radiative recombination, reducing hysteresis, and improving device stability. Passivating additives utilized in recent time to enhance the performance and stability of PVSCs is listed as Table 1.1.

The imbalance in stoichiometric composition during perovskite crystal formation and non-coordinated ions (I^-, MA^+, Pb^{2+} etc.) could create defects on the perovskite surface and the grain boundaries.[53] The defects containing areas of the perovskite are more vulnerable to deteriorate under ambient condition. The thermal instability of PVSCs can also be correlated to the expansion of crystal lattice at higher temperature, which instigates the penetration of moisture and oxygen into the perovskite layer.[54] These defect states can also cause non-radiative recombination in the devices which can reduce the photovoltaic performance significantly. Among various explored methods to diminish the defects of perovskite, the surface passivation of perovskite is the most impactful which can also tune the morphology, grain arrangements, roughness, grain size, etc.[30] The nature of perovskite can be tuned by halide engineering which can also reduce the ion migration in photoactive layer. To comprehend the impact of chlorine doping in perovskite, MACl and $PbCl_2$ were also utilized which led to formation of $MAPbCl_3$ perovskite.[55] Due to the volatile nature of chlorine, iodine dominated perovskite film was obtained by annealing.[56-58] In recent time, grain size were increased up to 1500 nm from 250 nm by utilizing the MACl additive with $FAPbI_3$ perovskite film via anti-solvent method and the PCE reached beyond 23%.[59] Lewis bases as passivating agents in PVSCs can considerably mitigate the impact of uncoordinated Pb^{2+} through Lewis base–Lewis acid adduct formation with Lead. DMSO as Lewis base can interact with MAI and PbI_2 to control the crystallization process of perovskite. DMSO can also regulate the morphology perovskite photoactive layer and enhance the device performance. A mixed solvent of γ-butyrolactone (GBL) and DMSO is one of efficient to coat high quality and uniform perovskite film. The efficiency was reached beyond 16% by using this method.[60] The formation of CH_3NH_3I–PbI_2–DMSO adduct in intermediate stage played a key role in controlling the morphology. Furthermore, alkyl amines with varied chain length were also utilized as Lewis bases for passivation of triple-cation perovskite, $Cs_{0.05}FA_{0.70}MA_{0.25}PbI_3$ in 2020and PCE of 21.5% was achieved for octylamine passivated PVSCs.[61]

Table 1.1: A representative list of passivation additives utilized to enhance the performance and stability of PVSCs.

Additive	Device configuration	The role of additive		Perovskite material	PCE, %	Year/ Ref.
		Film formation	Stability (test conditions/ retained PCE)			
Methylammonium Chloride (MACl)	ITO/Y-TiO_2/Perovskite/spiro-OMeTAD/Au	Morphology and phase purity modulator	Devices stored in dry air without encapsulation/~98% after 216 h	$MAPbI_3$	17.91	2015/ 57
Lead chloride	ITO/PEDOT:PSS/perovskite/$PC_{61}BM$/PFN/Ag	Morphology modulator	Stored in a glovebox without encapsulation/75% after 3 months	$MAPbI_3$	14.91	2015/ 58
DMSO	FTO/bl-TiO_2/mp-TiO_2/Perovskite/spiro-MeOTAD/Ag	Solvent and morphology modulator	-	$MAPbI_3$	19.7	2015/ 60
Aliphatic Amines	ITO/PTAA/Perovskite/C_{60}/BCP/Ag	Surface morphology modulator	-	$Cs_{0.05}FA_{0.70}MA_{0.25}PbI_3$	21.5	2020/ 61
Poly(methyl methacrylate) (PMMA)	FTO/c-In-TiO_x/m-TiO_2/PMMA:PCBM/perovskite/PMMA/Spiro-OMeTAD/Au	-	-	$Cs_{0.07}Rb_{0.03}FA_{0.765}MA_{0.135}PbI_{2.55}Br_{0.45}$	20.8	2018/ 62
Thiophene	FTO/c-TiO_2/perovskite/ spiro-OMeTAD/gold	-	-	$MAPbI_{3-x}Cl_x$	15.3	2014/ 63
Pyridine	FTO/c-TiO_2/perovskite/spiro-OMeTAD/gold	-	-	$MAPbI_{3-x}Cl_x$	16.5	2014/ 63
Pyrazine	ITO/SnO_2/Perovskite-Pyrazine/ Spiro-OMeTAD/Au	Surface morphology modulator	Device maintained over 90% of the initial PCE even after aging for 50 h at 55 °C.	FAMAPbClBrI	20.58	2020/ 64
Trimethylolpropane triacrylate (TMTA)	ITO/P_3CT-N/perovskite/PCBM/C_{60}/BCP/Cu	-	Storing the devices at 85 °C in glovebox/~80% after 11h	$MAPbI_3$	19.20	2018/ 65
Fluorinated alkyl chain attached Perylenediimide (FPDI)	FTO/NiOx/Perovskite+FPDI/PCBM/BCP/Ag	Hydrophobicity enhancement and morphology Controller	Retained PCE > 80% of its initial efficiency after ambient exposure for 30 days. Retention of 70% of PCE after heating (100 °C) for 24 h at 50% RH condition.	$MAPbI_3$ and $Cs_{0.05}(FA_{0.83}MA_{0.17})_{0.95}Pb(Br_{0.17}I_{0.83})_3$	19.26	2019/ 66
Fluorinated Aliphatic Amines	FTO/PEDOT:PSS/ $MAPBI_3$/$PC_{61}BM$/BCP/Ag	Surface morphology modulator	Retained PCE of 85% after 240 h of ambient exposure	$MAPbI_3$	13.8	2019/ 67

Popular non-conjugated polymer, PMMA was incorporated as a ultrathin layer in PVSCs and it was observed that the carbonyl (C=O) attached to PMMA efficaciously passivated both perovskite/ETL and perovskite/HTL via interaction with of Pb^{2+}.[62] The passivation of perovskite layer led to the enhancement of PVSC performance. Lewis bases, such as thiophene, pyridine and pyrazine were also incorporated as additive to mitigate the defects states in photoactive layer.[63,64] The passivation of perovskite layer diminished the non-radiative recombination significantly and enhanced the performance of the PVSCs significantly. The instability of PVSCs under ambient condition is a major obstacle for its commercial viability. The strategy of surface passivation has successfully assisted the growth of PVSCs and enhanced its PCE significantly. However, to further enhance the ambient and thermal stability of perovskite layer, various hydrophobic materials were utilized as passivation additives. The hydrophobic additives restricted the moisture penetration in perovskite layer and improved the ambient stability. Moreover, it can also reduce the ion migration and provide structural rigidity by interacting with Pb-I framework which can further enhance the thermal stability of PVSCs. Trimethylolpropanetriacrylate (TMTA), a hydrophobic additive was incorporated into $MAPbI_3$ perovskite layer that interacted chemically to grain boundaries. Further, TMTA was crosslinked within active layer on thermal treatment and PVSCs showed enhanced thermal, UV and moisture stability.[65] Similarly, fluorinated alkyl chain attached perylenediimide, F-PDI was also incorporated in the perovskite layer to improve the device performance along with the device durability. The conductive F-PDI filled the grain boundaries and defects of perovskite layer were passivated significantly which facilitated the charge transport. The F-PDI-incorporated PVSCs with $MAPbI_3$ and $Cs_{0.05}(FA_{0.83}MA_{0.17})_{0.95}Pb(Br_{0.17}I_{0.83})_3$ achieved PCE of 18.28% and 19.26% and exhibited higher ambient and thermal stability.[66]

1.6 Thesis Synopsis

Intrigued from the emerging issues of depleting conventional energy sources and increasing global warming, the focus of this thesis is to achieve sustainable energy generation by further progress of polymer and perovskite solar cells in terms of efficiency and device durability. The first part of the thesis emphasizes on the design and synthesis of new terpolymers. Further, their structure-property correlation, photovoltaic performance and device stability were analyzed. The second part is focused on the enhancement and comprehension the crystallization method of perovskite material. In addition, the mitigation of trap states and ion migration in perovskite

layer has also been achieved via additive engineering. The results obtained during the course of these developments are divided into four chapters. Lastly, a summary of the thesis and future prospect is also presented. A brief outline of these chapters is given below

Chapter 2 aims to improve the performance of the conjugated polymer, PTB7-Th, and reducing the overall cost. Thus, random terpolymers, M1 and M1´, were synthesized by the Stille poly-condensation reaction. For this, 2,5-difluorobenzene (FBZ) was used in the polymerization reaction to partially substitute 3-fluorothieno[3,4-b]thiophene-2- carboxylate (FTT) during the coupling with thienyl-substituted benzo[1,2-b:4,5-b´]-dithiophene (BDT-Th) to obtain the two terpolymers. The polymers, M1 and M1´, contained 5% and 10% of the FBZ monomer in the polymer backbones, respectively. The presence of FBZ significantly improved the molecular alignment of the polymer in thin film by substantially decreasing the dihedral angle in the polymer backbone. The dihedral angle was reduced via several inter/intramolecular interactions (S-F, O-F or C-F) involving the fluorine atom present at the diagonal positions of FBZ. These non-covalent interactions significantly controlled the charge carrier movement and nano-morphology of the active layer blend film which enhanced the short circuit current density (J_{SC}). The presence of extra fluorine atoms on the terpolymer backbone deepened their HOMO level without a drastic modification in the energy band gap, which helped to achieve a high open circuit voltage (V_{OC}) of 0.880 V for M1´. M1:$PC_{71}BM$ achieved efficiency of 8.78% with V_{OC} = 0.852 V, compared to 7.87% of PTB7-Th with V_{OC} = 0.790 V with device architecture of ITO/PEDOT:PSS/Photoactive layer/Ca/Al. Thus, it has been exhibited that incorporation of fluoroarene like FBZ can improve the photovoltaic performance of PSCs by tuning backbone planarity, energy band alignment and blend morphology.

Chapter 3 focuses on comparative analysis about the impact of various fluoroarene monomers on the performance and stability of terpolymer:$PC_{71}BM$ based polymer solar cells. By substituting 5% of 3-fluorothieno[3,4-b]thiophene-2-carboxylate (FTT) in PTB7-Th backbone using monomers like 2,5-difluorobenzene, 2,3-difluorobenzene and 2,3,5,6-tetrafluorobenzene, random terpolymers M1, M2 and M3 were synthesized, respectively. The presence of fluorinated monomers deepened the highest occupied molecular orbital (HOMO) energy level of terpolymers which substantially enhanced the open circuit voltage (V_{OC}) of polymer solar cells (PSCs). The PCE for M1 and M2 based PSCs reached up to 9.48% and 8.80% from 8.19% for

PTB7-Th:$PC_{71}BM$ blend (Device Architecture: ITO/PEDOT:PSS/Photoactive layer/BCP/Ag). However, M3 based blend achieved an inferior PCE of 8.13% majorly due to its weaker absorption at higher wavelength region and lower carrier mobility. Moreover, the fluoroarenes induced intra/intermolecular non-covalent interactions in blend films. These interactions acted as a conformational lock to tune the morphology that also improved the phase domain stability. M1:$PC_{71}BM$ based PSC displayed superior capability to sustain in ambient condition and it retained 82% of its initial PCE after 1000 h of ambient exposure in comparison to 51% of PTB7-Th blend under relative humidity of 45 ± 5%. This generic approach can be utilized in finely modulating the property of photovoltaic materials to enhance the performance along with the stability of PSCs.

Chapter 4 focuses on the trap passivation of perovskite solar cells to enhance the photovoltaic performance along with its device stability by utilizing multifunctional fluoroaromatic amine based additives i.e., 4-fluoroaniline (FA), 2,4,6-trifluoroaniline (TFA) and 2,3,4,5,6-pentafluoroaniline (PFA). Among these additives, PFA most proficiently improved the efficiency along with the ambient and thermo-stability of $MAPbI_3$ based PVSCs. PFA significantly passivated the defects and assisted better charge transport in the devices. The power conversion efficiency (PCE) was enhanced beyond 20% for the PFA passivated device, compared to the 15.08% of the pristine device without any passivation. Moreover, the PFA passivated device retained up to 87% PCE, compared to 26% for the pristine device when exposed to relative humidity ~50% for 1000 h. The fluorine atoms attached to the passivation additives were able to provide protection to the PVSCs against moisture induced erosion. Furthermore, only 10% efficiency was maintained by the pristine device in comparison to 82% for the PFA based device after 20 h of heating at 100 °C inside a glovebox. Thus, this work presented a generic approach to improve the overall stability and performances of PVSCs using fluorarene derivatives, thereby widening the possibility towards practical applications.

Chapter 5 discusses about the trap passivation of perovskite solar cells utilizing a multifunctional additive, 5-fluoropyrimidine-2,4(1H,3H)-dione (FPD). FPD was incorporated in $MAPbI_3$ based photoactive layer to enhance its photovoltaic efficiency along with its ambient stability. When this biologically active cancer drug was utilized as a passivation additive, significant improvement was achieved in all photovoltaic parameters that collectively

contributed in the enhancement of photovoltaic efficiency. The efficiency of PVSCs was elevated up to 20.22% for FPD passivated devices from 15.10% for pristine device without any passivation. Furthermore, the incorporation of FPD also improved the long-term durability of PVSCs by suppressing defects and enhancing the hydrophobicity of perovskite surface. The FPD passivated device maintained PCE up to 89% in comparison to 27% for pristine devices when PVSCs were exposed to relative humidity 45 ± 5% for 1000 h. This unique approach has elucidated the impact of passivation which significantly enhanced the efficiency and long-term stability to widen the possibility of real life applications.

Chapter 6 illustrates the conclusions of the research work and its future prospects. A brief summary of research work conducted and possibilities of investigations essential towards the practical application of photovoltaic devices in the near future is also presented.

1.8 References

(1) N. Armaroli and V. Balzani, *Angew. Chem., Int. Ed.*, 2007**, 46**, 52-66.

(2) D. Gust,T. A. Moore and A.L. Moore, *Acc. Chem. Res.*, **2009,** *42*, 1890-1898.

(3) M. Grätzel, M. *Nature*, 2001**, 414**, 338-344.

(4) F. Akira and H. B. Kenichi, *Chem. Soc. Jpn.*, 1971**, 44**, 1148-1150.

(5) A. Fujishima and K. Honda, *Nature*, 1972**, 238**, 37-38.

(6) H. Kang, G. Kim, J. Kim, S. Kwon, H. Kim and K. Lee, *Adv. Mater*., 2016, **28**, 7821–7861.

(7) R. Søndergaard, M. Ho¨sel, D. Angmo, T. T. Larsen-Olsen and F. C. Krebs, *Mater. Today*, 2012, **15**, 36–49.

(8) S. Sun, T. Salim, N. Mathews, M. Duchamp, C. Boothroyd, G. Xing, T. C. Sum and Y. M. Lam, *Energy Environ. Sci.*, 2014, **7**, 399–407.

(9) NREL, https://www.nrel.gov/pv/cell-efficiency.html, 2019.

(10) Q. Liu, Y. Jiang, K. Jin, J. Qin, J. Xu, W. Li, J. Xiong, J. Liu, Z. Xiao, K. Sun, S. Yang, X. Zhang and L. Ding, *Sci. Bull.*, 2020, **65**, 272–275.

(11) N. S. Sariciftci, D. Braun, C. Zhang, V. I. Srdanov, A. J. Heeger, G. Stucky and F. Wudl, *Appl. Phys. Lett.*, 1993, **62**, 585–587.

(12) G. Yu, J. Gao, J. C. Hummelen, F. Wudl and A. J. Heeger, *Science*, 1995, ***270***, 1789–1791.

(13) C. Cui and Y. Li, *Energy Environ. Sci.*, 2019, **12**, 3225–3246.

(14) A. Kojima, K. Teshima, Y. Shirai and T. Miyasaka, Novel Photoelectrochemical Cell with Mesoscopic Electrodes Sensitized by Lead-Halide Compounds. In 210th ECS Meeting, Cancun, Mexico, 2006; p 397.

(15) A. Kojima, K. Teshima, Y. Shirai and T. Miyasaka, Novel Photoelectrochemical Cell with Mesoscopic Electrodes Sensitized by Lead-Halide Compounds. In 214th ECS Meeting, Honolulu, Hawaii, 2008.

(16) A. Kojima, K. Teshima, Y. Shirai and T. Miyasaka, *J. Am. Chem. Soc.*, 2009**, 131**, 6050-6051.

(17) H.-S. Kim, C.-R. Lee, J.-H. Im, K.-B. Lee, T. Moehl, A. Marchioro, S.-J. Moon, R. Humphry-Baker, J.-H. Yum, J. E. Moser, M. Grätzel and N.-G. Park, *Sci. Rep*., 2012, **2**, 591.

(18) M. M. Lee, J. Teuscher, T. Miyasaka, T. N. Murakami and H. J. Snaith, *Science*, 2012**, 338**, 643-647.

(19) A. C. Mayer, S. R. Scully, B. E. Hardin, M. W. Rowell and M. D. McGehee, Mater. Today, 2007, **10**, 28–33.

(20) M. Liu, M. B. Johnston and H. J. Snaith, *Nature* 2013**, 501**, 395.

(21) J. -Y. Jeng, Y.-F. Chiang, M. -H. Lee, S. –R. Peng, T.-F. Guo, P. Chen and T.-C. Wen, *Adv. Mater.*, 2013**, 25**, 3727-3732.

(22) M. Urbani, G. de la Torre, M.K. Nazeeruddin and T. Torres, *Chem. Soc. Rev.*, 2019**, 48**, 2738-2766.

(23) Z. H. Bakr, Q. Wali, A. Fakharuddin, L. Schmidt-Mende, T.M. Brown and R. Jose, *Nano Energy*, 2017**, 34**, 271-305.

(24) A. Zaban, A. Meier and B. A. Gregg, *J. Phys. Chem. B*, 1997**, 101**, 7985-7990.

(25) R. Kern, R. Sastrawan, J. Ferber, R. Stangl, and J. Luther, *Electrochim. Acta,* 2002**, 47**, 4213-4225.

26) J. Prakash, A. Singh, G. Sathiyan, R. Ranjan, A. Singh, A. Garg and R. K. Gupta, *Mater. Today Energy*, 2018, **9**, 440–486.

27) S. Emami, J. Martins, D. Ivanou and A. Mendes, *J. Mater. Chem. A*, 2020, **8**, 2654–2662.

(28) H. C. Weerasinghe, Y. Dkhissi, A. D. Scully, R. A. Caruso and Y. B. Cheng, *Nano Energy*, 2015, **18**, 118–125.

(29) R. Ranjan, A. Prakash, A. Singh, A. Singh, A. Garg and R. K. Gupta, *J. Mater. Chem. A*, 2018, **6**, 1037–1047

(30) P. Zhao, B. J. Kim and H. S. Jung, *Mater. Today Energy*, 2018, **7**, 267–286

(31) J. Hou, M.-H. Park, S. Zhang, Y. Yao, L.-M. Chen, J.-H. Li and Y. Yang, *Macromolecules*, 2008, **41**, 6012–6018.

(32) B. Zheng, L. Huo and Y. Li, *NPG Asia Mater.*, 2020, **12**, 3.

(33) Y. Liang, Y. Wu, D. Feng, S.-T. Tsai, H.-J. Son, G. Li and L. Yu, *J. Am. Chem. Soc.*, 2009, **131**, 56–57.

(34) Y. Liang, Z. Xu, J. Xia, S.-T. Tsai, Y. Wu, G. Li, C. Ray and L. Yu, *Adv. Mater.*, 2010, **22**, E135–E138.

(35) S.-H. Liao, H.-J. Jhuo, Y.-S. Cheng and S.-A. Chen, *Adv. Mater.*, 2013, **25**, 4766–4771.

(36) D. Qian, L. Ye, M. Zhang, Y. Liang, L. Li, Y. Huang, X. Guo, S. Zhang, Z. A. Tan and J. Hou, *Macromolecules*, 2012, **45**, 9611–9617.

(37) Y. Wu, Y. Zou, H. Yang, Y. Li, H. Li, C. Cui and Y. Li, *ACS Appl. Mater. Interfaces*, 2017, **9**, 37078–37086.

(38) W. Zhao, S. Li, H. Yao, S. Zhang, Y. Zhang, B. Yang and J. Hou, *J. Am. Chem. Soc.*, 2017, **139**, 7148–7151.

(39) M. Zhang, X. Guo, W. Ma, H. Ade and J. Hou, *Adv. Mater.*, 2015, *27*, 4655–4660.

(40) S. Zhang, Y. Qin, J. Zhu and J. Hou, *Adv. Mater.*, 2018, **30**, 1800868.

(41) J. Xiong , K. Jin , Y. Jiang , J. Qin , T. Wang , J. Liu , Q. Liu , H. Peng , X. Li , A. Sun , X. Meng , L. Zhang , L. Liu , W. Li , Z. Fang , X. Jia , Z. Xiao , Y. Feng , X. Zhang , K. Sun , S. Yang , S. Shi and L. Ding , *Sci. Bull.*, 2019, **64** , 1573 —1576.

(42) J. Liu , L. Liu , C. Zuo , Z. Xiao , Y. Zou , Z. Jin and L. Ding , *Sci. Bull.*, 2019, **64** , 1655-1657

(43) T. E. Kang, K.-H. Kim and B. J. Kim, *J. Mater. Chem. A*, 2014, **2**, 15252-15267.

(44) T. Jiang, J. Yang, Y. Tao, C. Fan, L. Xue, Z. Zhang, H. Li, Y. Li and W. Huang, *Polym. Chem.*, 2016, **7**, 926–932.

(45) S. Qu, H. Wang, D. Mo, P. Chao, Z. Yang, L. Li, L. Tian, W. Chen and F. He, *Macromolecules*, 2017, **50**, 4962-4971

(46) A. Kim , C. G. Park , S. H. Park , H. J. Kim , S. Choi , Y. U. Kim , C. H. Jeong , W.-S. Chae , M. J. Cho and D. H. Choi , *J. Mater. Chem. A*, 2018, **6** , 10095 —10103.

(47) H. Jung, G. Yu, S. Jang, I. Hwang, B. Kim, B. S. Kim, Y. Lee, *Org. Elec.*, 2020, **86**, 105929.

(48) M. A. Green, A. Ho-Baillie and H. J. Snaith, *Nat. Photonics*, 2014**, 8**, 506.

(49) G. Grancini, C. Roldán-Carmona, I. Zimmermann, E. Mosconi, X. Lee, D. Martineau, S. Narbey, F. Oswald, F. De Angelis, M. Graetzel and M. K. Nazeeruddin, *Nat. Commun.*, 2017**, 8**, 15684.

(50) N. J. Jeon, J. H. Noh, Y. C. Kim, W. S. Yang, S. Ryu and S. I. Seok, *Nat. Mater.*, 2014**, 13**, 897.

(51) X. Li, D. Bi, C. Yi, J.-D. Décoppet, J. Luo, S. M. Zakeeruddin, A. Hagfeldt and M. Grätzel, *Science,* 2016**, 353**, 58-62.

(52) E. H. Jung, N. J. Jeon, E. Y. Park, C. S. Moon, T. J . Shin, T.-Y. Yang, J. H. Noh and J. Seo, *Nature,* **2019,** *567,* 511-515.

(53) Z. Wang, C. Dong, X. Wang, M. Li, T. Nan, X. Liang, H. Chen, Y. Wei, H. Zhou, M. Zaeimbashi, S. Cash and N. X. Sun, *npj Flexible Electron*., 2018, **2**, 17.

(54) M. Bag, L. A. Renna, R. Y. Adhikari, S. Karak, F. Liu, P. M. Lahti, T. P. Russell, M. T. Tuominen and D. Venkataraman, *J. Am. Chem. Soc*., 2015, **137**, 13130–13137.

(55) S. T. Williams, F. Zuo, C.-C. Chueh, C. -Y. Liao, P. -W. Liang and A. K. Y. Jen, *ACS Nano,* **2014,** *8*, 10640-10654.

(56) Y. Zhao and K. J. Zhu, *J. Phys. Chem. C,* 2014**, 118**, 9412-9418.

(57) Q. Chen,H. Zhou, Y. Fang, A. Z. Stieg, T. –B. Song, H. –H. Wang, X. Xu, Y. Liu, S. Lu, J. You, P. Sun, J. McKay, M. S. Goorsky, Y. Yang, *Nat. Commun.*, 2015**, 6**, 7269.

(58) M. –F. Xu, H. Zhang, S. Zhang, H. L. Zhu, H. –M. Su, J. Liu, K. S. Wong, L. –S. Liao, W. C. H. Choy, *J. Mater. Chem. A,* 2015**, 3**, 14424-14430.

(59) M. Kim, G. -H. Kim, T. K. Lee, I. W. Choi, H. W. Choi, Y. Jo, Y. J. Yoon, J. W. Kim, J. Lee, D. Huh, H. Lee, S. K. Kwak, J. Y. Kim, D. S. Kim, *Joule,* 2019**, *3*,** 2179-2192.

(60) N. J. Jeon, J. H. Noh, Y. C. Kim, W. S. Yang, S. Ryu and S. I. Seok, *Nat. Mater.*, 2014**, 13**, 897.

(61) W. Feng, C. Zhang, J. X. Zhong, L. Ding and W. Q. Wu, *Chem. Commun*., 2020, **56**, 5006–5009.

(62) J. Peng, J. I. Khan, W. Liu, E. Ugur, T. Duong, Y. Wu, H. Shen, K. Wang, H. Dang, E. Aydin, X. Yang, Y. Wan, K. J. Weber, K. R. Catchpole, F. Laquai,S. De Wolf and T. P. White, *Adv. Energy Mater.*, 2018**, 8**, 1801208.

(63) N . K. Noel, A. Abate, S. D.Stranks, E. S. Parrott, V. M. Burlakov, A. Goriely and H . J. Snaith, *ACS Nano,* 2014**, 8**, 9815-9821.

(64) M.-S. Lee, S. Sarwar, S. Park, U. Asmat, D. T. Thuy, C.-H. Han, S. Ahn, I. Jeong and S. Hong, *Sustainable Energy Fuels*, 2020, **4**, 3318–3325.

(65) X. Li, W. Zhang, Y.-C. Wang, W. Zhang, H.-Q. Wang, J. Fang, *Nat. Commun.* 2018**, *9*,** 3806.

(66) J. Yang, C. Liu, C. Cai, X. Hu, Z. Huang, X. Duan, X. Meng, Z. Yuan, L. Tan and Y. Chen, *Adv. Energy Mater*., 2019, **9**, 1900198.

(67) S. Zhao, B. Zhao, Y. Chen, G. Yang and X. Li, *ACS Appl. Energy Mater.*, 2019, **2**, 6230-6236.

Chapter 2

Tuning the Open Circuit Voltage by Incorporating Difluorophenyl Unit into Polymer Backbone to Achieve High Efficiency Polymer Solar Cells

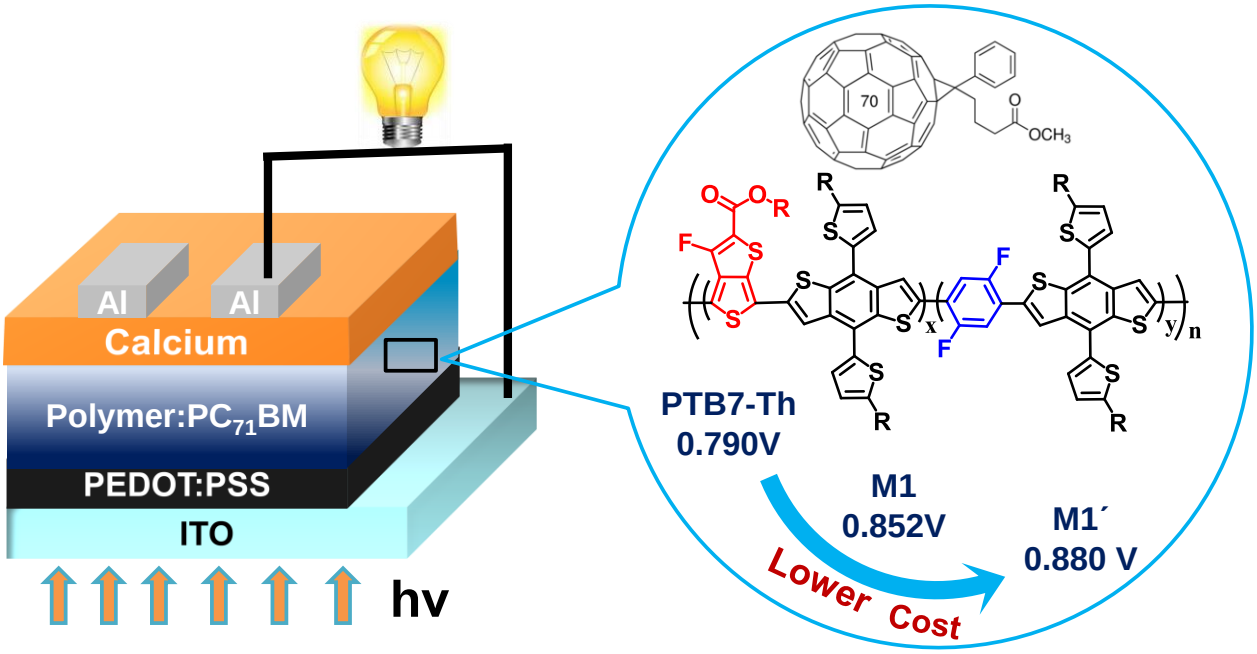

M. Hossain, M. A. Afroz, R. Garai, and P. K. Iyer, *Sustainable Energy Fuels*, 2021, **5**, 874–879.

Abstract

Two new random terpolymers have been synthesized by incorporating the cost-effective 2,5-difluorobenzene (FBZ) molecule in the backbone of donor polymer for application in polymer solar cells (PSCs). Replacing 5 and 10 mole percentage of expensive monomer 3-fluorothieno[3,4-*b*]thiophene-2-carboxylate (FTT) in the well-explored donor polymer PTB7-Th with FBZ, new terpolymers, M1 and M1´, were obtained respectively. These new terpolymers exhibited a deeper HOMO energy level, a comparable LUMO energy level with more planar molecular arrangements and improved morphology. These factors led to a remarkable enhancement in open circuit voltage (V_{OC}) and short circuit current (J_{SC}), which helped to achieve a higher power conversion efficiency (PCE) of 8.78% (V_{OC} = 0.852 V) with M1 as compared to 7.87% for PTB7-Th (V_{OC} = 0.790 V). However, in the case of M1´, V_{OC} reached up to 0.880 V with a lower PCE of 3.46% due to the lower range of solar absorbance and inferior fill factor (FF). The hole and electron mobility of the polymer active layers were also estimated by the space charge limited current (SCLC) method. M1 displayed improved hole and electron mobility (2.68×10^{-4} and 1.9×10^{-4} cm^2 V^{-1} s^{-1}, respectively) compared to PTB7-Th and M1´ based devices since the M1 polymer backbone had a lower dihedral angle and superior blend morphology in thin films. The incorporation of the FBZ monomer into polymer backbone has been demonstrated to be a very effective method to synthesize cost-effective donor polymers to fabricate high performance PSCs with enhanced V_{OC}.

2.1 Introduction

Solar energy, the most preeminent option among all renewable energy sources, can fulfill the increasing need for energy demand in an industrialized society, and it is also capable of substituting the conventional energy sources in coming decades.[1,2] Polymer solar cells (PSCs) have gained immense interest in the last decade due to their numerous advantages such as solution-processing and low cost fabrication of efficient flexible large-area devices using eco-friendly techniques.[3–10] Donor–Acceptor (D–A) copolymers are one of the most efficient classes of solar materials due to their wide absorption, desirable HOMO–LUMO energy levels and adequate charge mobility. To improve the efficiency of PSCs, numerous techniques are being used, *e.g.*, polymer backbone alteration,[11–17] modulation of side chains,[18,19] and introducing new

bridging groups[20–22]. However, the fine-tuning of energy band gap, the position of HOMO and LUMO and molecular arrangement in thin films is difficult in case of this class of materials. The synthesis of new monomers to modify the photophysical properties of these polymers also involves rigorous steps using costly building blocks.[23–25] These limitations of D–A copolymers can be overcome using random copolymerization by incorporating a 3rd monomer (donor/acceptor), which can successfully tune the optoelectronic and photovoltaic properties. These new terpolymers can be utilized to analyze about the impact of tailored structural features, and understand the correlation between the molecular structure of the polymers and device properties.

The benzo[1,2-*b*:4,5-*b′*]-dithiophene (BDT) and thieno[3,4-*b*]thiophene (TT) units as building blocks for D–A copolymers are one of the most effective ones, which have drawn considerable attention in last decade.[26] The combination of BDT and TT provides smooth thin films and a wide absorption to the polymer. Further, the presence of a carboxyl group and a fluorine atom on TT decreases the energy band gap of polymers *via* forming a quinoidal structure. PTB7-Th is one of the most explored polymers of this class in recent times, but its cost is too high as its synthesis involves expensive monomers. The introduction of fluorine containing monomers in the polymer backbone is a useful strategy to enhance photovoltaic performance by utilizing the very small van der Waals radius of 1.35 Å and the high electronegativity of fluorine. There are reports in which non-covalent conformational locking (S···F, O···F or C···F) is being used to synthesize semi-crystalline polymers, where these interactions have improved the intermolecular orderly packing and planarity of the polymer backbone.[27–29]

Thus, in this study, with the objective of improving the performance of PTB7-Th, and reducing the overall cost, random terpolymers, M1 and M1′, were synthesized by the Stille poly-condensation reaction (Scheme 2.1). For this, 2,5-difluorobenzene (FBZ) was used in the polymerization reaction to partially substitute 3-fluorothieno[3,4-*b*]thiophene-2-carboxylate (FTT) during the coupling with thienyl-substituted benzo[1,2-*b*:4,5-*b′*]-dithiophene (BDT-Th) to obtain the two terpolymers. The polymers, M1 and M1′, contained 5% and 10% of the FBZ monomer in the polymer backbones, respectively. The presence of FBZ significantly improved the molecular alignment of the polymer in thin film by decreasing the dihedral angles between the monomers. The dihedral angle was reduced *via* inter/intramolecular interactions (S···F, O···F or C···F) involving the fluorine atom present at the diagonal positions of FBZ. These non-

covalent interactions could significantly control the movement and nano-morphology of the active layer thin film and enhance the short circuit current density (J_{SC}). The presence of extra fluorine atoms on the terpolymer backbone deepened their HOMO level without a drastic modification in the energy band gap, which helped to achieve a high open circuit voltage (V_{OC}) of 0.880 V for M1′.[30]

2.2 Results and discussion

All the polymers were obtained in 75–79% yield as purple/black solid after the appropriate purification steps (Scheme 2.1, details given in the experimental section). The synthesized terpolymer (M1 and M1′) structures were confirmed by ^{1}H NMR spectra. Further, the weight average molecular weight (M_w) of PTB7-Th, M1 and M1′ were found to be 149 kDa, 261 kDa and 122 kDa, respectively by gel-permeation chromatography (GPC) (Figure 2.6).

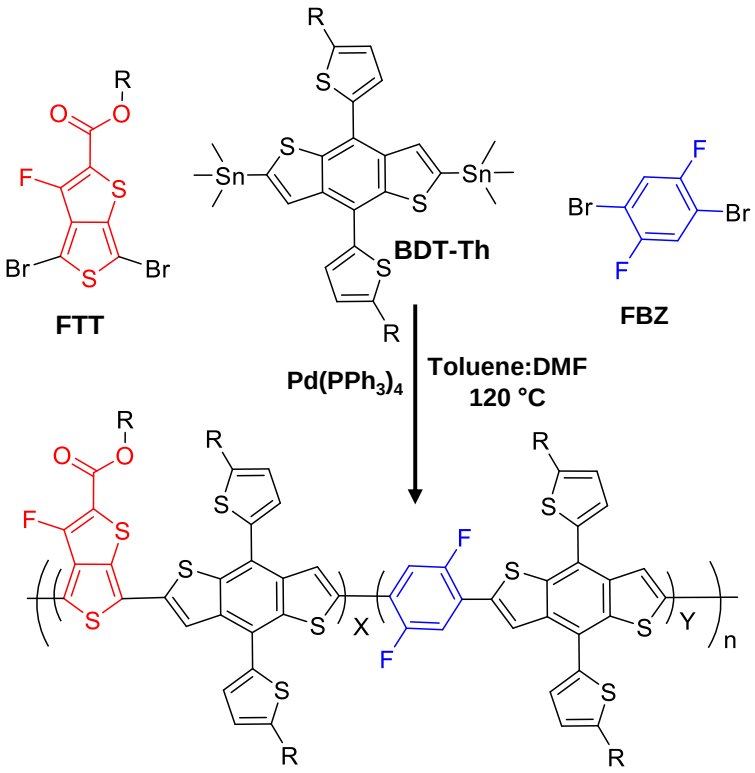

Scheme 2.1: Synthesis of polymers (PTB7-Th, M1, and M1´).

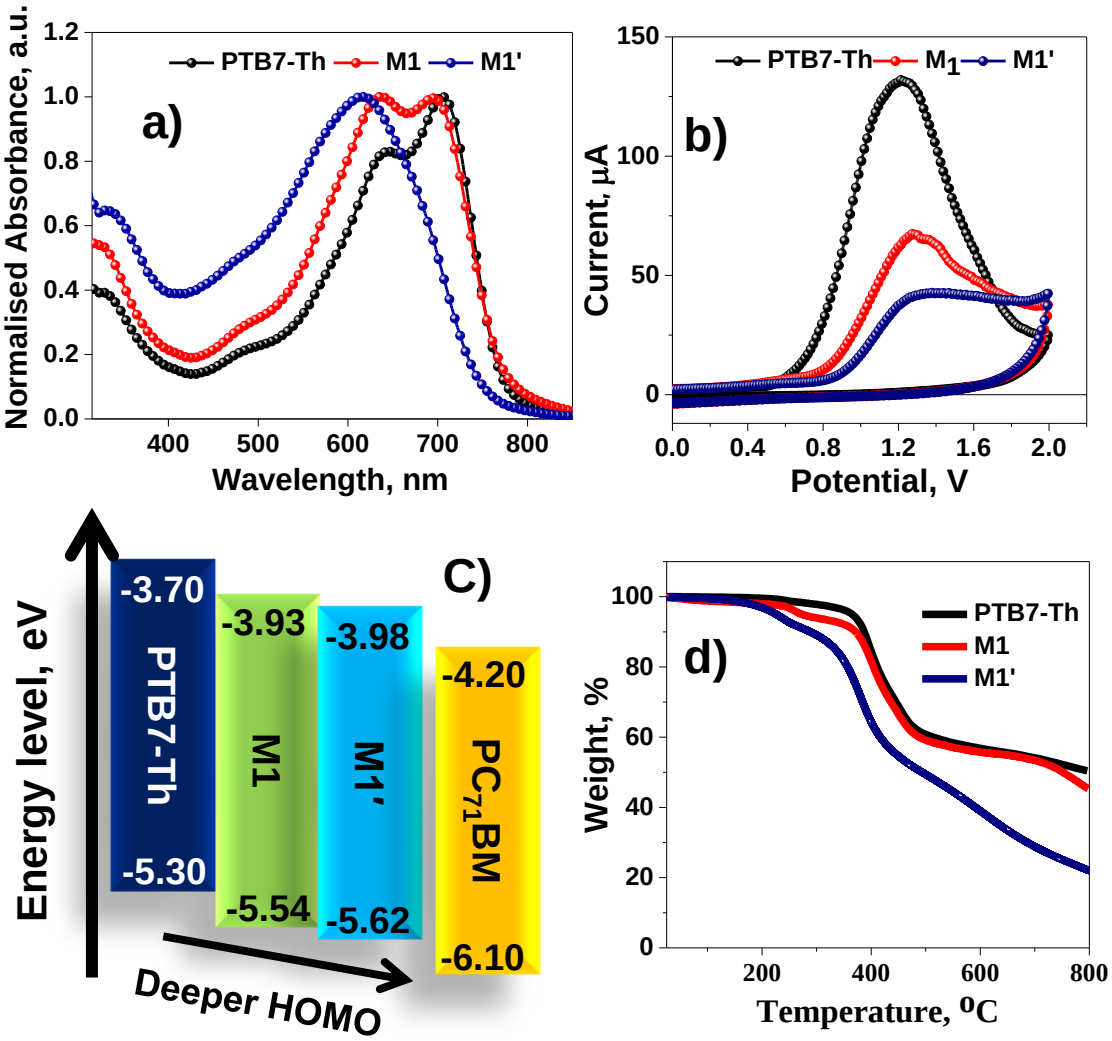

Figure 2.1: a) UV-visible absorption (thin film) curves, b) CV plots of polymer using three-electrode system, c) Energy band diagrams, and d) TGA plots of polymers.

The UV-vis absorption spectra of all polymers (Figure 2.1a) exhibited two absorption bands below 400 nm for localized π–π* transition, and 450–800 nm for the intramolecular charge transfer (ICT) between electron rich BDT-Th and relatively electron deficient FTT in the thin film. Nevertheless, due to the weaker accepting nature of FBZ, there was a blue shift in the UV-visible spectra for M1 and M1′. The absorption of M1 and M1′ in the region of 300–650 nm had a higher intensity as compared to PTB7-Th. The spectral contribution of FBZ to the polymers might be the reason for this trend at the lower wavelength region. The energy band gaps were determined from the onset of the thin film UV-visible spectra of polymers. PTB7-Th and M1 had similar band gaps of 1.60 and 1.61 eV, respectively. However, in case of M1′, the band gap

increased to 1.64 eV. Cyclic voltammetry was employed to further analyze the impact of FBZ incorporation on the energy levels of the terpolymers (using a three-electrode system) (Figure 2.1b). A significant positive shift of the oxidation potential (E_{ox}) for terpolymers was observed with an increment in the percentage of FBZ incorporation. The HOMO energy level of polymers were determined to be 5.30, 5.54, and 5.62 eV for PTB7-Th, M1 and M1′, respectively, using the following equation, $E_{HOMO} = -e(E_{ox} + 4.71)$ (Table 2.1).[31] The presence of the extra fluorine on terpolymers deepened the HOMO energy level, which could effectively enhance the V_{OC} of PSCs. The LUMO energy levels were found to be 3.70, 3.93, and 3.98 eV for PTB7-Th, M1 and M1′, respectively (Figure 2.1c). The thermal stability of the donor polymers was studied by thermogravimetric analysis (TGA) under argon atmosphere with a heating rate of 10 °C /min. 10% weight loss was observed at 298 °C for M1′, which was much lower than 377 °C and 372 °C for PTB7-Th and M1, respectively. The trend of decomposition temperatures (T_d) of these polymers exhibited that the incorporation of FBZ in a higher ratio in the polymer backbone affected its thermal stability adversely (Figure 2.1d) which can be attributed to its intrinsic property of the resultant terpolymers.

Table 2.1: Summary of photophysical and electrochemical properties of polymers

Polymers	**λ_{film}, nm**	**$T_{d,10}$, °C**	**HOMO, eV**	**LUMO, eV**	**E_g, eV**	**μ_h, $cm^2V^{-1}s^{-1}$**	**μ_e, $cm^2V^{-1}s^{-1}$**	**μ_h/μ_e**
PTB7-Th	644, 707	377	-5.30	-3.70	1.60	2.1×10^{-4}	1.7×10^{-4}	1.24
M1	636,696	372	-5.54	-3.93	1.61	2.7×10^{-4}	2.2×10^{-4}	1.23
M1′	616	298	-5.68	-3.98	1.64	1.21×10^{-4}	0.78×10^{-4}	1.55

Density functional theory (DFT) calculations (Figure 2.2a-b) were utilized to study the non-covalent interactions, conformational locking, and dihedral angles. The dihedral angle between FTT and the BDT-Th unit was around 25.5° and 18.8°, which was reduced to 11.5° and 13.4°, respectively, when the FTT unit was replaced by FBZ in the optimized structural models. From the side view, it was clear that BDT-Th-FBZ-BDT was much more planar compared to BDT-Th-FTT-BDT, facilitating well-arranged intermolecular interactions and an improved morphology.

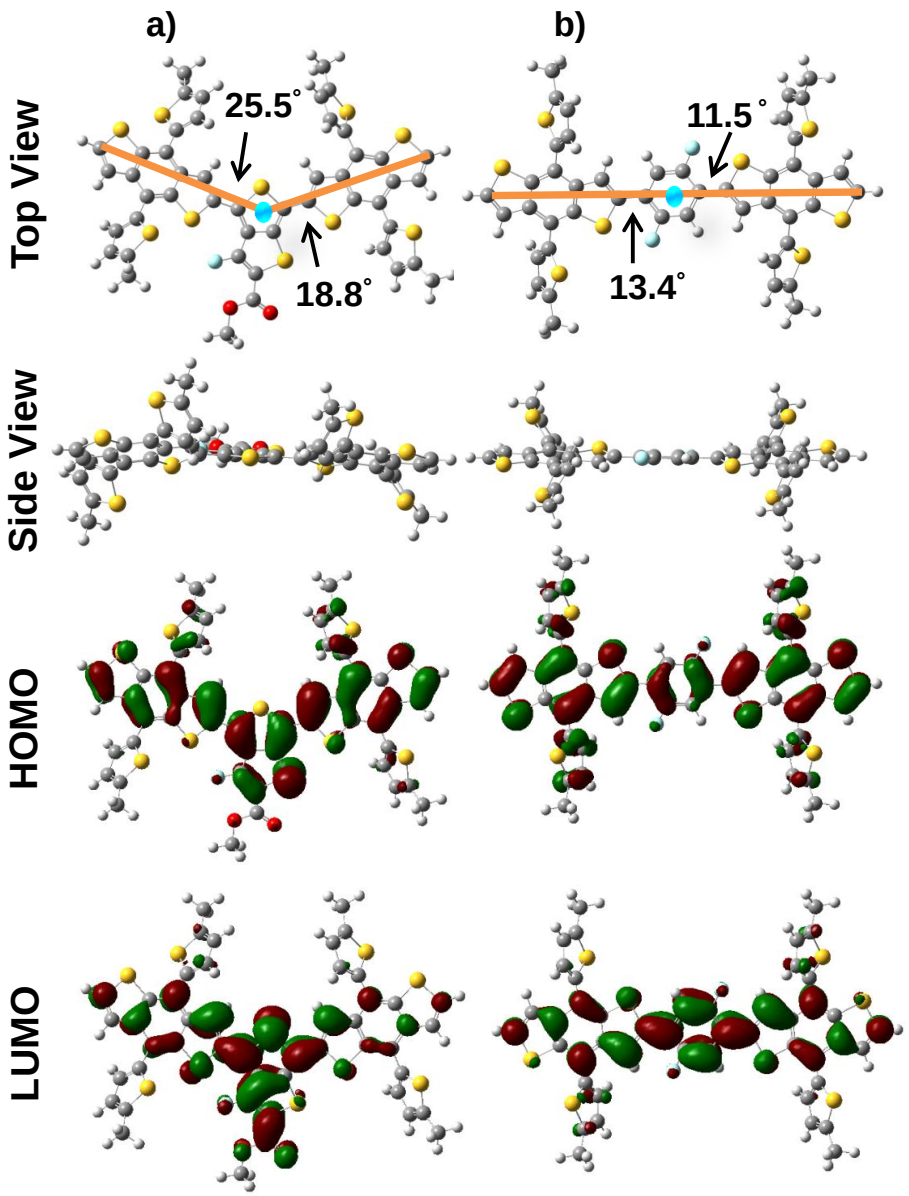

Figure 2.2: Optimized molecular arrangements and HOMO–LUMO energy orbitals based on molecular structure in the polymer backbone for a) BDT-Th-FTT-BDT-Th and b) BDT-Th-FBZ-BDT-Th models in the DFT basis set of B3LYP/6-31G (d,p).

In comparison to the donor polymer PTB7-Th, the modified polymers have deeper HOMO energy levels and lower dihedral angles in the polymer backbone which can facilitate the smoother charge carrier movement in PSCs. To evaluate the overall impact of the FBZ incorporation on the device performances, PSCs were fabricated using the blend of polymers and $PC_{71}BM$ with a conventional photovoltaic architecture (Figure 2.3a). The active layer was

processed in CB with DIO as an additive at room temperature. The *J–V* (current density–voltage) characteristic curves (Figure 2.3b) demonstrated that PTB7-Th, M1, and M1′ had efficiencies of 7.87%, 8.78%, and 3.46%, respectively (Table 2.2).

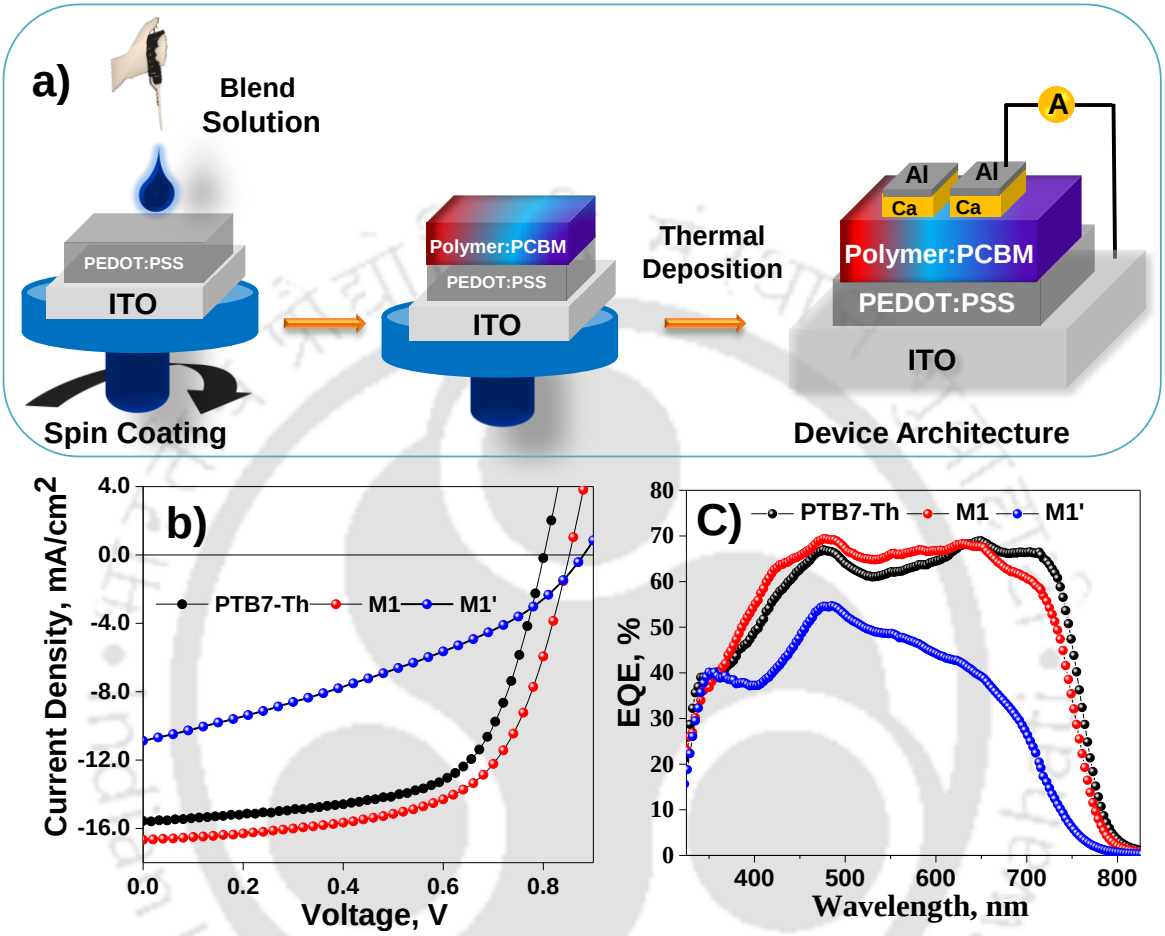

Figure 2.3: a) Schematic illustration of PSCs architecture, b) *J–V* plots, and c) EQE curves of PSCs.

Table 2.2: Summary of photovoltaic Parameters of PSCs

Donor : Acceptor[a]	J_{SC}, mA/cm^2	V_{OC}, V	FF, %	PCE, % (Average)[b]
PTB7-Th:$PC_{71}BM$	15.57	0.790	0.64	7.87 (7.77±0.09)
M1:$PC_{71}BM$	16.62	0.852	0.62	8.78 (8.71±0.05)
M1′:$PC_{71}BM$	10.91	0.880	0.36	3.46 (3.31±0.10)

[a] Polymer:Acceptor = 1:1.5; [b] Average of 15 devices.

M1:$PC_{71}BM$ based PSCs displayed better performances compared to the other two polymer blends because of its improved J_{SC} and V_{OC}. The enhancement in J_{SC} for M1 was attributed to the FBZ induced conformational locking (S···F interaction) which improved backbone planarity. On the other hand, V_{OC} was directly dependent on the differences between the HOMO level of the polymers and the LUMO level of the $PC_{71}BM$.[32] The V_{OC} also gradually enhanced from 0.790 V (PTB7-Th) to 0.880 V (M1′), which was predicted from the lowering trend of HOMO with a higher FBZ incorporation.[33] M1 based PSCs had the highest PCE of 8.78% with a V_{OC} of 0.850 V. Contrarily, the current density was lower for M1′ based blend because it had a lower solubility and an inferior absorption around the near IR region. In Figure 2.3c, external quantum efficiency (EQE) spectra of polymers illustrated similar EQE for PTB7-Th and M1 of around 70%, but M1′ had a lower EQE of 40–50%. The J_{SC} values derived from the integration of EQE graphs of PSCs were comparable and consistent with those observed by *J*–*V* characteristics for all PSC devices.

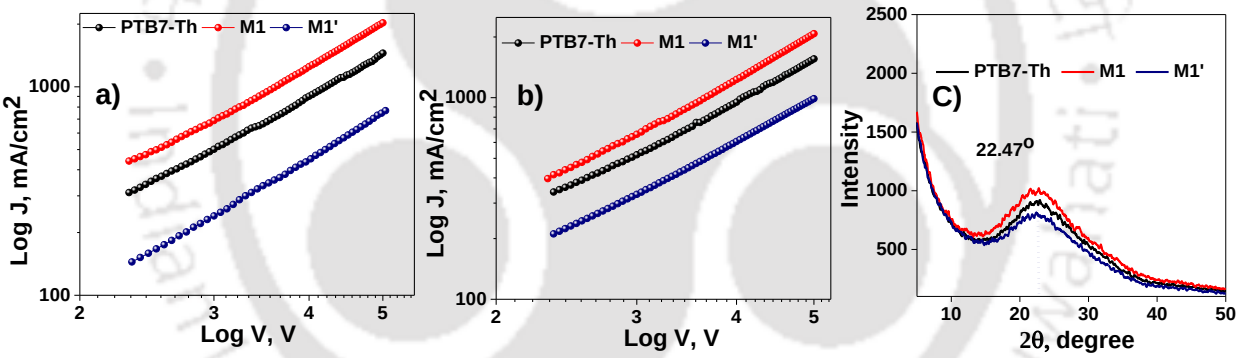

Figure 2.4: SCLC plot for a) hole only device, b) electron only device, and c) XRD patterns of PTB7-Th, M1, and M1′ film.

To further gain better insight about the correlation between the molecular planarity and photovoltaic performance of PSCs, the hole and electron mobility of blends were studied. In order to calculate the hole mobility (μ_h) of the blend films of polymers (PTB7-Th, M1, and M1′) with $PC_{71}BM$, the device architecture ITO/PEDOT:PSS/active layer/Cu was used, and the mobilities were found to be 2.08×10^{-4}, 2.68×10^{-4}, and 1.21×10^{-4} $cm^2\ V^{-1}\ s^{-1}$, respectively, by the space charge limited current (SCLC) method (Figure 2.4a). The hole mobility data indicated an improvement in mobility for M1 compared to PTB7-Th, which significantly contributed in the enhancement of J_{SC} of devices. On the contrary, further increment of the FBZ

content in M1′ hampered the charge carrier mobility within the device, which could be correlated with its comparably higher band gap, less solubility and inferior blend morphology. To analyze the electron mobility (μ_e) of the polymer blend thin films, electron-only devices were fabricated with the architecture of ITO/ZnO/polymers:$PC_{71}BM$/Ca/Al. The electron mobilities were found to be 1.7×10^{-4}, 1.9×10^{-4}, and 7.8×10^{-5} $cm^2\ V^{-1}\ s^{-1}$ for PTB7-Th, M1, and M1′ based devices, respectively (Figure 2.4b). The mobility of electron-only devices followed a similar trend like the hole only devices of polymer:$PC_{71}BM$ blends. M1 based devices had a better electron mobility than the other two polymers. PTB7-Th and M1 based devices showed well-balanced charge carrier mobility and achieved better FF than M1′ based PSC. Thin film X-ray diffractions (XRD) of polymer films were also examined to understand the molecular alignments and the crystalline nature of polymers in the thin-film state. The π–π stacking distance was calculated to be 3.89 Å from the diffraction peaks (22.47°) of the polymers (Figure 2.4c), suggesting that even with the varied FBZ incorporation in the polymer backbone, M1 and M1′ had similar alignment patterns like PTB7-Th in the thin film. Thus, polymer thin films had comparable crystallinity due to this small change in the backbone.

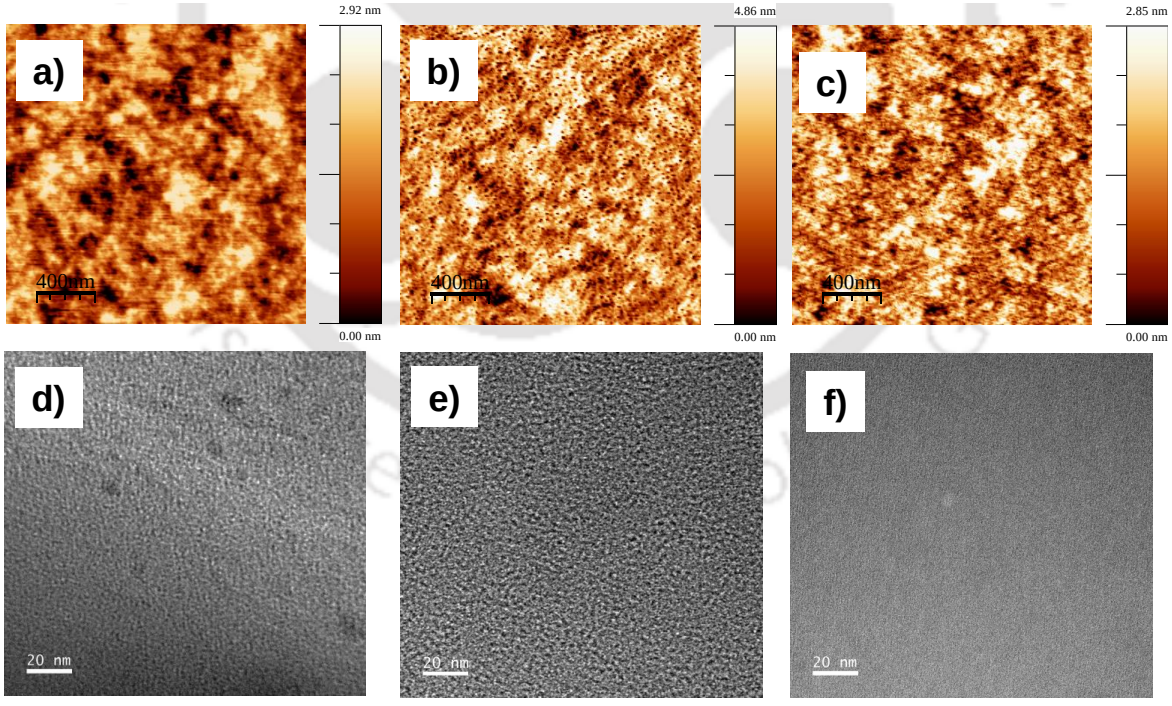

Figure 2.5: AFM height images (2 μm x 2 μm) of a) PTB7-Th:$PC_{71}BM$, b) M1:$PC_{71}BM$, and c) M1′:$PC_{71}BM$ blend films. FETEM images of d) PTB7-Th:$PC_{71}BM$, e) M1:$PC_{71}BM$, and f) M1′:$PC_{71}BM$ blend films.

To gain further insight about the impact of the FBZ monomer on the morphology of blends and its correlation with the device performance, blend thin films were probed by AFM in the tapping mode (Figure 2.5a-c). The roughness (RMS) of the blend films were found to be 1.3 nm, 1.1 nm and 0.8 nm for PTB7-Th:$PC_{71}BM$, M1:$PC_{71}BM$, and M1′:$PC_{71}BM$ thin films, respectively, which exhibited a steady decline in roughness with the increase in the FBZ content in the polymer backbone. The roughness values of thin films were consistent with the device performance of PSCs. Fluorine-induced non-covalent interactions helped in forming smoother thin films for M1 and M1′. However, the introduction of a monomer without a long hydrophobic alkyl chain affected the solubility of polymers, and hence, the film forming property of the blend solution.[34,35] The thin film of the M1′:$PC_{71}BM$ blend had a low roughness (RMS) of 0.8 nm that affected the photovoltaic properties adversely. To obtain further insight into the morphology, the field-emission transmission electron microscopy (FETEM) analysis was performed (Figure 2.5d–f). The PTB7-Th blend with a homogeneous nano-morphology was observed with a little contrast between $PC_{71}BM$ and PTB7-Th. However, M1:$PC_{71}BM$ blend exhibited a less homogeneous nano-structure in thin film, but displayed a better phase separation between the polymer and $PC_{71}BM$. Such a distinct phase separation provided more channels for smoother charge transport in PSCs. M1′:$PC_{71}BM$ blend showed a smooth, but less nano-structured morphology, as the charge transport was not as effective as the other two blends. This decline in the nano-structured morphology may be attributed to higher FBZ-induced aggregation in the active layer thin film. It is evident that the presence of the diflurophenyl based monomer in the polymer backbone played a critical role in tuning the device properties of PSCs. M1 based blend exhibited superior photovoltaic performance than other polymers because of its broad absorption, improved backbone planarity in thin films and deeper HOMO level, which improved the charge carrier mobility, V_{OC} and blend morphology.

2.3 Conclusion

In summary, a simple strategy has been developed to finely tune the opto-electronic properties and film morphology of active polymer layers by incorporating the cost effective 2,5-difluorobenzene (FBZ) into the backbone of the well-known PTB7-Th polymer. Two random terpolymers M1′ and M1′ were synthesized by incorporating 5% and 10% of the FBZ unit in the polymer backbone, with PTB7-Th being synthesized as a reference. The incorporation of the FBZ unit in the polymer backbone resulted in a significant change in the opto-electronic

properties of the polymers, such as the solar absorption, energy level of polymers and morphology of active layer films, which considerably influenced the performance of the PSCs. The incorporation of FBZ majorly improved the V_{OC} from 0.790 to 0.880 V with the increment of the FBZ content in the polymer backbone, which was attributed to the lowering of the HOMO levels of terpolymers. A significant improvement of J_{SC} by 11% (from 15.57 mA/cm^2 for PTB7-Th to 16.62 mA/cm^2 for M1) was also observed which was attributed to the enhancement of the charge carrier mobility of thin films as confirmed from SCLC measurements. The improvement of J_{SC} and V_{OC} collectively contributed in the enhancement of the PCE from 7.87% for PTB7-Th to 8.78% for M1. This understanding on the influential impacts of a fluorinated bridging group will assist to develop highly efficient and cost-effective solar materials for the next generation.

2.4 Experimental Section

2.4.1 Materials

The monomers of 2-Ethylhexyl-4,6-dibromo-3-fluorothieno[3,4-b]thiophene-2-carboxylate (R1) (Price=750 USD/g) and 1,1′-[4,8-Bis[5-(2-ethylhexyl)-2-thienyl]benzo[1,2-b:4,5 b′]dithiophene-2,6-diyl]bis[1,1,1-trimethylstannane] (R2), and $PC_{71}BM$ were purchased from Lumtec. 1,4-dibromo-2,5-difluorobenzene (R3) (Price=7 USD/g) and $Pd(PPh_3)_4$ were bought from Sigma Aldrich. The hole transporting material (HTM) Poly(3,4-ethylenedioxythiophene)-poly(styrenesulfonate) (PEDOT:PSS, PVP AI 4083) was received from Clevios.

2.4.2 Instruments

^{1}H NMR spectra of the polymers were recorded on a Bruker 400 MHz (at 298 K) spectrometers. Absorbance spectra of synthesized polymers film (spin coated from chlorobenzene on a pre cleaned glass slide and vacuum dried) were recorded using a Perkin–Elmer Lambda-35 UV-visible spectrophotometer. Gel-permeation chromatography (GPC) measurements were performed on a Waters 515 chromatograph with tetrahydrofuran as eluent and polystyrene as standard. Thermal stabilities of all polymers under nitrogen atmosphere have been analyzed by thermogravimetric analysis (TGA) in a Netzch (STA 449, Jupiter) instrument at a heating rate of 10 ^{o}C/minute. To determine oxidation potential of polymers three electrode was used and polymer film was coated on a glassy carbon electrode. The thin film of PEDOT:PSS and the active layer blend were deposited on ITO coated glass substrate by spin coating technique using

a Laurell and Spin 150 spin. A JEOL 2100F FETEM was used for FETEM analysis of Blend film. A Veeco Dektak 150 Surface Profilometer was used to measure thicknesses of the thin films. AFM images of the thin active layer films were recorded by Agilent 5500-STM instrument. All the electrical parameters were characterized by Keithley-2400 digital source meter. Newport, Oriel Sol 3A solar simulator with an Oriel 500 W xenon lamp, connected to AM 1.5 Globe filter, was used as solar cell characterization. Newport Oriel IQE-200 instrument was used for external quantum efficiency (EQE) measurement. The XRD patterns of the perovskite films were studied using a Rigaku Micromax-007HF diffractometer equipped with Cu Kα1 irradiation (λ = 1.54184 Å).

2.4.3 General Synthesis Procedure

To synthesize these polymers we have followed previously reported Stille polycondensation based methods.[36] R1, R2, and R3 were weighed into a dry 50 mL Schlenk tube equipped with a magnetic stirrer. After that $Pd(PPh_3)_4$ was added, the mixture was degassed three times, and then toluene and DMF (4:1) were added. The reaction mixture was stirred for 15 hours under argon at 120 °C. After cooling down to room temperature, the dense black gel was precipitated in to 300 mL of MeOH and then stirred for few minutes. By filtration the resulting polymer was collected and washed with MeOH. Further purification was done via Soxhlet extraction sequentially with MeOH, Acetone, n-Hexane, and $CHCl_3$. Then the $CHCl_3$ part was concentrated. Lastly, it was again precipitated and used for device fabrication and other photophysical studies.

***Synthesis of PTB7-Th*:** The polymer, PTB7-Th was synthesized under the same reaction conditions with ratio of R1 (188.8 mg, 0.4 mmol) and R2 (361.82 mg, 0.4 mmol) and Yield: 240 mg (74%), ^{1}H NMR (400 MHz, $CDCl_3$) δ (ppm): 7.38-8.20 (br, 4 H), 6.40-7.20 (br, 2 H), 4.00-4.50 (br, 2 H), 2.50-3.55 (br, 4 H), 0.45-1.95 (br, 45 H), M_w = 149 kDa, M_n= 50 kDa, Đ = 3.01.

***Synthesis of M1*:** The polymer, M1 was synthesized under the same reaction conditions with ratio of R1 (179.45 mg, 0.38 mmol), R2 (361.82 mg, 0.4 mmol) and R3 (5.43 mg, 0.02 mmol) and Yield: 256 mg (79%), ^{1}H NMR (400 MHz, $CDCl_3$) δ (ppm): 7.38-8.20 (br, 4 H), 6.40-7.20 (br, 2 H), 4.00-4.50 (br, 2 H), 2.50-3.55 (br, 4 H), 0.45-1.95 (br, 45 H), M_w = 261 kDa, M_n = 103 kDa, Đ = 2.52.

***Synthesis of M1'*:** The polymer, M1′ was synthesized under the same conditions with ratio of R1 (170 mg, 0.36 mmol), R2 (361.82 mg, 0.4 mmol) and R3 (10.87 mg, 0.04 mmol) and Yield: 256 mg (79%), ^{1}H NMR (400 MHz, $CDCl_3$) δ (ppm): 7.38-8.20 (br, 4 H), 6.40-7.20 (br, 2 H), 4.00-4.50 (br, 2 H), 2.50-3.55 (br, 4 H), 0.45-1.95 (br, 45 H), M_w = 122 kDa, M_n = 46 kDa, Đ = 2.68.

2.4.4 Device Fabrication

Device architecture of ITO/PEDOT: PSS/Active Layer blend/Ca/Al was utilized to fabricate the PSCs where thin layer of PEDOT: PSS was Spin coated on pre-cleaned ITO coated glass with a PEDOT:PSS aqueous solution at 4000 rpm and dried subsequently at 150 °C for 15 min in air, then the device was moved to a argon glove box. The Donor polymers and PCBM blend was prepared in 1:1.5 ratio with a concentration of 35 mg/ml in chlorobenzene and stirrer for 12 hours and 15 mins before spin coating of active layer DIO was added to the solution. After that the donor polymer and PCBM blend was spin coated on PEDOT:PSS thin layer at rpm of 3000. Next sequentially Ca (~20 nm) and Al (~70 nm) were deposited in through a shadow mask on top of the active layer by thermal deposition under high vacuum (5×10^{-6} Torr). Same devices were used for EQE analysis. Hole mobility of the polymers was determined by fitting the dark current to the model of a single carrier SCLC using the device structure ITO/PEDOT: PSS/Active Layer blend/Cu. To further calculate the electron mobility of the polymers, the architecture of ITO/ZnO/polymers:$PC_{71}BM$/Ca/Al was utilized.[37] The slope value was ~2 for all SCLC plots. All devices had a cell area of 0.06 cm^2.

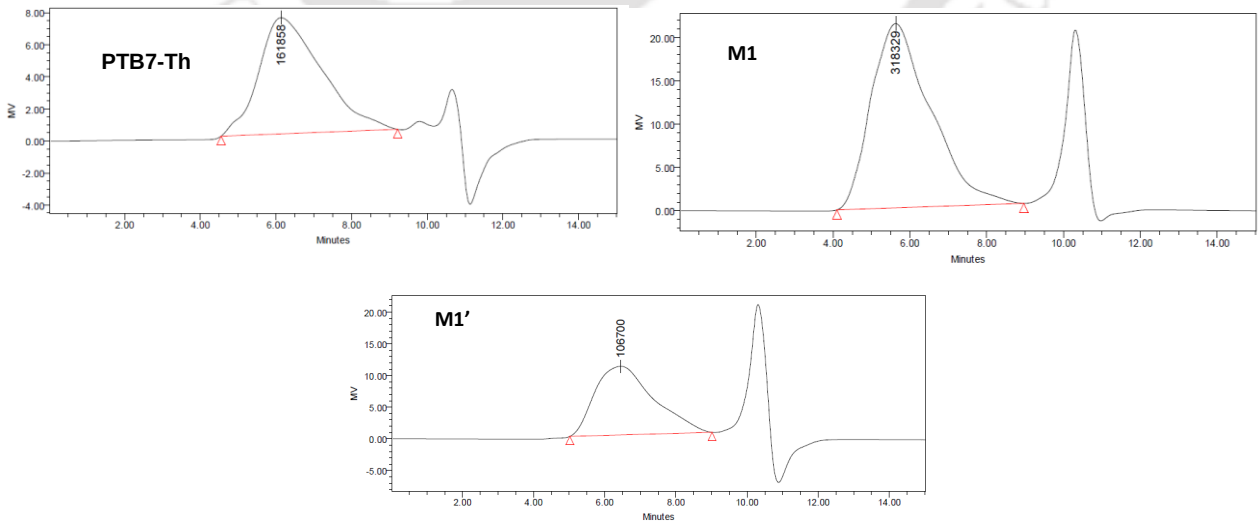

Figure 2.6: GPC of polymers.

2.5 References

(1) N. Armaroli and V. Balzani, *Energy Environ. Sci*., 2011, **4**, 3193-3222.

(2) M. S. Dresselhaus and I. L. Thomas, *Nature 2001*, **414**, 332-337.

(3) G. Yu, J. Gao, J. C. Hummelen, F. Wudl and A. J. Heeger, *Science* 1995, **270**, 1789-1791.

(4) J. J. M. Halls, C. A. Walsh, N. C. Greenham, E. A. Marseglia, R. H. Friend, S. C. Moratti and A. B. Holmes, *Nature* 1995, **376**, 498-500.

(5) C. L. Chochos and S. A. Choulis, Prog. *Polym. Sci.*, 2011, **36**, 1326-1414.

(6) C. J. Brabec, S. Gowrisanker, J. J. M. Halls, D. Laird, S. J. Jia and S. P. Williams, *Adv. Mater.*, 2010, **22**, 3839-3856.

(7) E. E. Havinga, W. Tenhoeve and H. Wynberg, *Synth. Met*., 1993, **55**, 299-306.

(8) G. Li, R. Zhu and Y. Yang, *Nat. Photonics*, 2012, **6**, 153-161.

(9) J. W. Chen and Y. Cao, *Acc. Chem. Res.*, 2009, **42**, 1709-1718.

(10) Z. Zhang, X. J. Zhang, J. C. Zhang, X. Gong, Y. H. Liu, H. Lu, C. H. Li and Z. S. Bo, *RSC Adv*., 2016, **6**, 39074-39079.

(11) H. F. Yao, L. Ye, H. Zhang, S. S. Li, S. Q. Zhang and J. H. Hou, *Chem. Rev.*, 2016, **116**, 7397-7457.

(12) S. Q. Zhang, Y. P. Qin, M. A. Uddin, B. Jang, W. C. Zhao, D. L. Liu, H. Y. Woo and J. H. Hou, *Macromolecules* 2016, **49**, 2993-3000.

(13) H. Zhang, S. Q. Zhang, K. Gao, F. Liu, H. F. Yao, B. Yang, C. He, T. P. Russell and J. H. Hou, *J. Mater. Chem. A*, 2017, **5**, 10416-10423.

(14) Y. H. Cai, X. L. Zhang, X. N. Xue, D. H. Wei, L. J. Huo and Y. M. Sun, *J. Mater. Chem. C*, 2017, **5**, 7777-7783.

(15) Y. H. Li, D. Y. Liu, J. Y. Wang, Z. G. Zhang, Y. F. Li, Y. F. Liu, T. T. Zhu, X. C. Bao, M. L. Sun and R. Q. Yang, *Chem. Mater*., 2017, **29**, 8249-8257.

(16) Y. Z. Lin, F. W. Zhao, Q. He, L. J. Huo, Y. Wu, T. C. Parker, W. Ma, Y. M. Sun, C. R. Wang, D. B. Zhu, A. J. Heeger, S. R. Marder and X. W. Zhan, *J. Am. Chem. Soc*., 2016, **138**, 4955-4961.

(17) H. Huang, L. Yang, A. Facchetti and T. J. Marks, *Chem. Rev*., 2017, **117**, 10291-10318.

(18) J. G. Mei and Z. N. Bao, *Chem. Mater*., 2014, 26, 604-615.

(19) L. J. Huo, X. N. Xue, T. Liu, W. T. Xiong, F. Qi, B. B. Fan, D. J. Xie, F. Liu, C. L. Yang and Y. M. Sun, *Chem. Mater*., 2018, **30**, 3294-3300.

(20) C. Gao, L. W. Wang, X. Y. Li and H. Q. Wang, *Polym. Chem*., 2014, **5**, 5200-5210.

(21) Z. Xu, Q. P. Fan, X. Y. Meng, X. Guo, W. Y. Su, W. Ma, M. J. Zhang and Y. F. Li, *Chem. Mater*., 2017, **29**, 4811-4818.

(22) Y. Kim, D. X. Long, J. Lee, G. Kim, T. J. Shin, K. W. Nam, Y. Y. Noh and C. Yang, *Macromolecules* 2015, **48**, 2948−2957.

(23) S. Q. Zhang, L. Ye and J. H. Hou, *Adv. Energy Mater*., 2016, **6**, 1502529.

(24) H. Benten, D. Mori, H. Ohkita and S. Ito, J. Mater. Chem. A, 2016, 4, 5340-5365.

(25) X. Guo, C. H. Cui, M. J. Zhang, L. J. Huo, Y. Huang, J. H. Hou and Y. F. Li, *Energy Environ. Sci*., 2012, **5**, 7943-7949.

(26) H. F. Yao, L. Ye, H. Zhang, S. S. Li, S. Q. Zhang and J. H. Hou, *Chem. Rev*., 2016, **116**, 7397-7457.

(27) T. L. Nguyen, H. Choi, S. J. Ko, M. A. Uddin, B. Walker, S. Yum, J. E. Jeong, M. H. Yun, T. J. Shin, S. Hwang, J. Y. Kim and H. Y. Woo, *Energy Environ. Sci*., 2014, **7**, 3040-3051.

(28) K. Kawashima, T. Fukuhara, Y. Suda, Y. Suzuki, T. Koganezawa, H. Yoshida, H. Ohkita, I. Osaka and K. Takimiya, *J. Am. Chem. Soc*., 2016, **138**, 10265-10275.

(29) D. Gedefaw, M. Tessarolo, W. Zhuang, R. Kroon, E. Wang, M. Bolognesi, M. Seri, M. Muccini and M. R. Andersson, *Polym. Chem*., 2014, **5**, 2083-2093.

(30) P. Liu, K. Zhang, F. Liu, Y. C. Jin, S. J. Liu, T. P. Russell, H. L. Yip, F. Huang and Y. Cao, *Chem. Mat.*, 2014, **26**, 3009-3017.

(31) Z. Zhang, Y. H. Liu, J. C. Zhang, S. Y. Feng, L. L. Wu, X. Gong, X. J. Xu, X. B. Chen and Z. S. Bo, *ACS Appl. Mater. Interfaces*, 2017, **9**, 23775-23781.

(32) S. W. Qu, H. Wang, D. Z. Mo, P. J. Chao, Z. Yang, L. J. Li, L. L. Tian, W. Chen and F. He, *Macromolecules* 2017, **50**, 4962-4971.

(33) B. Xiao, Y. J. Zhao, A. L. Tang, H. Q. Wang, J. Yang and E. J. Zhou, *Sci. Bull.*, 2017, **62**, 1275-1282.

(34) T. Jiang, J. Yang, Y. T. Tao, C. Fan, L. W. Xue, Z. G. Zhang, H. Li, Y. F. Li and W. Huang, *Polym. Chem.*, 2016, **7**, 926-932.

(35) Z. Tang, J. Wang, A. Melianas, Y. Wu, R. Kroon, W. Li, W. Ma, M. R. Andersson, Z. Ma, W. Cai, W. Tress and O. Inganas, *J. Mater. Chem. A*, 2018, **6**, 12574–12581.

(36) R. Garai, M. A. Afroz, R. K. Gupta, A. Choudhury and P. K. Iyer, *ACS Omega*, 2020, **5**, 2747–2754.

(37) R. K. Gupta, R. Garai, M. A. Afroz and P. K. Iyer, *J. Mater. Chem. C*, 2020, **8**, 8191–8198.

भारतीय प्रौद्योगिकी संस्थान गुवाहाटी
Indian Institute of Technology Guwahati

Chapter 3

Backbone Engineering with Fluoroarene to Mitigate Morphological Disorder for High Performance Polymer Solar Cells

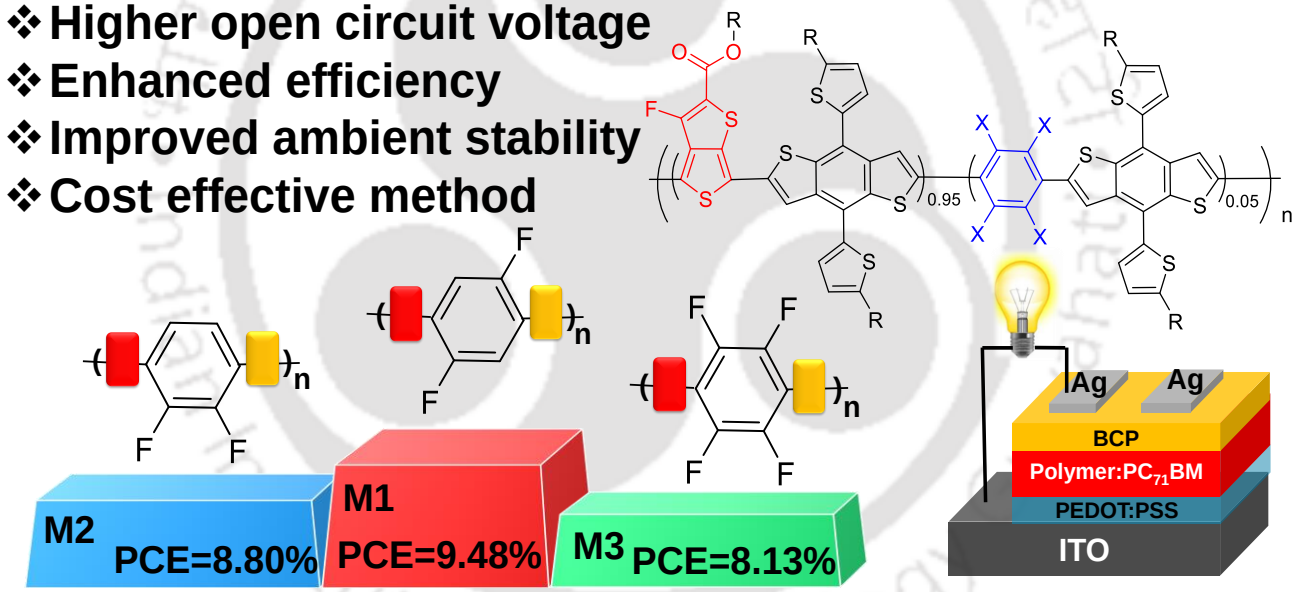

M. Hossain, R. Garai, R. Narasimhan, M. A. Afroz, and P. K. Iyer**,** *ACS Appl. Polym. Mater. 2021, **3**, 5216–5223.*

Abstract

Three random terpolymers were synthesized by subtle incorporation of fluoroarenes as third monomer in popular PTB7-Th backbone and utilized for photovoltaic applications. By substituting 5% of 3-fluorothieno[3,4-b]thiophene-2-carboxylate (FTT) in PTB7-Th backbone using monomers like 2,5-difluorobenzene, 2,3-difluorobenzene, and 2,3,5,6-tetrafluorobenzene, random terpolymers M1, M2, and M3 were synthesized, respectively. The presence of fluorinated monomers deepened the highest occupied molecular orbital (HOMO) energy level of terpolymers which substantially enhanced the open circuit voltage (V_{OC}) of polymer solar cells (PSCs). The power conversion efficiency (PCE) for M1 and M2 based PSCs reached up to 9.48% and 8.80% from 8.19% for PTB7-Th:$PC_{71}BM$ blend. However, M3 based blend achieved an inferior PCE of 8.13% majorly due to its weaker absorption at higher wavelength region and lower carrier mobility. Moreover, the fluoroarenes induced intra/intermolecular non-covalent interactions in blend films. These interactions acted as a conformational lock to tune the morphology that also improved the phase domain stability. M1:$PC_{71}BM$ based PSC displayed superior capability to sustain in ambient condition and retained 82% of its initial PCE after 1000 h of ambient exposure in comparison to 51% of PTB7-Th blend under relative humidity of 45 ± 5%. This generic approach can be utilized in finely modulating the property of photovoltaic materials to enhance the performance along with the stability of PSCs.

3.1 Introduction

Among the renewable energy technologies, polymer solar cells (PSCs) are one of the most preeminent platforms due to their eco-friendly properties and tremendous capability to substitute the existing technology counterpart for next generation.[1,2] The emergence of PSCs was accelerated by the extensive research in the last decade that have explored its distinct advantages like solution processibility, utility as stretchable or flexible device, large area fabrication etc.[3-5] Among numerous p-type photoactive materials, which were incorporated in PSCs, the copolymers have emerged as the most effective photovoltaic materials with n-type semiconductors like fullerene derivatives ($PC_{61}BM$ or $PC_{71}BM$) or recently developed non-fullerene acceptors (NFAs).[6-10] Due to the efficacious intramolecular charge transfer (ICT) between electron rich monomer 'D' and electron deficient monomer 'A' in the polymer backbone, D-A copolymers generally have

extended absorption at near Infra-red (NIR) region along with well-balanced charge mobility and suitable energy band alignment. Furthermore, various strategies like new monomer incorporation, alteration in side-chain, functional group modifications and new fabrication methods were utilized to enhance the efficiency and ambient stability of PSCs.[11-17]

The thiophene substituted benzo[1,2-b:4,5-b']-dithiophene (BDT-Th) based donor and thieno[3,4-b] thiophene (TT) units based acceptor monomers were often utilized to develop efficient D–A copolymers.[11] PTB7-Th is a well-known polymer of this class due to its wide absorption, smooth film formation and high efficiency.[18] However, the fine modulation of molecular aggregation and energy band alignment of these polymers are always a challenging task. Low band gap polymers like PTB7-Th are also susceptible to various kinds of degradations under ambient condition which can adversely impact the performance of the PSCs.[15,19] The phase domains of photoactive layers are very sensitive to external factors like temperature, light, moisture, etc.[20-22] The ambient instability of PSCs can be attributed to the morphological degradation and photo-oxidation of active layer triggered by ambient conditions. These degradations can substantially reduce the photon harvesting capability of PSCs. The photovoltaic efficiency and long term durability are equally crucial for the advancements of PSCs towards industrial applications. The structural modification of polymer backbone can be used as an efficient method to enhance the ambient stability of PSCs along with its PCE.[15] The incorporation of a suitable third monomer in D-A copolymer backbone can be utilized as an effective strategy to finely modulate the morphology of blend film. As a result, the terpolymer based blends are also become capable of maintaining their morphological features and photovoltaic performance even after long ambient exposure. The extent and nature of third monomer in polymer backbone can collectively regulate the opto-electronic properties of terpolymers. Higher concentration of third monomer can impact the ICT in polymer backbone depending upon the electron accepting nature of third monomers compared to the FTT unit. Third monomer incorporation in polymer backbone at very low concentration will also have minimal impact in tuning the energy band alignment, morphology, and overall photovoltaic performance. Hence, an optimal amount of third monomer incorporation is crucial to obtain enhanced device efficiency and stability.

Herein, we have synthesized three terpolymers by incorporating cost effective fluorinated phenyl based monomers (FPMs) like 1,4-dibromo-2,5-difluorobenzene (FPM1), 1,4-dibromo-2,3-difluorobenzene (FPM2), and 1,4-dibromo-2,3,5,6-tetrafluorobenzene (FPM3) in the backbone of PTB7-Th by substituting optimal extent (5%) of 3-fluorothieno[3,4-b]thiophene-2-carboxylate (FTT) unit. The FPM incorporation can induce varied non-covalent interactions (sulphur-fluorine, hydrogen-fluorine or oxygen-fluorine) which can provide conformational locking in polymer backbone and resulting in reduced dihedral angle.[23,24] The non-covalent interactions can substantially facilitate better charge carrier movement to enhance the short circuit current density (J_{SC}) of PSCs. Moreover, the presence of fluorine atoms finely modified the energy band alignment of terpolymers and deepened the HOMO energy levels which assisted terpolymer based PSCs to achieve higher open circuit voltage (V_{OC}). These interactions can also effectively modulate the morphology by improving molecular packing in thin films which can minimize the morphological degradation upon ambient exposure.[15,25] FPM1 incorporated polymer, M1 displayed superior photovoltaic performance over FPM2 and FPM3 incorporated polymer M2 and M3 based blends respectively. M1:$PC_{71}BM$ blend achieved power conversion efficiency (PCE) of 9.48% and maintained 82% of its initial PCE even after 1000 h of ambient exposure.

3.2 Results and Discussion

All the polymers were synthesized by utilizing the Stille polycondensation method with 70-79% yield as black or purple solid through multistep purification method (Scheme 3.1). All the polymers were characterized by ^{1}H NMR. Further, gel-permeation chromatography (GPC) revealed the weight average molecular weight (M_W) of polymers were 149 kDa, 261 kDa, 241 kDa, and 107 kDa for PTB7-Th, M1, M2, and M3, respectively (Figure 2.6 and Figure 3.9). The dispersity (Đ) of polymers were found to be 3.01, 2.52, 2.38, and 2.85 for PTB7-Th, M1, M2, and M3, respectively which are suitable for photovoltaic applications. To further understand the impact of FPM incorporation on UV-vis absorption of polymers, their absorption profiles were recorded (Figure 3.1a). All the polymers displayed two absorption bands in UV-vis absorption spectra which are corresponding to localized π-π* transitions (below 400 nm) and relatively stronger band of 450-800 nm for ICT in polymer backbone.

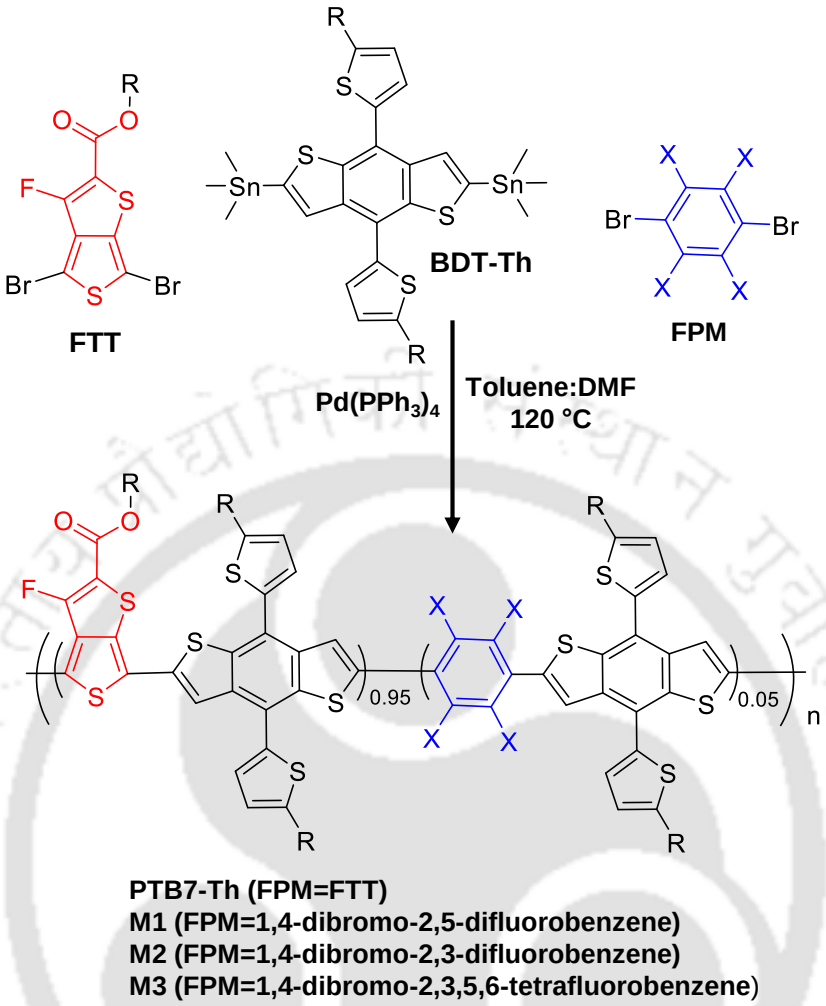

Scheme 3.1: Synthesis of polymers (PTB7-Th, M1, M2, and M3), R=2-ethylhexyl.

Due to the FPM incorporations in terpolymers, the absorption band at lower wavelength region was enhanced significantly. Contrarily, the peak maxima of PTB7-Th in higher wavelength region marginally blue shifted for M1 and M2 terpolymers which can be correlated with the weaker electron accepting nature of the third monomers. The absorption profile of M3 polymer showed blue shifted peak maxima along with a change in peak pattern which can be attributed to the influence of FPM3 on interchain aggregation of the terpolymer.[26] The energy band gaps were found to be very similar from the onset of absorption profile of polymers. The band gaps were calculated to be 1.60 eV for PTB7-Th and 1.61 eV for other terpolymers. To further study about the electrochemical properties, polymers were analyzed using cyclic voltammetry (CV) (using a three-electrode system). For terpolymers, a considerable positive shift was observed in oxidation profile (E_{ox}) which can be attributed to the presence of fluorinated third monomer (Figure 3.1b).

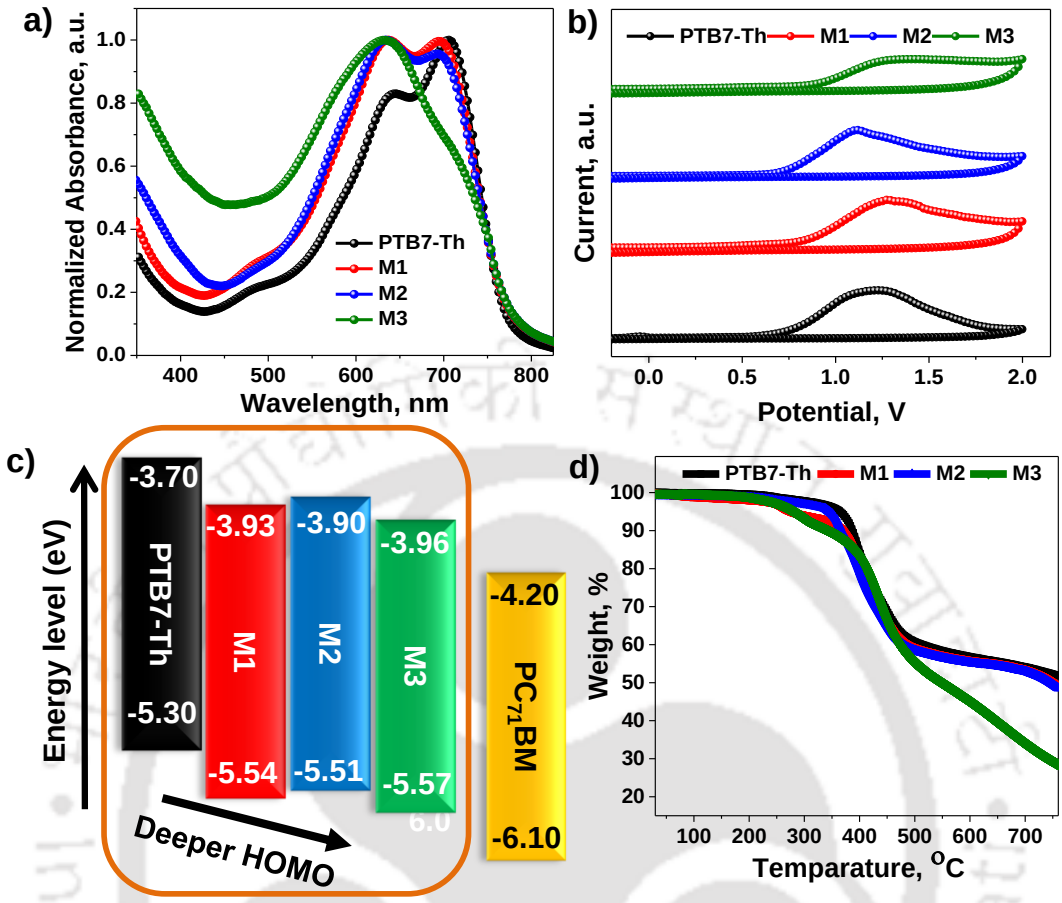

Figure 3.1: a) UV-visible absorption of polymer films, b) CV plots of polymer using three-electrode system, c) Energy band of polymers and $PC_{71}BM$, and d) TGA plots of polymers.

From the CV profile, HOMO energy level for PTB7-Th was determined to be -5.30 eV using the equation, E_{HOMO} = -e(E_{ox}+4.71) eV (Table 3.1).[27] For terpolymers M1, M2, and M3, HOMO level was deepened to -5.54, -5.51, and -5.57 eV, due to the incorporation of fluorinated monomers. This change in HOMO energy levels can substantially improve the V_{OC} of terpolymers based photovoltaic devices. A similar trend was also observed for LUMO levels of all polymers which were calculated to be -3.70, -3.93, -3.90, and -3.96 eV for PTB7-Th, M1, M2, and M3, respectively (Figure 3.1c). Further, the thermal stability of all polymers was studied under inert condition utilizing thermogravimetric analysis (TGA) (Figure 3.1d). The terpolymers exhibited marginally lower thermal decomposition temperature (T_d) compared to the PTB7-Th ($T_{d,10}$ = 377 °C) which can be attributed to the intrinsic property of third monomers incorporated in polymer backbone.

Table 3.1: Summary of photophysical and electrochemical properties of polymers

Polymers	λ_{film}, nm	$T_{d,10}$, °C	HOMO, eV	LUMO, eV	E_g, eV	μ_h, $cm^2V^{-1}s^{-1}$	μ_e, $cm^2V^{-1}s^{-1}$	μ_h/μ_e
PTB7-Th	644, 707	377	-5.30	-3.70	1.60	2.1×10^{-4}	1.7×10^{-4}	1.24
M1	636,696	372	-5.54	-3.93	1.61	2.7×10^{-4}	2.2×10^{-4}	1.23
M2	635,694	366	-5.51	-3.90	1.61	2.2×10^{-4}	1.5×10^{-4}	1.47
M3	634	345	-5.57	-3.96	1.61	1.5×10^{-4}	0.9×10^{-4}	1.66

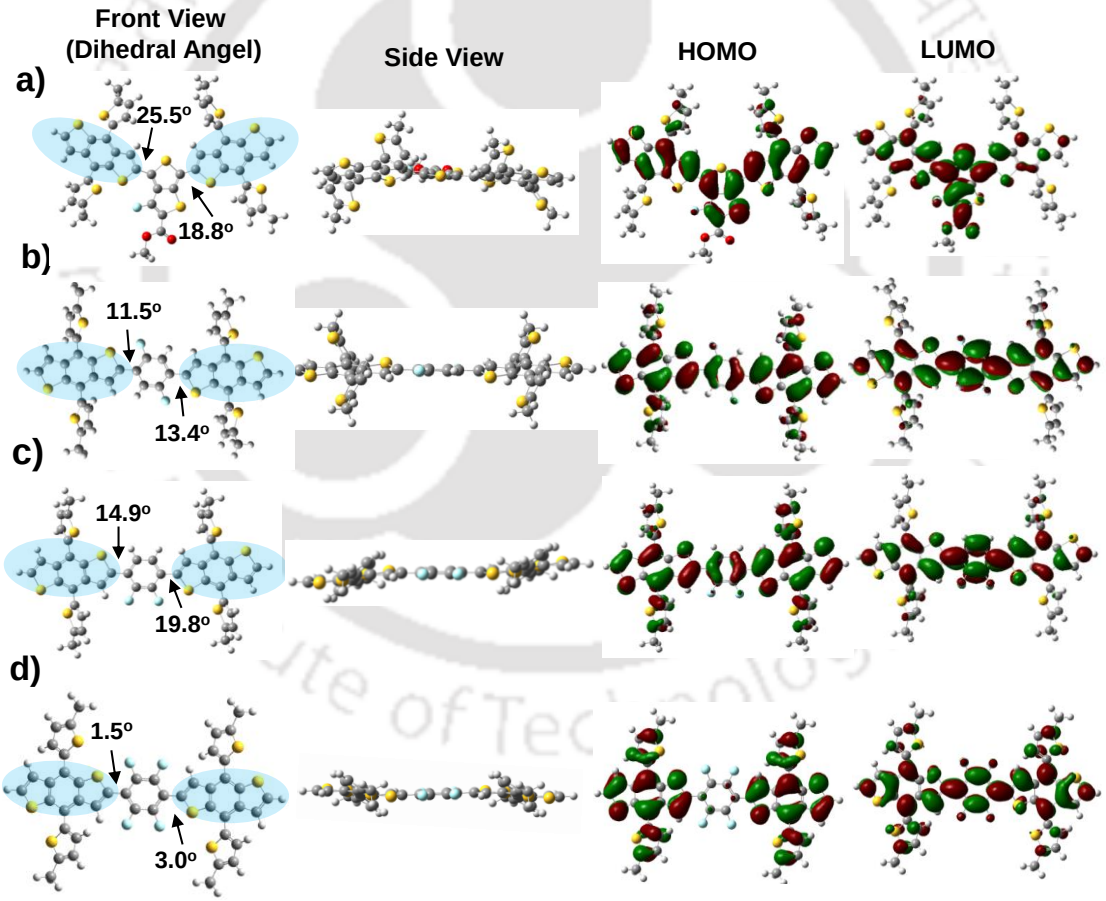

Figure 3.2: Optimized molecular orientation in DFT (top and side view) with energy orbitals (HOMO and LUMO) of the polymer backbone for a) FTT, b) FPM1, c) FPM2, and d) FPM3 based molecular models bonded with BDT-Th units.

All the polymers showed very high thermal stability and 10% decomposition of materials happened above 345 °C which was well-suited for room temperature processed PSC fabrication. Density functional theory (DFT) was employed with basis set of B3LYP/6-31G (d, p) to further elucidate the dihedral angle, noncovalent interactions and conformational lock in molecular architecture of polymers. The dihedral angle was found to be 25.5° and 18.8° for BDT-Th and FTT unit representing the molecular structure of PTB7-Th, which was reduced as varying amounts of FPMs were incorporated in the terpolymer.

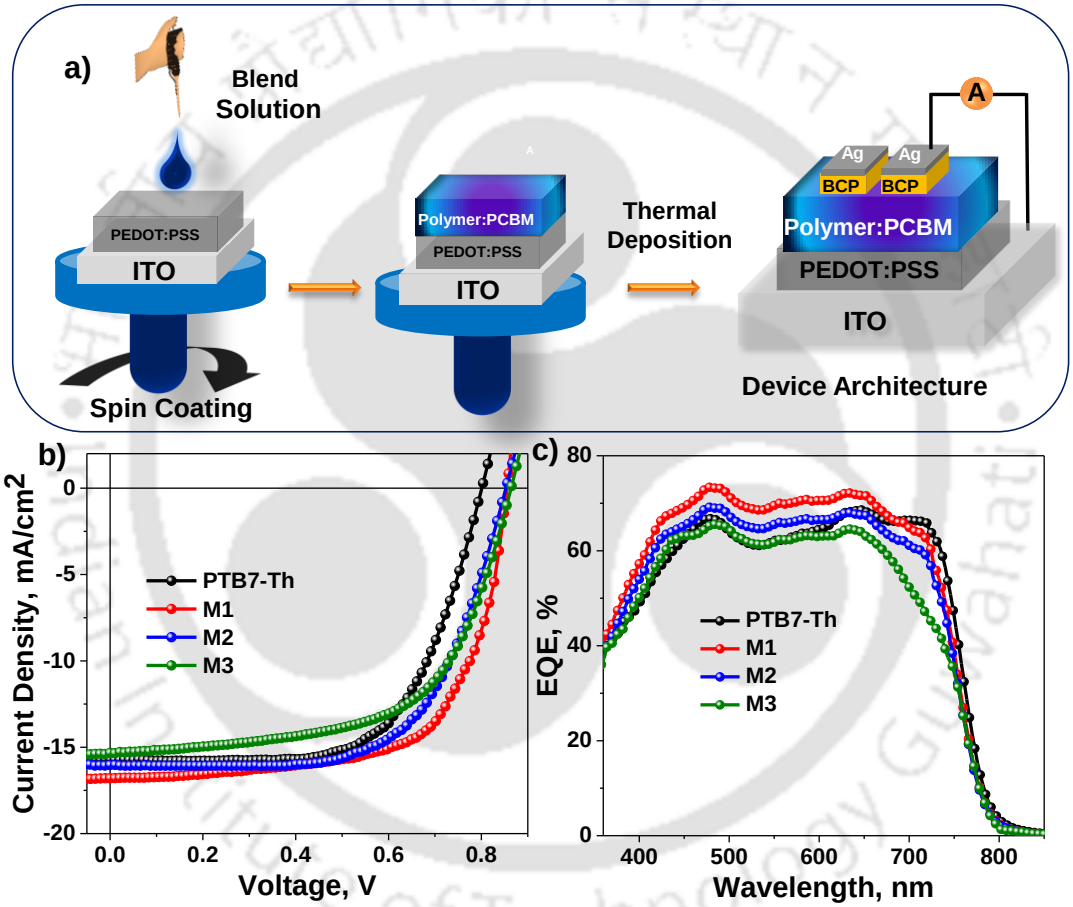

Figure 3.3: a) Schematic representation of the PSC fabrication method, b) Current Density–Voltage plot, and c) EQE profiles of PSCs.

For BDT-Th-FPM-BDT-Th molecular system, the dihedral angle was lowered to (11.5° & 13.4°), (14.9° & 19.8°), and (1.5° & 3.0°) for FPM1, FPM2, and FPM3 incorporated molecular systems, respectively (Figure 3.2a-d). FPM3 appeared to be the strongest monomer which had a dominant impact to modify the electronic distribution in HOMO and LUMO energy levels along

with lowest dihedral angle. The side view of optimized structures displayed that terpolymers were expected to have more organized packing in thin films. This also indicated that the fluorine induced varied non-covalent interactions substantially reduced the dihedral angle which can tune the morphology of polymer blends to enhance the charge transport property. To further understand the influence of FPMs on photovoltaic performance, PSCs were fabricated (Figure 3.3a) utilizing polymers and $PC_{71}BM$ blend with a conventional architecture of ITO/PEDOT:PSS/Photoactive layer/BCP/Ag.[28] 1,8-diiodooctane (DIO) was used as an additive with chlorobenzene to deposit the $PC_{71}BM$ based photoactive layer and fabricate the PSCs at room temperature. The details of fabrication methods are illustrated in experimental section 3.4. The *J–V* (current density–voltage) characteristic profile revealed that PTB7-Th, M1, M2, and M3 based PSCs achieved the PCE of 8.19%, 9.48%, 8.80%, and 8.13%, respectively.

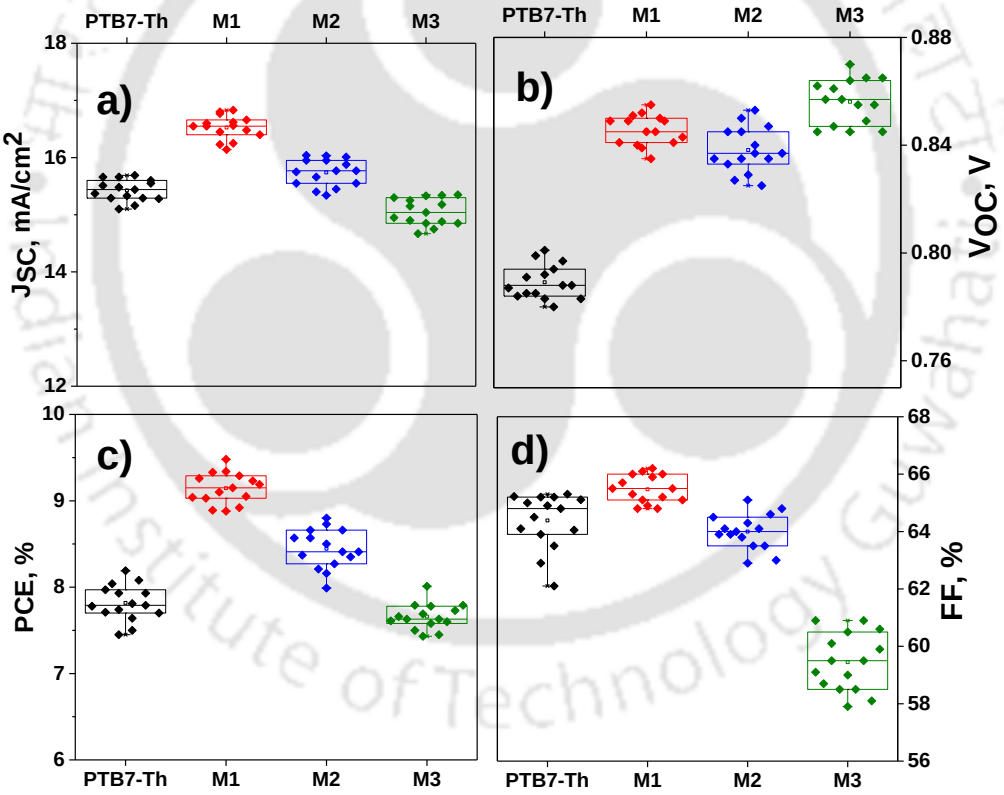

Figure 3.4: Box chart of a) J_{SC} b) V_{OC}, c) PCE, and d) FF for PSCs fabricated using different polymer blends.

A box chart for varied photovoltaic parameters is included for all polymer blends in as Figure 3.4a-d which also represents the reproducibility of these PSCs. Moreover, a significant

enhancement of current density (J_{SC}) and V_{OC} was achieved for M1 and M2 based PSCs. The V_{OC} of fabricated PSCs were found to be 0.801 V, 0.855 V, 0.853 V, and 0.864 V for PTB7-Th, M1, M2 and M3 based devices (Figure 3.3b). This improvement of V_{OC} can be correlated with the lower HOMO energy level of terpolymers in comparison to the PTB7-Th. The summary of all photovoltaic parameters for varied blends are included in Table 3.2. FPM induced conformational lock in polymer backbone contributed to enhance the J_{SC} for the M1 and M2 based PSCs. Contrarily, M3 based PSCs displayed inferior photovoltaic performances which was majorly due to its lower J_{SC} and fill factor (FF). The lower J_{SC} of M3 based PSCs can be correlated with its blue shifted absorption peak maxima. The mobility and morphological study can provide better insight about the trends in photovoltaic performance of PSCs. Further, the external quantum efficiency (EQE) spectra of PSCs were analyzed (Figure 3.3c). M1 based blend achieved highest EQE, compared to other blends. The integrated J_{SC} from EQE was found to be well-matched with results of *J-V* profile for all the blends.

Table 3.2: Photovoltaic Parameters of PSCs

Donor : Acceptor[a]	J_{SC}, mA/cm^2	V_{OC}, V	FF, %	PCE, % (Average)[b]
PTB7-Th:$PC_{71}BM$	15.69	0.801	65.2	8.19 (7.82 ±0.20)
M1:$PC_{71}BM$	16.83	0.855	65.9	9.48 (9.15±0.18)
M2:$PC_{71}BM$	16.03	0.853	64.3	8.80 (8.45 ±0.22)
M3:$PC_{71}BM$	15.33	0.864	60.5	8.13 (7.67±0.17)

[a] Polymer:Acceptor = 1:1.5; [b]Average of 15 devices.

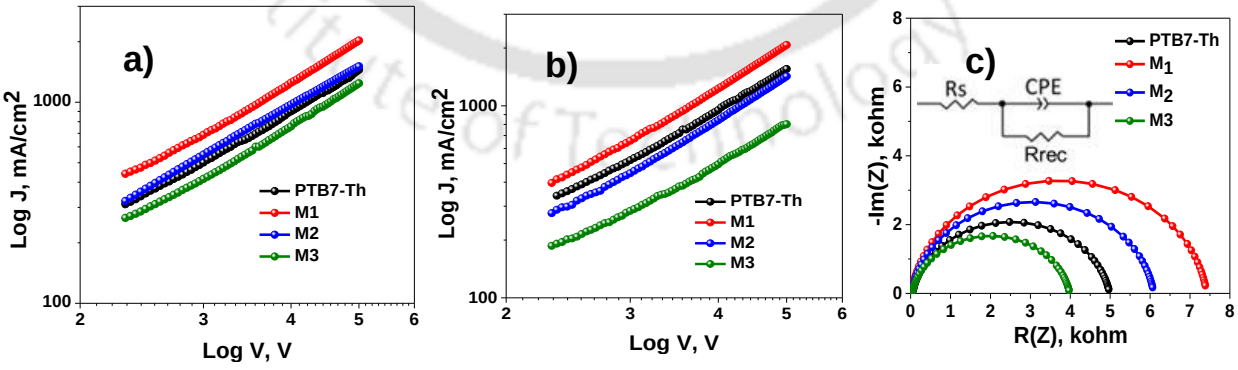

Figure 3.5: SCLC plot for a) hole only device, b) electron only device, and c) Impedance spectra of PSCs with the equivalent circuit in the inset.

To estimate the hole mobility (μ_h) of polymer based blends, a device architecture comprising ITO/PEDOT:PSS/Polymer:$PC_{71}BM$/Cu was utilized (Figure 3.5a).[29] The hole mobility was calculated to be 2.1×10^{-4}, 2.7×10^{-4}, 2.2×10^{-4}, and 1.5×10^{-4} $cm^2V^{-1}S^{-1}$, respectively for PTB7-Th, M1, M2, and M3 based blends by the space charge limited current (SCLC) method (Table 3.1). The hole mobility was enhanced for M1 and M2 which justifies the changes in *J-V* profile parameters of terpolymer based PSCs. Then, the electron mobility (μ_e) was estimated for the blend films utilizing electron-only devices with reported architecture of ITO/ZnO/Polymer Blend/Ca/Al.[13] For PTB7-Th, M1, M2, and M3 based blends, the electron mobilities were determined to be 1.7×10^{-4}, 2.2×10^{-4}, 1.5×10^{-4}, and 0.9×10^{-4} $cm^2V^{-1}S^{-1}$ (Figure 3.5b). Although both M1 and M2 terpolymer contain regioisomeric fluoroarene monomers in backbone, FPM1 more efficiently reduced the dihedral angle in M1 backbone, compared to the FPM2 in M2 polymer. The backbone planarity of M1 polymer assisted to achieve higher mobility than M2 polymer which also boosted the photovoltaic performance of M1 blend, compared to other polymer blends.[30-32] Moreover, due to the well-balanced charge carrier mobility of PTB7-Th, M1, and M2 based PSCs achieved higher FF compared to M3 based PSCs (Table 3.1).

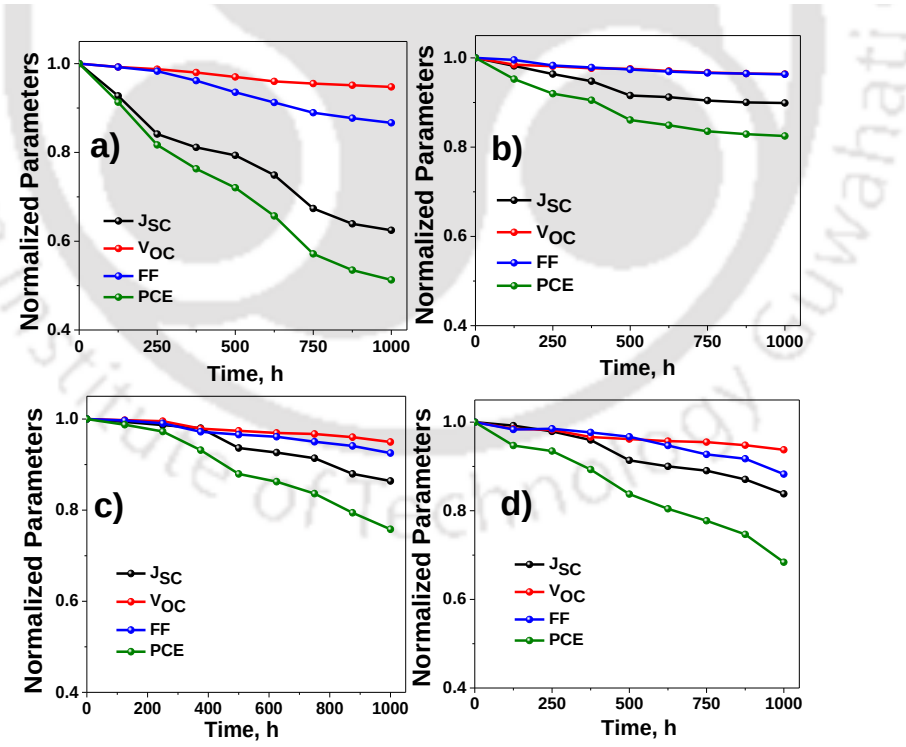

Figure 3.6: The analysis of PSCs performance stability for 1000 h under ambient condition for a) PTB7-Th:$PC_{71}BM$, b) M1:$PC_{71}BM$, c) M2:$PC_{71}BM$, and d) M3:$PC_{71}BM$ based blend.

To gain better insight about the interfacial charge carrier kinetics and recombination, the electrochemical impedance spectroscopy (EIS) was analyzed for all the polymer blends under dark condition (Figure 3.5c). The Nyquist plots were fitted with equivalent circuit presented in inset. The series resistance (R_S) and recombination resistance (R_{rec}) were determined for all PSCs.[33] The R_S was reduced to 19.10 Ω for M1 based blend from 45.22 Ω for PTB7-Th based devices. For M2 and M3 based blends, R_S was found to be 26.5 Ω and 46.10 Ω, respectively which was higher than M1 based device. Moreover, the R_{rec} was estimated to be 4943 Ω, 7400 Ω, 6065 Ω, and 3942 Ω for PTB7-Th, M1, M2, and M3 based blend, respectively. This indicated that M1 based PSCs suffered from least charge carrier recombination compared to the other blends which also validated the superior photovoltaic performance of M1 based blend. To further elucidate the impact of FPM incorporation on ambient stability of devices, the PSCs with varied polymer blends were exposed to ambient condition with relative humidity (RH) of 45 ± 5% without encapsulation. Figure 3.6a-d presents the variations of photovoltaic parameters for all the blends after ambient exposure.

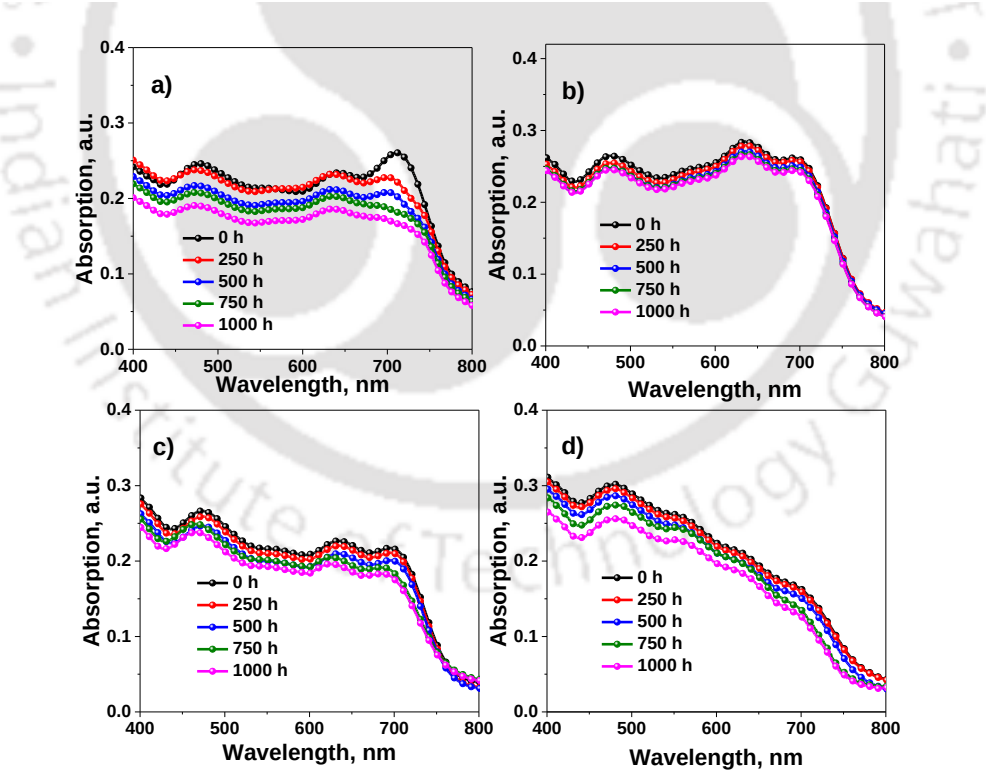

Figure 3.7: UV-visible absorption of a) PTB7-Th:$PC_{71}BM$, b) M1:$PC_{71}BM$, c) M2:$PC_{71}BM$, and d) M3:$PC_{71}BM$ blend films aged under ambient condition for 1000 h.

The PTB7-Th based device was able to maintain only 51% of its initial efficiency after 1000 h of ambient exposure. Contrarily, the terpolymer based devices exhibited better ambient stability. M1, M2, and M3 based PSCs retained PCE of 82%, 75%, and 65% of its initial efficiency, respectively. A major decline was observed in J_{SC} and FF of the PTB7-Th based device after exposing to ambient condition which can be correlated with the gradual degradation in molecular structure and active layer morphology triggered by ambient condition. However, the rate of degradation was significantly reduced for terpolymer based devices and M1 based PSCs exhibited relatively higher ambient stability in comparison to the other polymer blends. To understand the reasons behind the sharp reduction of J_{SC} after ambient exposure in PTB7-Th, we analyzed the change in absorption profile of PTB7-Th:$PC_{71}BM$ blend along with other polymer blends for 1000 h in ambient condition (Figure 3.7a-d). Due to the ambient condition mediated structural degradation of active layer blend, a gradual decline was observed in the intensity of absorption spectra for all blends.[23] However, the rate of degradation was much lower for terpolymer based blends. This indicates that FPM induced non-covalent interactions diminished the extent of degradation significantly. M1 based blend film exhibited most stable absorption profile in comparison to other blend films which assisted the M1 based PSCs to retain higher J_{SC} compared to other blends under ambient condition. To further attain better insight about the impact of FPM incorporation on surface morphology of active layer, the blend films were probed with atomic force microscope (AFM). Figure 3.8ai-di display AFM images for all polymer blends. PTB7-Th, M1, and M2 based films displayed very smooth films with well distributed intermixed nano-morphology. However, the M3 based blend film exhibited lesser intermixed morphology that can be attributed to the lower solubility of the polymer and the stronger aggregation induced by tetra-fluorinated phenyl monomer in M3 polymer backbone. The RMS roughness was observed to be 1.3 nm, 1.1 nm, 1.2 nm, and 0.8 nm in AFM height images of PTB7-Th, M1, M2, and M3 based blend films. The smoothness of blend thin films was improved with the FPM incorporation which was expected due to the FPM induced intra/intermolecular non-covalent interactions (sulphur-fluorine, hydrogen-fluorine, oxygen-fluorine etc.). The surface roughness trend for polymer blend films was also consistent with the DFT observations. FPMs finely

modulated the dihedral angle in polymer backbone which further controlled the blend morphology of terpolymers and photovoltaic performance.

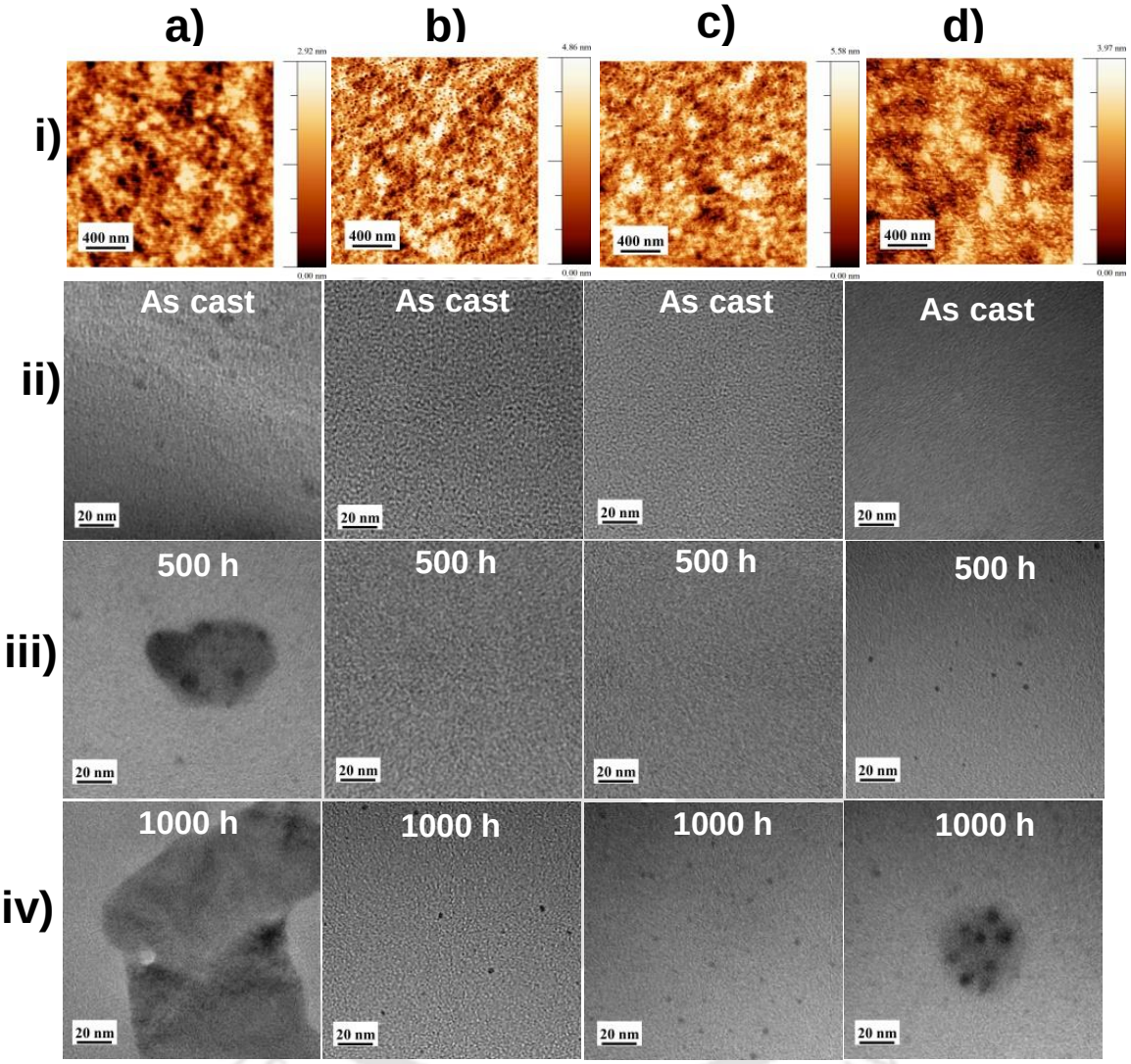

Figure 3.8: Morphological analysis of a) PTB7-Th:$PC_{71}BM$, b) M1:$PC_{71}BM$, c) M2:$PC_{71}BM$, and d) M3:$PC_{71}BM$ blend film where i) AFM height image (2×2 μm) of as casted film, ii) FETEM image of as casted blend film, iii) FETEM image after 500 h of ambient exposure, and iv) FETEM image after 1000 h of ambient exposure.

The photoactive layers with lower RMS roughness and intermixed morphology facilitated the enhanced charge transport in the M1 and M2 based PSCs. To further gain more insight about active layer nano-morphology, Field Emission Transmission Electron Microscope (FETEM) was employed (Figure 3.8a-d(ii-iv)). The PTB7-Th:$PC_{71}BM$ blend

displayed almost homogenous surface morphology with very less contrast between the donor and acceptor in photoactive layer blend.[34,35] Contrarily, M1 based blend film exhibited better phase separation with evenly distributed intermixed morphology. For M2 and M3 blend, the phase separation and the contrast between donor and acceptor was reduced compared to M1 blend. FPM1 as third monomer tuned the morphology optimally to gain suitable morphology which assisted the superior photovoltaic performance of M1:$PC_{71}BM$ based blend. To further illustrate the correlation between the ambient stability of PSCs and surface morphology of blend films, FETEM images of polymer:$PC_{71}BM$ blends were analyzed for aged films under ambient condition. FETEM images of PTB7-Th blend film displayed ~100 nm sized cluster after 500 h of ambient ageing due to the morphological degradation. M1 and M2 based blends were relatively stable (morphological stability) under ambient condition even after 500 h due to FPM induced non-covalent interactions in blend films. In M3 based blend films, tiny sized (3-4 nm) clusters appeared after 500 h of ambient exposure which exhibited the instability of phase domain. The black cluster size increased significantly in PTB7-Th and M3 based film after 1000 h of ambient exposure. Though both M1 and M2 films displayed the presence of tiny sized clusters after 1000 h of ageing in ambient condition, the number of black clusters was very less for M1:$PC_{71}BM$ blend. This indicates that 2,5-difluorobenzene as a monomer induced strong intra/inter molecular interactions in M1 based blend film which provided an improved phase domain stability overcoming the adverse impact of ambient condition. This unique strategy of subtle incorporation of fluorinated phenyl derivatives in polymer backbone proficiently levitated the long term durability of PSCs along with its photovoltaic performance.

3.3 Conclusion

In summary, we have elucidated the impact of fluorinated phenyl derivative incorporations to comprehend the correlation between polymer structure and its photovoltaic property. Three random terpolymers were synthesized using varied fluorinated phenyl derivatives as third monomer to finely regulate the photo physical properties and surface morphology of photoactive layers. The incorporation of FPM in the terpolymers effectively modulated the energy level alignment, photon absorption, and

film morphology of photoactive layer. These changes collectively enhanced the photovoltaic performance of terpolymer based PSCs. Higher J_{SC} was achieved for M1 and M2 based blend because of its low dihedral angle and uniformly separated phase with nano-morphology. Contrarily, due to the lower absorption at NIR region and relatively poor blend morphology of M3 blend, it exhibited overall lower photovoltaic performance. All terpolymers displayed significantly enhanced V_{OC} compared to PTB7-Th based PSCs due to their deeper HOMO levels. This improvement of J_{SC} and V_{OC} collectively enhanced the PCE for M1 and M2 based blend up to 9.48% and 8.80%, respectively. Moreover, M1 based blend achieved highest ambient stability and retained 82% of its initial PCE in comparison to 51%, 75%, and 68% retention for PTB7-Th, M2, and M3 based blend, respectively. This indicates about the influence of FPM derivatives in suppressing morphological degradations triggered by ambient condition. This efficient strategy can be widely applied to further explore the impacts of fluorinated monomers to develop highly efficacious and durable photovoltaic materials for the future generation.

3.4 Experimental Section

3.4.1 Materials

The monomers of 2-Ethylhexyl-4,6-dibromo-3-fluorothieno[3,4-b]thiophene-2-carboxylate (R1), 1,1′-[4,8-Bis[5-(2-ethylhexyl)-2-thienyl]benzo[1,2-b:4,5 b′]dithiophene-2,6-diyl]bis[1,1,1-trimethylstannane] (R2), and $PC_{71}BM$ were purchased from Lumtec. 1,4-dibromo-2,5-difluorobenzene, 1,4-dibromo-2,3-difluorobenzene, 1,4-dibromo-2,3,5,6-tetrafluorobenzene, and $Pd(PPh_3)_4$ were procured from Sigma Aldrich. The hole transporting material (HTM), Poly(3,4-ethylenedioxythiophene)-poly(styrenesulfonate) (PEDOT:PSS, PVP AI 4083) was obtained from Clevios.

3.4.2 Instruments

^{1}H NMR spectra of the polymers were analyzed by Bruker 400 MHz spectrometers. Absorbance spectra of synthesized polymers film (deposited from chlorobenzene on a pre cleaned glass slide and vacuum dried) were recorded using a Perkin–Elmer Lambda-35 UV-visible spectrophotometer. Gel-permeation chromatography (GPC) measurements were performed on a Waters 515 chromatograph with tetrahydrofuran as eluent and polystyrene as standard. Thermal stabilities of all polymers under nitrogen atmosphere have been analyzed by thermogravimetric

analysis (TGA) in a Netzch (STA 449, Jupiter) instrument at a heating rate of 10 °C/minute. To determine oxidation potential of polymers, three electrode was used and polymer film was coated on a glassy carbon electrode. The thin film of PEDOT:PSS and the active layer blend were deposited on ITO-coated glass substrate by spin coating technique utilizing a Laurell and Spin 150 spin. A JEOL 2100F FETEM was utilized for morphological analysis of Blend films. A Veeco Dektak 150 Surface Profilometer was used to measure thicknesses of the thin films. AFM images of the thin active layer films were recorded by Agilent 5500-STM instrument. All the electrical parameters were characterized by Keithley-2400 digital source meter. Newport, Oriel Sol 3A solar simulator with an Oriel 500 W xenon lamp, connected to AM 1.5 Globe filter, was used as solar cell characterization. Newport Oriel IQE-200 instrument was used for external quantum efficiency (EQE) measurement.

3.4.3 General Synthesis Procedure

To synthesize these polymers, we followed previously reported Stille polycondensation based methods. R1, R2, and R3 (third monomers) were weighed into a dry 50 mL Schlenk tube equipped with a magnetic stirrer. After that, $Pd(PPh_3)_4$ was added, the mixture was degassed three times, and then toluene and DMF (4:1) were added. The reaction mixture was stirred for 15 hours under argon at 120 °C. After cooling down to room temperature, the dense black gel was precipitated in 300 mL of MeOH and then stirred for few minutes. By filtration the resulting polymer was collected and washed with MeOH. Further purification was done via Soxhlet extraction sequentially with MeOH, Acetone, n-Hexane, and $CHCl_3$. Then the $CHCl_3$ part was concentrated. Then it was again precipitated and used for device fabrication and other studies.

Synthesis of PTB7-Th: The polymer, PTB7-Th was synthesized under the same reaction conditions with R1 (0.2 mmol) and R2 (0.2 mmol) with Yield of 71% (dark blue solid) ^{1}H NMR (400 MHz, $CDCl_3$) δ (ppm): 7.38-8.10 (br, 4 H), 6.40-7.20 (br, 2 H), 4.00-4.50 (br, 2 H), 2.50-3.55 (br, 4 H), 0.45-1.95 (br, 45 H).

GPC for PTB7-Th: M_w =149 kDa, M_n= 50 kDa, and Đ= 3.01.

Synthesis of Terpolymers: M1, M2, and M3 were synthesized under the same reaction conditions with R1 (0.19 mmol), R2 (0.2 mmol), and R3 (0.01 mmol) with Yield of 70-79% (black solid).

^{1}H NMR of M1: (400 MHz, $CDCl_3$) δ (ppm): 7.38-8.10 (br, 4 H), 6.40-7.20 (br, 2 H), 4.00-4.50 (br, 2 H), 2.50-3.55 (br, 4 H), 0.45-1.95 (br, 45 H).

^{1}H NMR of M2: (400 MHz, $CDCl_3$) δ (ppm): 7.38-8.10 (br, 4 H), 6.40-7.20 (br, 2 H), 4.00-4.50 (br, 2 H), 2.50-3.55 (br, 4 H), 0.45-1.95 (br, 45 H).

^{1}H NMR of M3: (400 MHz, $CDCl_3$) δ (ppm): 7.38-8.10 (br, 4 H), 6.40-7.20 (br, 2 H), 4.00-4.50 (br, 2 H), 2.50-3.55 (br, 4 H), 0.45-1.95 (br, 45 H).

GPC for M1 polymer: M_w = 261 kDa, M_n= 103 kDa, and Đ= 2.52.

GPC for M2 polymer: M_w = 241 kDa, M_n= 102 kDa, and Đ= 2.38.

GPC for M3 polymer: M_w = 107 kDa, M_n= 38 kDa, and Đ= 2.85.

3.4.4 Device fabrication

PSCs were fabricated with the conventional architecture of ITO/PEDOT:PSS/Active layer blend/BCP/Silver. The donor–acceptor blend solution was prepared using chlorobenzene (CB) as a processing solvent at a concentration of 35 mg mL^{-1} (D/A ratio 1:1.5) for $PC_{71}BM$ blend. Then it was kept at 50 °C and constantly stirred for 5-6 h, and a small extent (3%, volume) of 1,8-diiodooctane (DIO) was added to it 10 min before spin coating. Patterned ITO glass substrates were cleaned using deionized (DI) water, acetone, and isopropanol sequentially. Then they were dried and UV–ozone treatment was carried out for 15 min. Further, PEDOT:PSS was spin-coated on the ITO substrate at 4000 rpm and then annealed at 150 °C for 20 min. The blend solutions were spin-coated at 3000 rpm followed by methanol treatment for the removal of DIO. BCP (~10 nm) and silver (~100 nm) were thermally deposited. All devices had a cell area of 0.06 cm^2.[7] Hole and electron mobility of polymers were calculated using SCLC method where slope values were ~2 for all the plots.

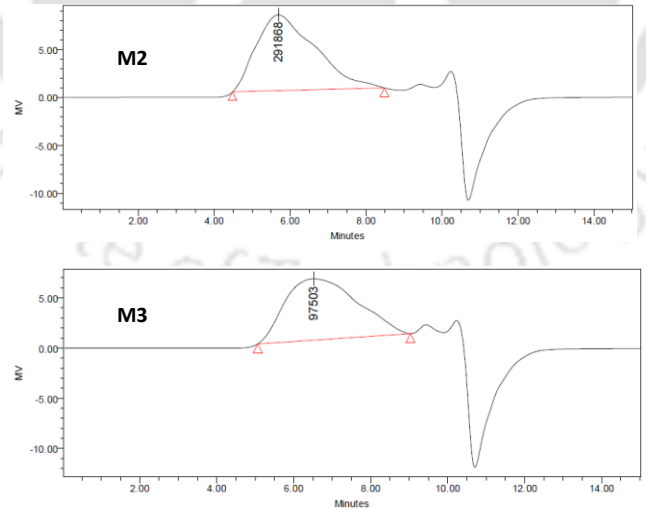

Figure 3.9: GPC of M2 and M3.

3.5 References

(1) A. J. Heeger, *Adv. Mater.*, 2014, **26**, 10-28.

(2) G. Li, R. Zhu and Y. Yang, *Nat. Photonics*, 2012, **6**, 153-161.

(3) K. Fukuda, K. Yu and T. Someya, *Adv. Energy Mater.*, 2020, **10**, 2000765.

(4) F. C. Krebs, T. Tromholt and M. Jørgensen, *Nanoscale*, 2010, **2**, 873-886.

(5) F. C. Krebs, M. Jørgensen, K. Norrman, O. Hagemann, J. Alstrup, T. D. Nielsen, J. Fyenbo, K. Larsen and J. Kristensen, *Sol. Energy Mater. Sol. Cells*, 2009, **93**, 422-441.

(6) J. Chen and Y. Cao, *Acc. Chem. Res.*, 2009, **42**, 1709-1718.

(7) R. Garai, M. Adil Afroz, R. K. Gupta, A. Choudhury and P. K. Iyer, *ACS Omega*, 2020, **5**, 2747-2754.

(8) H. Fu, Z. Wang and Y. Sun, *Angew. Chem., Int. Ed*, 2019, **58**, 4442-4453.

(9) J. Yuan, Y. Zhang, L. Zhou, G. Zhang, H.-L. Yip, T.-K. Lau, X. Lu, C. Zhu, H. Peng, P. A. Johnson, M. Leclerc, Y. Cao, J. Ulanski, Y. Li and Y. Zou, *Joule*, 2019, **3**, 1140-1151.

(10) C. An, Z. Zheng and J. Hou, *Chem. Commun.*, 2020, **56**, 4750-4760.

(11) H. Yao, L. Ye, H. Zhang, S. Li, S. Zhang and J. Hou, *Chem. Rev.*, 2016, **116**, 7397-7457.

(12) J. Mei and Z. Bao, *Chem. Mater.*, 2014, **26**, 604-615.

(13) R. K. Gupta, R. Garai, M. A. Afroz and P. K. Iyer, *J. Mater. Chem. C*, 2020, **8**, 8191-8198.

(14) H. Jiang, F. Pan, L. Zhang, X. Zhou, Z. Wang, Y. Nian, C. Liu, W. Tang, Q. Ma, Z. Ni, M. Chen, W. Ma, Y. Cao and J. Chen, *ACS Appl. Mater. Interfaces*, 2019, **11**, 29094-29104.

(15) G. E. Park, S. Choi, S. Y. Park, D. H. Lee, M. J. Cho and D. H. Choi, *Adv. Energy Mater.*, 2017, **7**, 1700566.

(16) W. Su, Y. Meng, X. Guo, Q. Fan, M. Zhang, Y. Jiang, Z. Xu, Y. Dai, B. Xie, F. Liu, M. Zhang, T. P. Russell and Y. Li, *J. Mater. Chem. A*, 2018, **6**, 16403-16411.

(17) W. Chen and Q. Zhang, *J. Mater. Chem. C*, 2017, **5**, 1275-1302.

(18) S.-H. Liao, H.-J. Jhuo, Y.-S. Cheng and S.-A. Chen, *Adv. Mater.*, 2013, **25**, 4766-4771.

(19) F. C. Löhrer, C. Senfter, C. J. Schaffer, J. Schlipf, D. Moseguí González, P. Zhang, S. V. Roth and P. Müller-Buschbaum, *Adv. Photonics Res.*, 2020, **1**, 2000047.

(20) Q. Liu, J. Toudert, F. Liu, P. Mantilla-Perez, M. M. Bajo, T. P. Russell and J. Martorell, *Adv. Energy Mater.*, 2017, **7**, 1701201.

(21) Y.-J. Hsieh, Y.-C. Huang, W.-S. Liu, Y.-A. Su, C.-S. Tsao, S.-P. Rwei and L. Wang, *ACS Appl. Mater. Interfaces*, 2017, **9**, 14808-14816.

(22) S. Kim, M. A. M. Rashid, T. Ko, K. Ahn, Y. Shin, S. Nah, M. H. Kim, B. Kim, K. Kwak and M. Cho, *J. Phys. Chem. C*, 2020, **124**, 2762-2770.

(23) T. L. Nguyen, H. Choi, S. J. Ko, M. A. Uddin, B. Walker, S. Yum, J. E. Jeong, M. H. Yun, T. J. Shin, S. Hwang, J. Y. Kim and H. Y. Woo, *Energy Environ. Sci.*, 2014, **7**, 3040-3051.

(24) M. Hossain, M. A. Afroz, R. Garai and P. K. Iyer, *Sustainable Energy Fuels*, 2021, **5**, 874-879.

(25) M. Hossain, R. Garai, R. K. Gupta, R. N. Arunagirinathan, P. K. Iyer, *J. Mater. Chem. C*, 2021, **9** 10406-10413.

(26) J. Yang, M. A. Uddin, Y. Tang, Y. Wang, Y. Wang, H. Su, R. Gao, Z.-K. Chen, J. Dai, H. Y. Woo and X. Guo, *ACS Appl. Mater. Interfaces*, 2018, **10**, 23235-23246.

(27) Z. Zhang, Y. Liu, J. Zhang, S. Feng, L. Wu, X. Gong, X. Xu, X. Chen and Z. Bo, *ACS Appl. Mater. Interfaces*, 2017, **9**, 23775-23781.

(28) Z. Huai, L. Wang, Y. Sun, R. Fan, S. Huang, X. Zhao, X. Li, G. Fu and S. Yang, *ACS Appl. Mater. Interfaces*, 2018, **10**, 5682-5692.

(29) R. Ratha, A. Singh, M. A. Afroz, R. K. Gupta, M. Baumgarten, K. Müllen and P. K. Iyer, *Synth. Met.*, 2019, **252**, 113-121.

(30) Y. Li, J. –W. Lee, M. Kim, C. Lee, Y. W. Lee, B. J. Kim, H. Y. Woo, *Polym. Chem.*, 2019, **10**, 395−402.

(31) Z. Li, K. Jiang, G. Yang, J. Y. L. Lai, T. Ma, J. Zhao, W. Ma, H. Yan, *Nat. Commun.*, 2016**, 7**, 13094.

(32) G. P. Kini, H. S. Park, S. J. Jeon, Y. W. Han, D. K. Moon, D. K., *Solar Energy*, 2020**, 207**, 720-728.

(33) A. Choudhury, R. K. Gupta, R. Garai, P. K. Iyer, *Adv. Mater. Interfaces*, 2021, **8**, 2100574.

(34) C. Duan, Z. Peng, F. J. M. Colberts, S. Pang, L. Ye, O. M. Awartani, K. H. Hendriks, H. Ade, M. M. Wienk, R. A. J. Janssen, *ACS Appl. Mater. Interfaces*, 2019**, 11**, 10794-10800.

(35) L. Zhang, N. Yi, W. Zhou, Z. Yu, F. Liu, Y. Chen, *Adv. Sci.*, 2019, **6** , 1900565.

Chapter 4

Fluoroarene Derivative Based Passivation of Perovskite Solar Cells Exhibiting Excellent Ambient and Thermo-stability Achieving Efficiency >20%

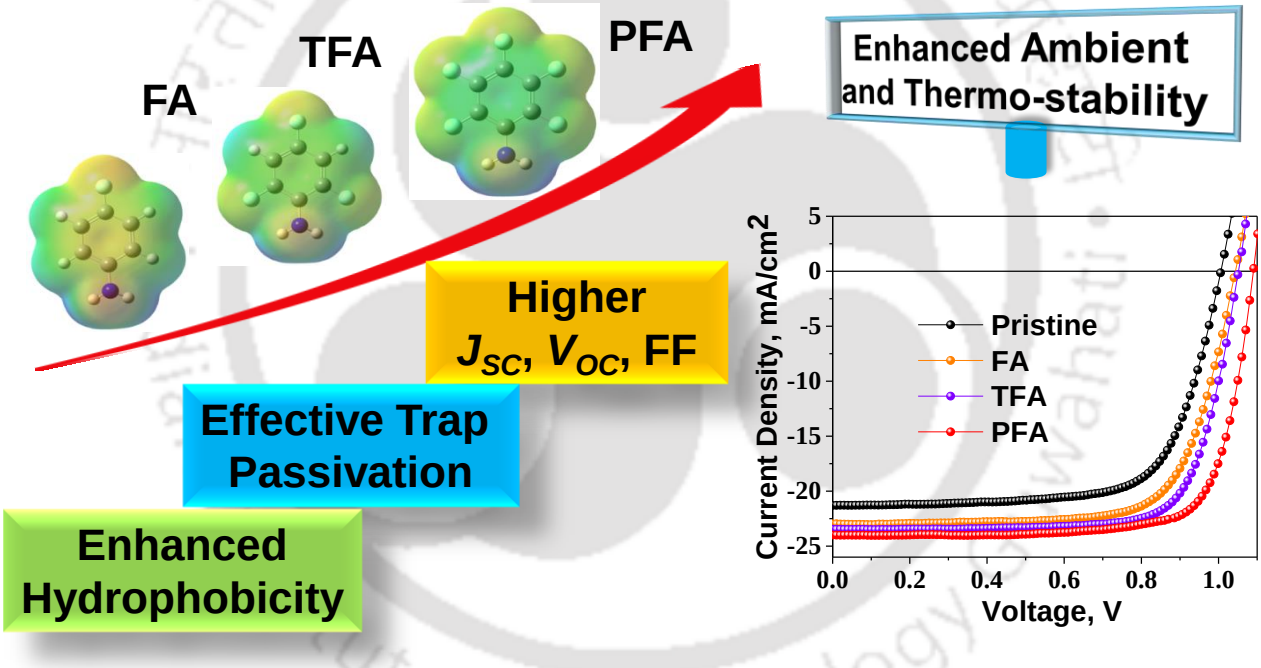

M. Hossain, R. Garai, R. K. Gupta, R. Narasimhan, and P. K. Iyer, *J. Mater. Chem. C*, 2021, ***9***, 10406-10413.

Abstract

Hybrid perovskite solar cells (PVSCs) are extremely susceptible to moisture and heat which restricts their commercial viability. Herein, three multifunctional fluoroaromatic amine additives i.e. 4-fluoroaniline (FA), 2,4,6-trifluoroaniline (TFA), and 2,3,4,5,6-pentafluoroaniline (PFA) are utilized as passivating additives to enhance stability of the perovskite films, thereby improving efficiency of PVSCs. Among these fluorinated aromatic amines, PFA most proficiently improved the efficiency along with the moisture and thermo-stability of $MAPbI_3$ based PVSCs. PFA significantly passivated the defects and assisted the better charge transport in the devices. The power conversion efficiency (PCE) enhanced beyond 20% for PFA passivated device, compared to the 15.08% of the pristine device without any passivation. Moreover, the PFA passivated device retained up to 87% PCE, compared to 26% for pristine device when exposed to relative humidity ~50% for 1000 h. The fluorine atoms attached to the passivation additives were able to provide the protection to PVSCs against the moisture induced erosion. Moreover, only 10% of efficiency was maintained by the pristine device in comparison to 82% for PFA based device after 20 h of heating at 100 °C inside the glovebox. Thus this work presented a generic approach to improve the overall stability and performances of PVSCs, thereby widening the possibility towards practical applications.

4.1 Introduction

Rapid progress in perovskite solar cells (PVSCs) in the past decade has brought about a new hope among the renewable technologies due to its incredibly high efficiency compared to its inorganic counterpart.[1] High power conversion efficiency (PCE) of PVSCs is due to their unique opto-electronic properties like broader absorption, band gap tunability, higher crystallinity and longer diffusion length of exciton.[2-7] Moreover, multifold PCE growth through easy solution processing in the last decade has stimulated worldwide intensive research in PVSCs.[1,8] However, the instability of perovskite crystal under heat and moisture hampers its further progress towards commercialization. The stoichiometric compositional imbalance during perovskite crystal formation and non-coordinated ions (I^-, MA^+, Pb^{2+} etc.) could create defects on the surface and the grain boundaries of perovskite.[9] These non-coordinated free ions can also interact with metal electrode which can generate more defects in the perovskite lattice resulting in higher

non-radiative recombination.[10] As a result, defect containing regions of the perovskite films are more prone to degrade in the presence of moisture under ambient condition. Thermal instability of PVSCs can be attributed to the crystal lattice expansion during heating which stimulates the moisture and oxygen penetration in the perovskite layer.[11]

Numerous techniques are utilized to counter the notorious instability of PVSCs, such as compositional tuning of photoactive layer,[12] encapsulation of the device,[13,14] device engineering[15-18], and molecular passivation[19,20]. Among all these techniques, the passivation of perovskite layer using a Lewis base is one of the most explored ones. Lewis bases as passivating agents in PVSCs can significantly suppress the impact of under-coordinated Pb^{2+} through the formation of Lewis base-Lewis acid adduct with Pb^{2+}.[21-26] Several aliphatic and aromatic amines were incorporated as passivation additives in PVSCs to minimize the defect of perovskite surface.[27,28] Furthermore, to enhance the ambient stability, fluorine containing passivating additives were also employed to increase the hydrophobicity of surface which can restrict the moisture penetration into the perovskite layer.[29-31] Fluorine containing molecules also have the ability to reduce heat induced instability of PVSCs by restricting the ion migration through the formation of hydrogen bonds with organic ions like MA^+ or FA^+.[31-33] This kind of non-covalent interactions can provide certain degree of structural rigidity to perovskite crystal lattice. Although, many techniques have been implemented for the defect passivation of PVSCs, the selection of suitable passivation additives remains crucial to modulate the perovskite crystallization and efficacious suppression of diverse kind of defects. Molecules with multiple functional groups have also been utilized as passivating additives because it can suppress the diverse defects in perovskite and provide higher stability.[29,34] To enhance the long-term durability of PVSCs and satisfy the prerequisite for real-life applications, the utilization of multifunctional additive is required which can efficiently minimize the defect density.

Herein, to suppress the wide range of defects in PVSCs, multifunctional passivation additives are utilized which contain varied number of fluorine atoms along with an amine group. Three multifunctional passivating additives i.e., 4-fluoroaniline (FA), 2,4,6-trifluoroaniline (TFA), and 2,3,4,5,6-pentafluoroaniline (PFA) were utilized to understand the combined influence of fluorine and amine group (Figure 4.10). Among these

fluorinated aromatic amines (FAAs), PFA based PVSCs exhibited superior hydrophobic property compared to other two amines. PFA passivation improved the stability (ambient and thermal) of $MAPbI_3$ based films significantly by restricting interaction of moisture with perovskite. This proficient strategy has contributed in improving the short circuit current (J_{SC}), open circuit voltage (V_{OC}), and fill factor (FF) simultaneously, which collectively enhanced the PCE beyond 20%. Due to the presence of amine and fluorine substituents on PFA molecule, trap states and ion migration were reduced simultaneously which also contributed in significant enhancement of moisture and thermo-stability of PVSCs compared to the pristine one.

4.2 Results and discussion

To analyze the impact of FAAs, thin layer of these amines were incorporated in PVSCs using spin coating method. In Figure 4.1a, the steps involved in sequential spin-coating of perovskite films and passivation additives are displayed. Firstly, the precursor solution of Methylammonium iodide (MAI) and PbI_2 were deposited on NiO_x coated FTO substrate by the well-known anti-solvent dripping method and after annealing instantly, $MAPbI_3$ film was formed. Subsequently, thin films of passivation additives were coated above $MAPbI_3$ film. The details of thin film coating for perovskite and other successive layers are included in experimental section (4.4). Firstly, the contact angle analysis was performed to understand the variation of hydrophobicity in pristine and FAA passivated perovskite surface (Figure 4.1b). Pristine perovskite surface showed contact angle of 37.4°. FA and TFA coated perovskite surfaces showed moderate contact angle of 48.8° and 56.3°, respectively. However, PFA coated surfaces showed highest extent of moisture resistivity with a contact angle of 73.4° as it had highest number of fluorine atoms compared to other analogous additives. Further, density functional theory (DFT) was utilized to understand molecular orientation and charge distribution on the molecular structure (Figure 4.1c). Although three FAAs have almost planar structure, the electrostatic potential (ESP) profile depicted that PFA has better uniformity in distribution of electron density over the aromatic ring. Moreover, the fluorine and amine group can interact simultaneously with under-coordinated perovskite ions to stabilize the lattice structure. Consequently, to analyze the impact of additives on crystallinity of perovskite films, varied concentration of PFA was coated on perovskite film and XRD study was

performed (Figure 4.2a). Three major intense peaks of (1 1 0), (2 2 0), and (3 1 0) perovskite planes were observed at 14.1°, 28.4°, and 31.8°, respectively in both pristine and PFA modified $MAPbI_3$ film. The intensity of these peaks enhanced gradually as the concentration of PFA was increased up to 2 mg/ml, however, when concentration reached beyond that level, the peak intensity was slightly decreased.

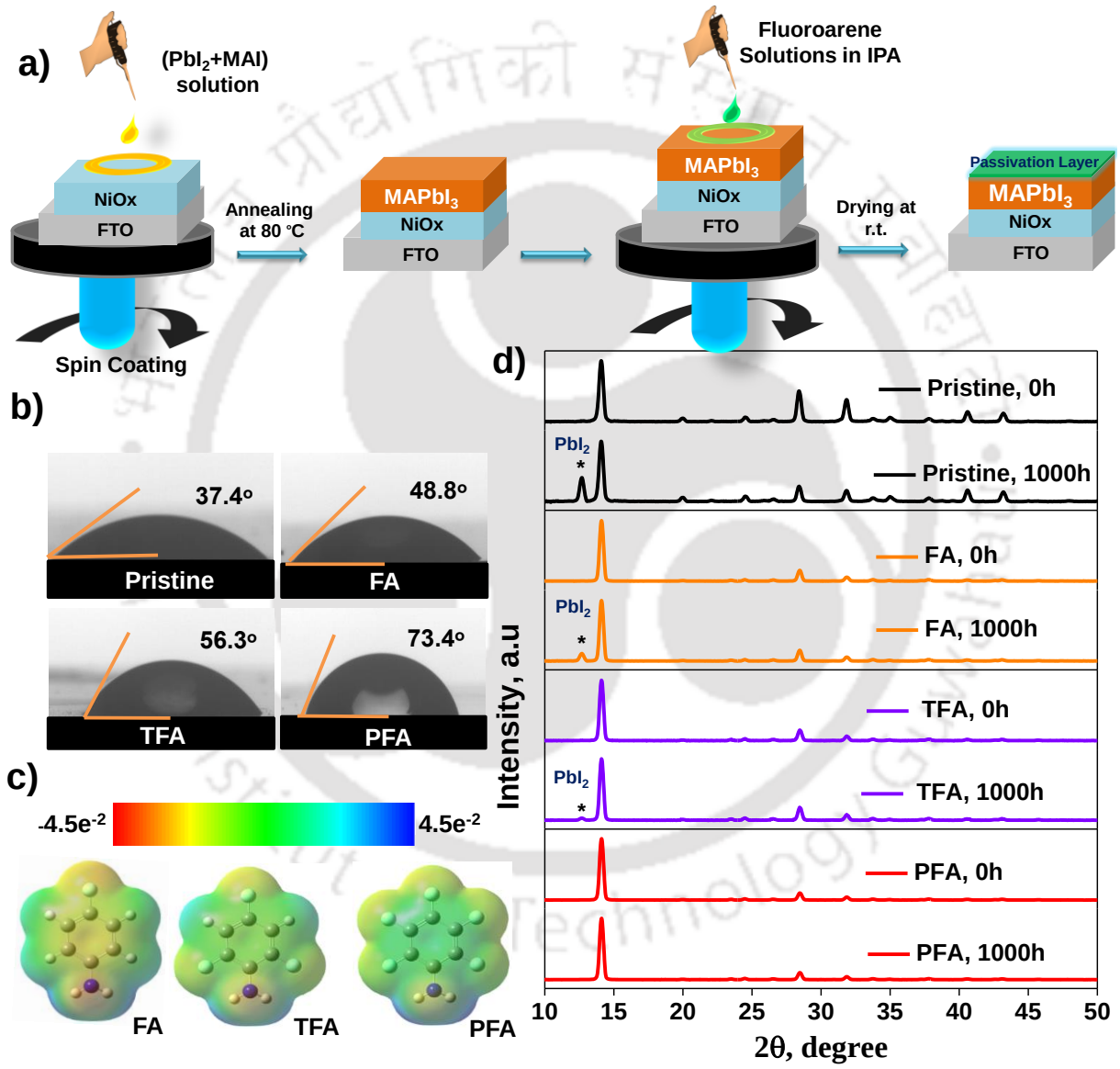

Figure 4.1: a) Schematic representation of perovskite and passivation layer thin film coating method, b) Contact angle of the pristine and passivated films FAA passivated films, c) ESP profile of FAAs, and d) XRD patterns of perovskite films stored in a relative humidity of 45 ± 5% up to 1000 h.

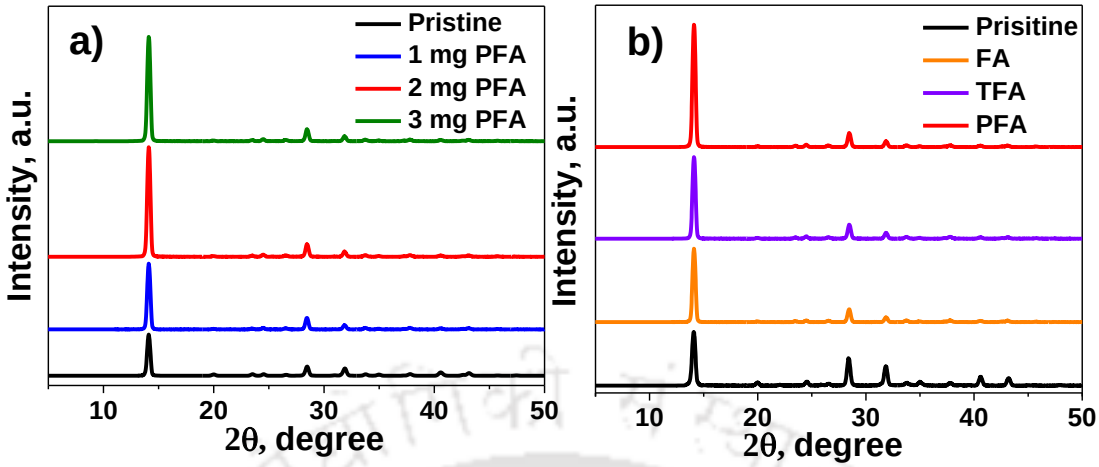

Figure 4.2: a) XRD patterns of perovskite film coated with varied concentration of PFA and b) XRD patterns of perovskite films coated with different FAAs.

The intensity enhancement of these characteristic peaks can be attributed to the improvement in crystallinity of perovskite film. Subsequently, to analyze the comparative long term durability of passivated perovskite film in ambient conditions, XRD study was also performed on FA, TFA, and PFA based passivated films where 2 mg/ml was considered as standard concentration for all the additives (Figure 4.2b). All the films were exposed to the environment with relative humidity of 45 ± 5% for a period of 1000 h (Figure 4.1d). The pristine film showed the indication of structural degradation and an intense peak at 12.7° was observed due to the PbI_2 phase in the film. Contrarily, the films passivated by PFA displayed much improved ambient stability compared to other analogous additives. Though, both FA and TFA based films lowered the rate of degradation compared to the pristine film, very small peak of PbI_2 was also present for FA and TFA based films after exposure of 1000 h in humid condition. The rate of degradation of these films can be directly correlated with hydrophobicity of their surface. PFA displayed superior passivation capability over other two FAAs which can also significantly influence the photo-physical and opto-electronic property of perovskite layer. To further investigate the impact of PFA, UV-visible spectra of thin films passivated with varied concentration of PFA were analyzed (Figure 4.3a). The gradual increase in concentration from 0 mg/ml to 2 mg/ml of PFA enhanced the intensity of

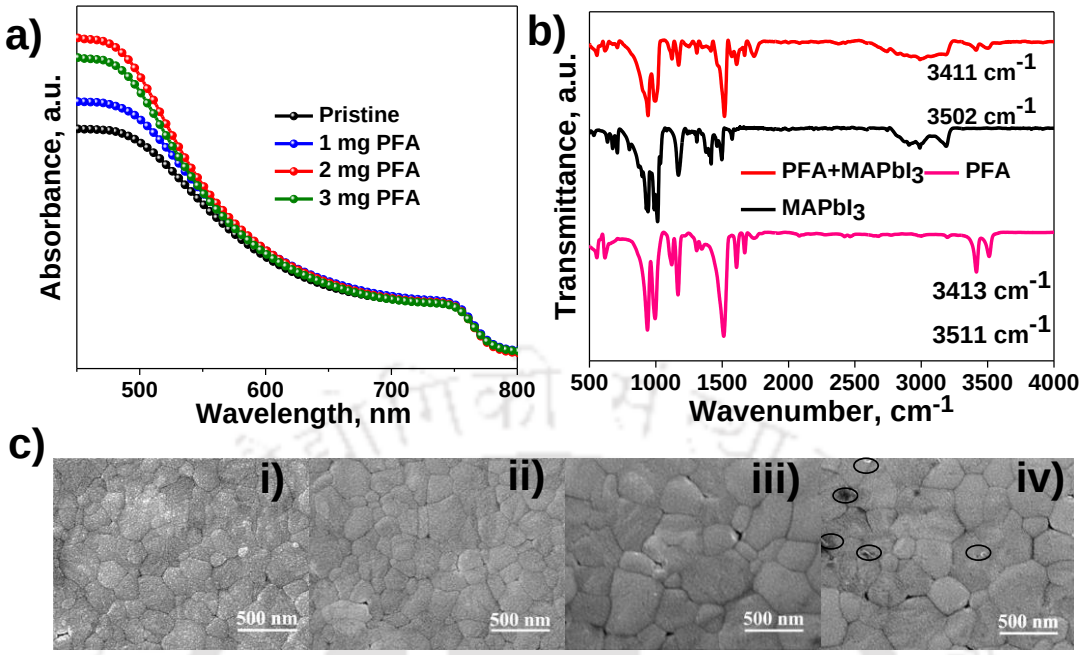

Figure 4.3: a) UV–vis absorption spectra of thin films of pristine and with varied concentration of PFA, b) FTIR spectra of PFA, $MAPbI_3$ film, and $MAPbI_3$ + PFA film, and c) FESEM images of i) Pristine, ii) 1 mg/ml PFA, (iii) 2 mg/ml PFA, and iv) 3 mg/ml PFA based perovskite films.

absorption peak significantly but an increase in concentration beyond 2 mg/ml reduced the absorption intensity marginally. The initial enhancement of absorption intensity can be correlated with the uniformity and higher crystallinity of passivated perovskite film which can substantially improve photon harvesting capability. To get better insight about the functional group interaction between the perovskite and PFA, Fourier transform infrared (FTIR) spectroscopy was analyzed (Figure 4.3b). Two sharp peaks for N-H stretching of primary amine group was visible at 3413 cm^{-1} and 3511 cm^{-1} for only PFA but when PFA was incorporated with perovskite layer, N-H stretching peak patterns were changed and shifted towards lower wavenumber at 3411 cm^{-1} and 3502 cm^{-1}. This indicates that there is an adequate interaction between the amine group and perovskite layer which can effectively suppress the defects on the surface of perovskite. To analyze about the influence of passivation in tuning grain orientation and overall morphology in thin film, field emission scanning electron microscope (FESEM) was employed for perovskite films which are passivated with varied concentration of PFA. FESEM images displayed that the morphology of pristine films has lack of uniformity in grain

distribution, size and compactness (Figure 4.3c). Contrarily, the passivated surfaces showed significant improvement in grain size and compactness with increase of PFA concentration up to 2 mg/ml which can contribute in diminishing the trap states in perovskite film.

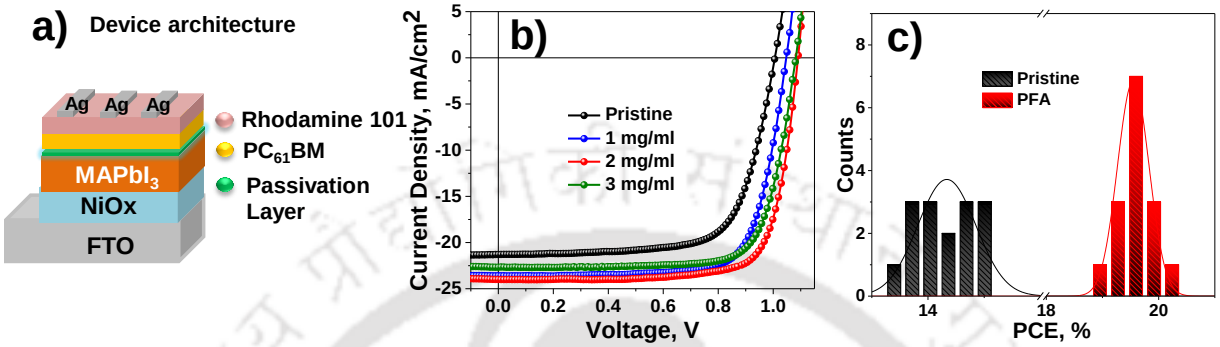

Figure 4.4: a) Schematic presentation of device architecture, b) *J–V* curves of the devices with various PFA concentrations, and c) Histogram of 15 cells of pristine and PFA modified device.

The multiple types of interactions between the PFA solution and perovskite top layer assisted the well-ordered growth of perovskite grains. However, beyond 2 mg/ml concentration, aggregated particles of PFA were visible on the surface which can adversely impact the movement of charge carriers due to the poor conductive property of the passivation additive. After the successive DFT, spectroscopic and morphological analysis of PFA based perovskite films; it was evident that PFA is a suitable additive for passivation with optimum concentration of 2 mg/ml which can significantly influence the photovoltaic property. Subsequently, we fabricated the photovoltaic devices using inverted architecture of FTO/NiOx/$MAPbI_3$/$PC_{61}BM$/Rhodamine 101/Silver (Figure 4.4a). Figure 4.4b displays the current density versus voltage (*J–V*) plot of pristine and passivated perovskite films with varied concentration of PFA. The summary of PVSC parameters is included in Table 4.1. The pristine devices achieved PCE of 15.08% efficiency with J_{SC} = 21.30 mA/cm^2, V_{OC} = 1.006 V, and FF = 70.4%. A gradual increase in concentration up to 2 mg/ml of PFA improved the device parameters which collectively enhanced the PCE up to 20.05% with *Jsc* = 23.99 mA/cm^2, V_{OC} = 1.09 V, and FF = 76.7%. However, as the concentration of PFA was raised above 2 mg/ml, the

efficiency decreased significantly due to the uncontrolled aggregation of PFA on perovskite surface which was evident in FESEM image also.

Table 4.1: Photovoltaic parameters for pristine and PFA passivated devices

Device	J_{SC}, mA/cm^2	*Voc*, V	FF, %	PCE (average)[a], %
Pristine	21.30	1.006	70.4	15.08 (14.33±0.52)
1 mg/ml PFA	23.38	1.045	73.5	17.97 (17.20±0.70)
2 mg/ml PFA	23.99	1.090	76.7	20.05 (19.45±0.38)
3 mg/ml PFA	22.50	1.081	76.1	18.50 (17.64±0.49)

[a] Average of 15 devices.

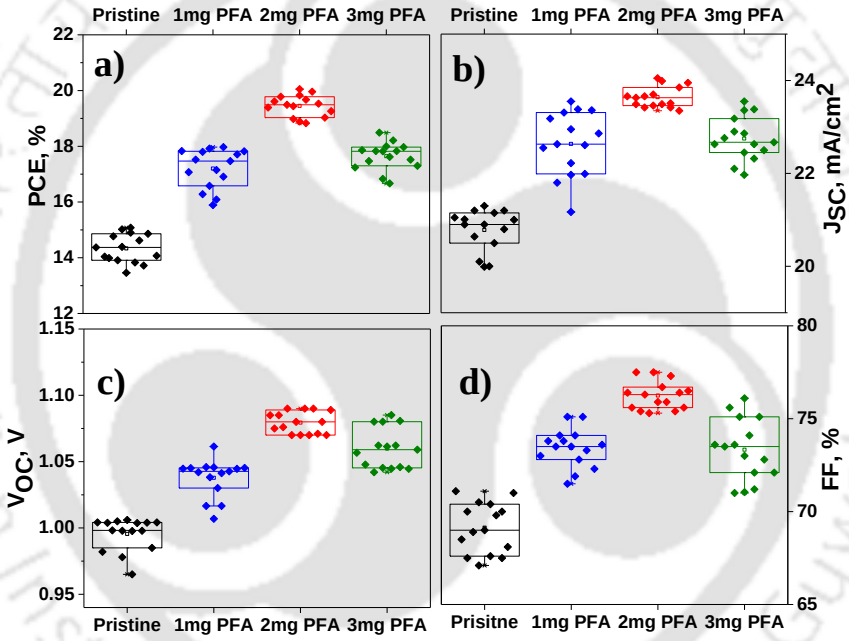

Figure 4.5: Box charts of different photovoltaic parameters for pristine and PFA passivated devices with varied concentration a) PCE, b) J_{SC}, c) V_{OC}, and d) FF.

Due to poor conductive nature of PFA, its overcrowding impacted the device parameters (J_{SC}, V_{OC}, and FF) adversely and reduced the efficiency of the devices. In Figure 4.4c, a histogram (of 15 devices) for PCE of PFA based devices is shown displaying improved efficacy with better reproducibility than the pristine devices. Subsequently, to present the concentration dependent reproducibility of photovoltaic parameters by PFA passivated devices, statistical data of 15 devices are displayed in Figure 4.5a-d as box chart. 2 mg/ml PFA based devices showed enhanced PCE with higher degree of reproducibility for all photovoltaic parameters, compared to the other devices.

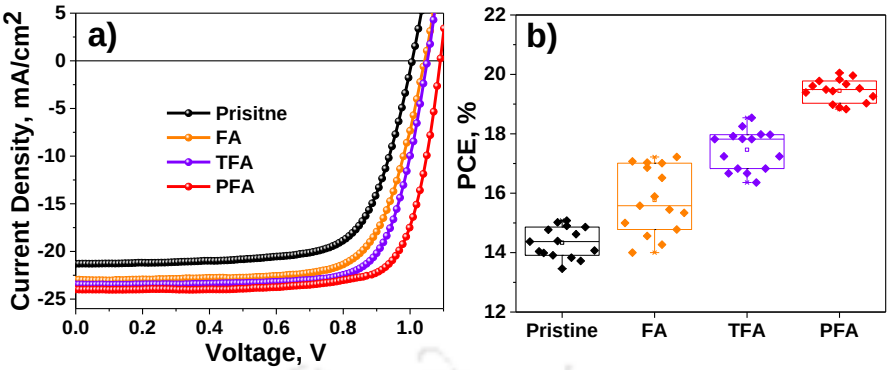

Figure 4.6: a) Current Density versus Voltage (*J-V*) plot for PVSCs passivated with different FAAs and b) Box chart of PCE for PVSCs passivated with different FAAs.

Table 4.2: Photovoltaic parameters for pristine and FAAs passivated PVSCs

Device	J_{SC}, mA/cm^2	*Voc*, V	FF, %	PCE (average)[a], %
Pristine	21.30	1.006	70.4	15.08 (14.33±0.52)
FA	22.98	1.043	71.8	17.22 (16.37±0.65)
TFA	23.46	1.051	75.1	18.54 (17.46±0.67)
PFA	23.99	1.090	76.7	20.05 (19.45±0.38)

[a] Average of 15 devices.

Higher reproducibility of PFA passivated devices indicates the impact of passivation, which successfully minimized the defects of perovskite lattice. A comparative analysis of device efficiency of FA, TFA, and PFA was also presented in *J–V* characteristic plot in Figure 4.6a where 2 mg/ml concentration was considered as the standard for all the additives. Photovoltaic data for different additives are summarized in Table 4.2. A box chart of PCE is also included for all additives presenting the reproducibility of device performance (Figure 4.6b). PFA displayed the highest efficiency, compared to other FAAs due to its superior capability to suppress the defects in perovskite. Figure 4.7a displays *J-V* curves for forward and reverse scan of PFA passivated and pristine device (corresponding data presented in Table 4.3). PFA passivated devices had almost identical *J-V* characteristic curves for scans in both direction exhibiting lower hysteresis, compared to the pristine one. The PFA passivated device exhibited very low HI of 0.89%, compared to 9.08% of pristine device.

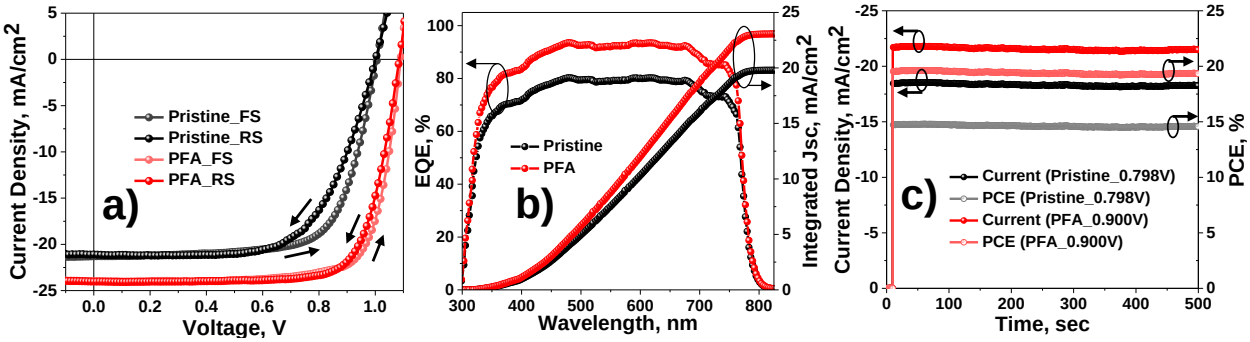

Figure 4.7: a) *J–V* curves of pristine and PFA passivated devices at forward and reverse scan, b) EQE curves of devices without and with PFA additive, and c) Steady-state current measured for pristine and PFA passivated PVSCs at maximum power point.

To estimate the magnitude of hysteresis, the hysteresis index (HI) was calculated using previously reported equation (4.1).[35]

$$\mathrm{HI} = \frac{|\mathrm{PCE}_{FS} - \mathrm{PCE}_{RS}|}{\mathrm{PCE}_{FS}} \times 100 \qquad (4.1)$$

Table 4.3: Device parameters for hysteresis study of pristine and PFA modified device

Device	J_{SC}, mA/cm^2	V_{OC}, V	FF, %	PCE, %	HI, %
Pristine_FS	21.30	1.006	70.4	15.08	9.08
Pristine_RS	21.01	1.001	65.2	13.71	
PFA_FS	23.99	1.090	76.7	20.05	0.89
PFA_RS	24.05	1.089	75.9	19.87	

This sharp improvement of hysteresis profile can be attributed to suppression of trap states through passivation which reduces the charge accumulation at the interface.[36] When external quantum efficiency (EQE) of passivated device was analyzed, passivated device exhibited better EQE than pristine one (Figure 4.7b). Integrated J_{SC} values were found to be well comparable to the values obtained using *J-V* analysis for both pristine and PFA based devices. To further validate *J-V* characteristic, steady-state current measurements were investigated at a maximum power point for PFA passivated and pristine device (Figure 4.7c). Both passivated and pristine devices demonstrated steady photo response

over 500 sec and PFA based devices exhibited higher PCE of 19.40%, compared to 14.72% of the pristine device.

To further analyze the mechanism of trap passivation, few opto-electronic studies were done for pristine and PFA based films. Firstly, absorption band edge of perovskite layer was used to estimate the Urbach energy (E_u). E_u can be associated with defects in band edge region and was determined using following equation (4.2),[37]

$$\alpha = \alpha_0 \exp(\frac{E}{E_u}) \qquad (4.2)$$

where, α is the absorption coefficient, α_0 presents a constant and E (= hυ) is the energy associated with photon. Figure 4.8a displays ln (α) versus photon energy plot wherefrom the slope of the graph, E_u was determined to be 53.7 meV for the pristine devices which reduces to 44.4 meV for passivated device.

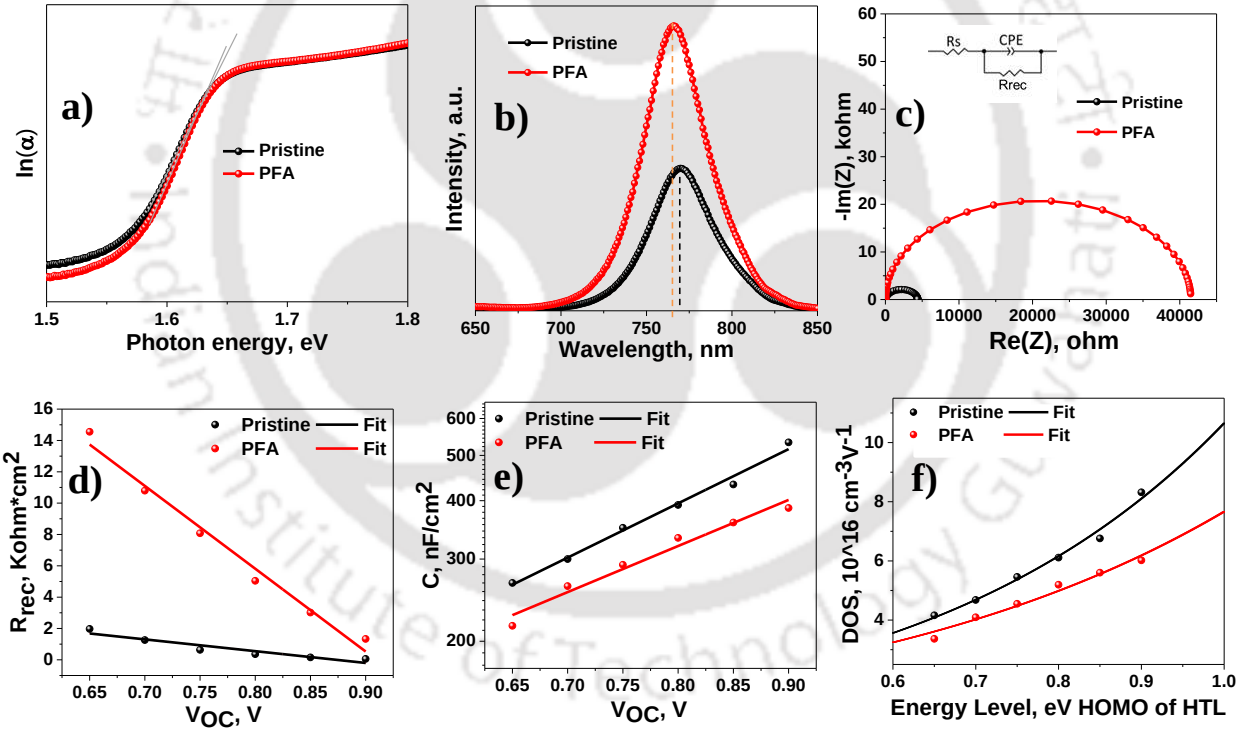

Figure 4.8: a) ln(α) versus photon energy plot, b) steady state PL spectra for pristine and PFA based films, c) Nyquist plots for pristine and PFA based devices with the fitting circuit in the inset, d) R_{rec} at different voltage bias, e) variation of C at different voltage bias, and f) trap density of states (DOS) versus electron energy level for pristine and PFA based devices.

This decrease in E_u for passivated devices indicates the mitigation of defect states and energetic disorder in band edge region of photoactive layer. Passivation significantly lowered the trap assisted recombination that resulted in elevation of V_{OC} of passivated devices. To further illustrate the trap passivation mechanism, steady state photoluminescence (PL) was studied for pristine and passivated film Figure 4.8b. The intensity of PL enhanced significantly for PFA based film, compared to the pristine film. The peak maximum at 766 nm for passivated film was blue shifted by 4 nm in comparison to the peak maxima of pristine film at 770 nm. This suggests that passivation resulted in substantial reduction in the trap states. In addition, the surface passivation of perovskite also minimized the non-radiative recombination in photoactive layer. The recombination properties and interfacial charge carrier kinetics of PVSCs can be analyzed by the electrochemical impedance spectroscopy (EIS). The Nyquist plots of the pristine and PFA based devices were estimated at a bias of 0.75 V under dark condition. The series resistance (R_S), recombination resistance (R_{rec}), and capacitance (C) can be determined for pristine and PFA based devices from the fitted graph (using equivalent circuit in inset) as shown in Figure 4.8c. The magnitude of R_S was reduced for passivated device, compared to the pristine device which signifies that PFA has considerably decreased the contact resistance at the interface. Also, R_{rec} was observed for PFA passivated devices to be higher than pristine device which signifies the lower rate of recombination, hence assisting the smooth charge carrier movement in the passivated device. Moreover, C signifies the extent of charge storage at the defects of perovskite layer. Lower value of C for passivated device, compared to pristine one revalidated the superior capability of PFA as an additive to suppress defects in perovskite film. EIS measurement was also conducted at different voltages (0.65-0.90 V). Linearly fitted curve of R_{rec} with varied applied voltage is presented in Figure 4.8d for pristine and PFA passivated devices which is displaying an inversely proportional relation between R_{rec} and applied voltage. R_{rec} of passivated device is significantly higher in comparison to the pristine device at all applied voltages which signifies that the effective passivation of traps reduced the charge carrier recombination substantially. Devices with lower charge recombination facilitates smooth transport of charge carriers and resulted in improved J_{SC} and V_{OC} for PFA passivated devices. Linear fitted semi log curve of capacitance, C with

varied voltages are also presented for both pristine and passivated device in Figure 4.8e. The magnitude of C is lesser for PFA passivated device than pristine device which signifies that PFA passivation mitigated the charge accumulation at traps. Further, the trap density of states (t-DOS) was assessed from C versus applied voltage graph and passivated device displayed significantly lower value of t-DOS than the pristine one which indicates about the lesser extent of charge carrier recombination in passivated devices (Figure 4.8f).[26] The impact of trap passivation in PFA based devices is very evident and the charge recombination reduced significantly which assisted smoother transport of charge carrier towards respective electrodes. To further investigate the impact of passivation in long term durability of PVSCs, we have exposed the PFA passivated and pristine devices to ambient condition with RH 45 ± 5%. For pristine devices a steep decline was observed across all photovoltaic parameters (J_{SC}, V_{OC}, and FF) which collectively reduced the PCE in ambient condition and after 1000 h of ambient exposure it was able to retain PCE of only 26% of its initial efficiency (Figure 4.9a).

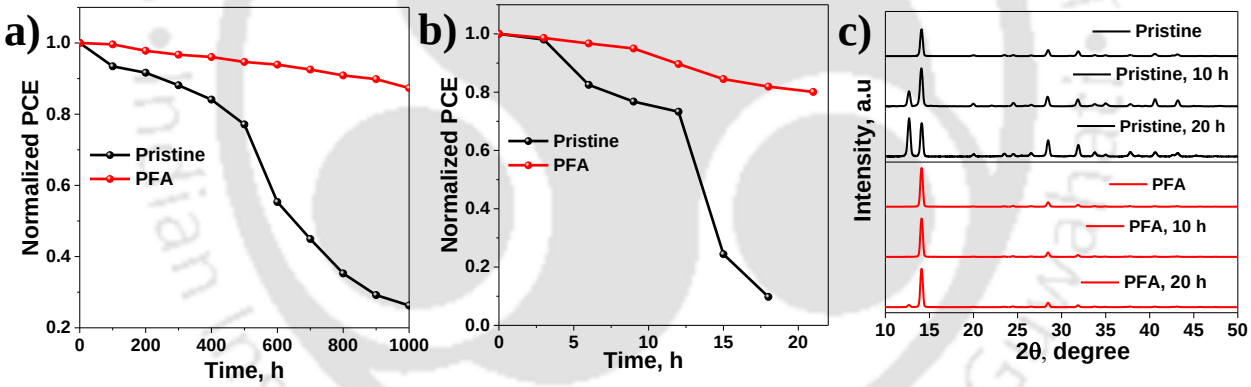

Figure 4.9: a) Normalized PCE of pristine and PFA based devices aged at room temperature in a relative humidity of 45 ± 5%, b) Normalized PCE of pristine and PFA based devices heated at 100 °C inside the glovebox, and c) XRD patterns of perovskite films heated at 100 °C for 20 h.

In contrast, the PFA passivated device showed high moisture resistivity and was able to maintain higher magnitude in all photovoltaic parameters which is reflected in overall retained PCE of 87%. The hydrophobic nature and passivation capability of PFA immensely contributed in achieving higher ambient stability. The decline of efficiency in the pristine devices can be correlated with gradual degradation of crystal structure under humid condition which was evident from the presence of PbI_2 phase in XRD data in Figure

4.1d after the exposure to moisture for 1000 h. Thermal instability of perovskite material is another major hurdle for PVSCs for their wider applicability. To further understand the impact of PFA passivation on perovskite layer, thermal stability test was executed at 100 °C inside the glove box for both pristine and PFA passivated devices. Figure 4.9b displays normalized PCE versus time plot for PVSCs where pristine device retained only 10% of its initial PCE after 18 h of heating at 100 °C. Contrarily, passivated device showed much improved heat stability and maintained 82% of its initial PCE even after 20 h of heating at 100 °C. Heat induced degradation of pristine and PFA passivated device can be further correlated with XRD data (Figure 4.9c) which implies that the rate of degradation is minimized substantially due to the incorporation of PFA on the perovskite surface and hence the growth rate of PbI_2 phase in passivated device is much lower. Moreover, it can be concluded that passivation by PFA has significantly improved the stability (moisture and thermal) and led the PCE to beyond 20% which can elevate its possibility for commercial applications.

4.3 Conclusion

In summary, we have demonstrated here that 2,3,4,5,6-pentafluoroaniline incorporation on perovskite layer tunes the photo-physical property, morphology and suppresses the defects in perovskite crystal lattice. For passivated device, PCE substantially improved up to 20.05% (J_{SC} = 23.99 mA/cm^2, V_{OC} = 1.090 V, and FF = 76.7%) in comparison to 15.08% of pristine device. Moreover, the ambient and thermal stability have been enhanced considerably by the introduction of hydrophobic PFA molecule. The passivated device displayed great ability to maintain its high efficiency for longer periods, compared to the pristine device. Moreover, the trap states were mitigated due to the PFA passivation which facilitates smooth charge transport in PVSCs. This unique approach can assist in developing highly efficient PVSCs with longer durability that can sustain in harsh environmental conditions.

4.4 Experimental Section

4.4.1 Materials

FTO glass substrates (13 Ω sq^{-1}), PbI_2 (99.8%), all anhydrous solvents such as DMF, DMSO, Isopropanol (IPA), Toluene, and Chlorobenzene, along with Rhodamine 101 inner salt were purchased from Sigma-Aldrich. Methylammonium iodide (MAI) was obtained from Dyesol.

Nickel nitrate hexahydrate ($Ni(NO_3)_2 \cdot 6H_2O$) was obtained from TCI. All other chemicals were utilized as received.

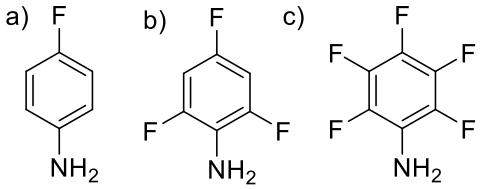

Figure 4.10: Chemical Structure of a) 4-fluoroaniline (FA), b) 2,4,6-trifluoroaniline (TFA), and c) 2,3,4,5,6-pentafluoroaniline (PFA).

4.4.2 NiO_x Film Preparation

NiO_x solution was prepared by dissolving Nickel nitrate hexahydrate and Ethylenediamine (in 1:1 molar ratio) in Ethylene glycol (1 ml). Then the NiO_x layer was coated as hole transporting layer (HTL) on the cleaned FTO. The cleaning process of FTOs was started with detergent and followed by deionized (DI) water, Acetone, and IPA for 15 min for each solvent, then dried and treated with UV-ozone for half an hour. NiO_x precursor solution was spin coated onto the FTO substrates at 3500 rpm for 45 sec. Lastly, the substrates were annealed at 300 °C for 60 min under ambient condition.

4.4.3 Device Fabrication

The $MAPbI_3$ precursor solution was prepared in a glovebox by mixing 209 mg of MAI, 581 mg of PbI_2 in a solvent mixture of γ-Butyrolactone and DMSO (7:3, v/v). The solution was heated for 5-6 h and filtered with the 0.45 μm filter prior to spin coating. The filtered precursor solution was spin coated on the NiO_x coated FTO in a two-step spin coating process that is 750 rpm for 20 sec and 4000 rpm for 60 sec. In the second step 150 μL anhydrous Toluene was dripped slowly after 20 sec as anti-solvent and after that the substrates were annealed at 80 °C for 10 min on a hotplate. For the passivated devices varied concentration of fluorinated aromatic amines (FAAs) solutions in IPA were coated above perovskite at 4000 rpm for 40 sec and dried at room temperature. After that for both passivated and pristine devices 12 mg/ml $PC_{61}BM$ solution was coated at 1200 rpm as electron transporting layer (ETL) and again annealed at 80 °C for 5 min on a hotplate. After that a thin layer of Rhodamine 101 inner salt was spin coated at 4000 rpm from

a solution of 0.5 mg/ml in IPA. Finally, Ag was thermally deposited by using a shadow mask to obtain the devices with active area of 0.12 cm^2.

4.4.4 Device Characterization

The XRD patterns of the perovskite films were studied using a Rigaku Micromax-007HF diffractometer equipped with Cu Kα1 irradiation (λ = 1.54184 Å). The perovskite films were analyzed by UV-vis absorption spectroscopy (Perkin Elmer Lambda-35) and FTIR spectroscopy (LabRam HR) in ATR mode. The film morphology of the samples was investigated by scanning electron microscopy (SEM, JEOL JSM-7610F). The current density−voltage (*J*−*V*) characteristic curves were recorded using a Keithley 2400 source meter under inert atmosphere by illuminating the device with a solar simulator (AM 1.5G, 100 mW/cm^2, Oriel Sol 3A solar simulator, Newport). The incident external quantum efficiency (EQE) was obtained by using an Oriel IQE-200 instrument under ambient condition. Electrochemical measurements were analyzed using a CH Instruments 760D.

4.5 References

(1) N. B. R. C. E. https://www.nrel.gov/pv/assets/pdfs/pv-efficiency-chart.20190103.pdf.

(2) J. Burschka, N. Pellet, S. J. Moon, R. Humphry-Baker, P. Gao, M. K. Nazeeruddin, M. Grätzel, *Nature*, 2013, **499**, 316-319.

(3) S. Sun, T. Salim, N. Mathews, M. Duchamp, C. Boothroyd, G. Xing, T. C. Sum, Y. M. Lam, *Energy Environ. Sci*., 2014, **7**, 399-407.

(4) T. Niu, J. Lu, R. Munir, J. Li, D. Barrit, X. Zhang, H. Hu, Z. Yang, A. Amassian, K. Zhao, S. Liu, *Adv. Mater*., 2018, **30**, 1706576.

(5) Y. C. Wang, J. Chang, L. Zhu, X. Li, C. Song, J. Fang, *Adv. Funct. Mater*., 2018, **28**, 1706317.

(6) Y. Rong, Y. Hu, A. Mei, H. Tan, M. I. Saidaminov, S. I. Seok, M. D. McGehee, E. H. Sargent, H. Han, *Science*, 2018, **361**, eaat8235.

(7) H. Cho, S. H. Jeong, M. H. Park, Y. H. Kim, C. Wolf, C. L. Lee, J. H. Heo, A. Sadhanala, N. Myoung, S. Yoo, S. H. Im, R. H. Friend, T. W. Lee, *Science*, 2015, **350**, 1222.

(8) A. Kojima, K. Teshima, Y. Shirai, T. Miyasaka, *J. Am. Chem. Soc.* 2009, **131**, 6050-6051.

(9) Z. Wang, C. Dong, X. Wang, M. Li, T. Nan, X. Liang, H. Chen, Y. Wei, H. Zhou, M. Zaeimbashi, S. Cash, N. X. Sun, *NPJ Flexible Electronics*. 2018, **2**, 17.

(10) C. Besleaga, L. E. Abramiuc, V. Stancu, A. G. Tomulescu, M. Sima, L. Trinca, N. Plugaru, L. Pintilie, G. A. Nemnes, M. Iliescu, H. G. Svavarsson, A. Manolescu, I. Pintilie, *J. Phys. Chem. Lett.*, 2016, **7**, 5168-5175.

(11) M. Bag, L. A. Renna, R. Y. Adhikari, S. Karak, F. Liu, P. M. Lahti, T. P. Russell, M. T. Tuominen, D. Venkataraman, *J. Am. Chem. Soc*., 2015, **137**, 13130-13137.

(12) J. Prakash, A. Singh, G. Sathiyan, R. Ranjan, A. Singh, A. Garg, R. K. Gupta, *Mater. Today Energy*, 2018, **9**, 440-486.

(13) S. Emami, J. Martins, D. Ivanou, A. Mendes, *J. Mater. Chem. A*, 2020, **8**, 2654-2662.

(14) H. C. Weerasinghe, Y. Dkhissi, A. D. Scully, R. A. Caruso, Y. B. Cheng, *Nano Energy*, 2015, **18**, 118-125.

(15) R. Ranjan, A. Prakash, A. Singh, A. Singh, A. Garg, R. K. Gupta, *J. Mater. Chem. A*, 2018, **6**, 1037-1047.

(16) G. Sathiyan, R. Ranjan, S. Ranjan, A. Garg, R. K. Gupta, A. Singh, *ACS Appl. Energy Mater.*, 2019, **2**, 7609-7618.

(17) R. K. Gupta, R. Garai, M. Hossain, A. Choudhury and P. K. Iyer, *ACS Sustainable Chem. Eng*, 2021, **9**, 7993-8001.

(18) X. Bao, J. Wang, Y. Li, D. Zhu, Y. Wu, P. Guo, X. Wang, Y. Zhang, J. Wang, H. L. Yip and R. Yang, *Adv. Mater. Interfaces*, 2017, **4**, 1600948.

(19) P. Zhao, B. J. Kim, H. S. Jung, *Mater. Today Energy* 2018, **7**, 267-286.

(20) C. Gao, H. Dong, X. Bao, Y. Zhang, A. Saparbaev, L. Yu, S. Wen, R. Yang and L. Dong, *J. Mater. Chem. C*, 2018, **6**, 8234-8241.

(21) S. Wang, A. Wang, X. Deng, L. Xie, A. Xiao, C. Li, Y. Xiang, T. Li, L. Ding, F. Hao, *J. Mater. Chem. A*, 2020, **8**, 12201-12225.

(22) L. Su, Y. Xiao, L. Lu, G. Han, M. Zhu, *Org. Electron.*, 2020, **77**, 105519.

(23) N. D. Pham, V. T. Tiong, P. Chen, L. Wang, G. J. Wilson, J. Bell, H. Wang, *J. Mater. Chem. A*, 2017, **5**, 5195-5203.

(24) L. Zhu, Y. Xu, P. Zhang, J. Shi, Y. Zhao, H. Zhang, J. Wu, Y. Luo, D. Li, Q. Meng, *J. Mater. Chem. A*, 2017, **5**, 20874-20881.

(25) M. A. Afroz, R. K. Gupta, R. Garai, M. Hossain, S. P. Tripathi, P. K. Iyer, *Org. Electron.*, 2019, **74**, 172-178.

(26) R. Garai, M. A. Afroz, R. K. Gupta, P. K. Iyer, *Adv. Sustainable Syst.*, 2020, **4**, 2000078.

(27) F. Wang, W. Geng, Y. Zhou, H. H. Fang, C. J. Tong, M. A. Loi, L. M. Liu, N. Zhao, *Adv. Mater.*, 2016, **28**, 9986-9992.

(28) W. Feng, C. Zhang, J. X. Zhong, L. Ding, W. Q. Wu, *Chem. Commun.*, 2020, **56**, 5006-5009.

(29) J. Xia, C. Liang, S. Mei, H. Gu, B. He, Z. Zhang, T. Liu, K. Wang, S. Wang, S. Chen, Y. Cai, G. Xing, *J. Mater. Chem. A*, 2021, **9**, 2919-2927.

(30) S. Zhao, J. Xie, G. Cheng, Y. Xiang, H. Zhu, W. Guo, H. Wang, M. Qin, X. Lu, J. Qu, J. Wang, J. Xu, K. Yan, *Small*, 2018, **14**, 1803350.

(31) J. Yang, C. Liu, C. Cai, X. Hu, Z. Huang, X. Duan, X. Meng, Z. Yuan, L. Tan, Y. Chen, *Adv. Energy Mater.*, 2019, **9**, 1900198.

(32) N. A. N. Ouedraogo, H. Yan, C. B. Han, Y. Zhang, *Small*, 2021, **17**, 2004081.

(33) M. Hossain, M. A. Afroz, R. Garai and P. K. Iyer, *Sustainable Energy Fuels*, 2021, **5**, 874-879.

(34) X. Wu, L. Zhang, Z. Xu, S. Olthof, X. Ren, Y. Liu, D. Yang, F. Gao, S. Liu, *J. Mater. Chem. A*, 2020, **8**, 8313-8322.

(35) R. Azmi, N. Nurrosyid, S. H. Lee, M. Al Mubarok, W. Lee, S. Hwang, W. Yin, T. K. Ahn, T. W. Kim, D. Y. Ryu, Y. R. Do, S. Y. Jang, *ACS Energy Lett*., 2020, **5**, 1396-1403.

(36) J. Cao, B. Wu, R. Chen, Y. Wu, Y. Hui, B. W. Mao, N. Zheng, *Adv. Mater*,. 2018, **30**, 1705596.

(37) Y. Zhang, P. Wang, X. Yu, J. Xie, X. Sun, H. Wang, J. Huang, L. Xu, C. Cui, M. Lei, D. Yang, *J. Mater. Chem. A*, 2016, **4**, 18509-18515.

Chapter 5

Enhancing Efficiency and Ambient Stability of Perovskite Solar Cells via Multifunctional Trap Passivation Molecule

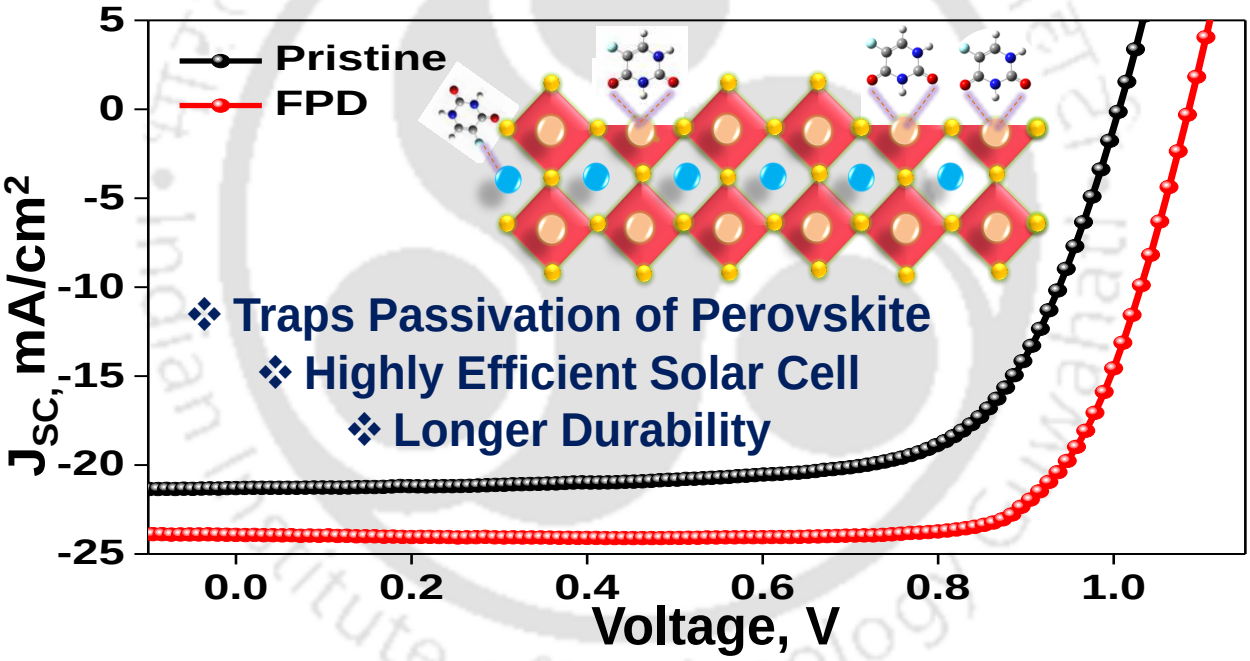

M. Hossain, R. Narasimhan, R. Garai, R. K. Gupta, and P. K. Iyer, *J. Mater. Chem. C*, 2021, **9,** 14309-14317.

Abstract

In recent times the perovskite solar cells (PVSCs) have emerged as the most preeminent candidates among renewable technologies, yet the instability of PVSCs in ambient condition has hindered its progress towards commercialization. Herein, a multifunctional passivation additive, 5-fluoropyrimidine-2,4(1H,3H)-dione (FPD), widely used as a cancer drug, was incorporated in perovskite based photoactive layer to enhance its photovoltaic efficiency along with its ambient stability. When this biologically active cancer drug molecule was utilized as a passivation additive, significant improvement was achieved in all photovoltaic parameters that collectively contributed in the enhancement of photovoltaic efficiency. The efficiency of PVSCs was elevated up to 20.22% for FPD passivated devices from 15.10% for pristine device without any passivation. Furthermore, the incorporation of FPD also improved the long term durability of PVSCs by suppressing defects and enhancing the hydrophobicity of perovskite surface. The FPD passivated device maintained PCE up to 89% in comparison to 27% for pristine devices when PVSCs were exposed to relative humidity 45 ± 5% for 1000 h. This unique approach has elucidated the impact of passivation which significantly enhanced the efficiency and long term stability to widen the possibility of practical applications.

5.1 Introduction

Hybrid perovskite solar cells (PVSCs) have demonstrated immense potentials as a preferable renewable technology for the forthcoming generation due to its incredible optoelectronic properties e.g. wide absorption with high absorptivity, bandgap tunability, higher carrier mobility, and longer charge carrier diffusion etc.[1-4] The extensive research on PVSCs in last decade has levitated the power conversion efficiency (PCEs) from 3% to 25% for single junction PVSCs at laboratory scale which is comparable with standard c-Si based photovoltaic technology.[5] However, among different perovskite materials, polycrystalline methylammonium lead iodide ($MAPbI_3$) films often possess electronic and grain boundary (GB) defects which can substantially reduce the PVSCs performance. These defects usually originate from the presence of under coordinated ions (MA^+, Pb^{2+}, and I^-) in perovskite thin film.[6] Moreover, these varied kinds of defects at the GB and surface of perovskite film stimulate rapid moisture penetration and ion migration in perovskite layer, instigating the faster deterioration of perovskite lattice structure resulting in ambient instability of PVSCs.

Hence, it is really essential to proficiently mitigate the defects and improve the quality of the thin films with better surface coverage, uniform grain distribution, and suitable stoichiometry.[7-8] To diminish the diverse kind of defects at the surface and GB of perovskite film, various techniques were implemented in PVSCs like molecular passivation,[9-11] device engineering,[12] compositional tuning,[13-16] etc. Among these techniques, molecular passivation of perovskite film has emerged as the most explored method in recent times. Molecular passivation induces various interactions with uncoordinated species in perovskite film which can significantly annihilate the defects in perovskite lattice.[17,18] The fluorine containing passivation additives were also utilized which can enhance the hydrophobicity of perovskite surface along with suppressing the defects in perovskite film.[19,20] The fluorine atom can decrease the ion migrations in perovskite layer by hydrogen bond formation with MA^+ ion which can reduce the structural instability in photoactive layer.[21-23] Although, varied methods were utilized to minimize the defects in PVSCs, it is always vital to utilize a suitable additive with multifunctional groups which can efficaciously diminish the diverse defects in perovskite photoactive layer. In recent times, our group has extensively explored the application of multifunctional additives to elevate the efficiency and long term durability of PVSCs by modulating perovskite crystallization process and enhancing hydrophobicity of perovskite photoactive layer.[9,10,24,25]

Herein, a multifunctional additive, 5-fluoropyrimidine-2,4(1H,3H)-dione (FPD) is utilized to suppress the broad range of defects and modulate the microstructures of perovskite film. FPD is a popular bioactive material (also known as 5-Flurouracil) due to its application as a cancer drug.[26] The immense therapeutic value of FPD stimulated extensive research globally.[27] This fluorinated additive contains two carbonyl groups and two amine groups in its aromatic structure which can interact with lead-iodide (Pb-I) framework to significantly suppress the defects in perovskite layer. Subsequently, FPD passivated inverted PVSCs achieved the enhanced short circuit current (J_{SC}), open circuit voltage (V_{OC}), and fill factor (FF) collectively contributing in the PCE above 20%, which is substantially higher than the pristine device (15.10%). The presence of fluorine atom also contributed in enhancing the hydrophobicity of perovskite thin film which significantly restricted the moisture penetration in perovskite layer under ambient condition. The defect suppression and enhancement of hydrophobicity in passivated perovskite film incredibly improved the ambient stability of the PVSCs. When the devices were exposed to relative humidity of 45 ± 5% for 1000 h, the passivated device retained efficiency up to 89% of

its initial PCE, compared to 27% of non-passivated device. This can be attributed to the efficient passivation by multifunctional FPD to suppress defects and enhance the hydrophobicity of perovskite surface.

5.2 Results and discussion

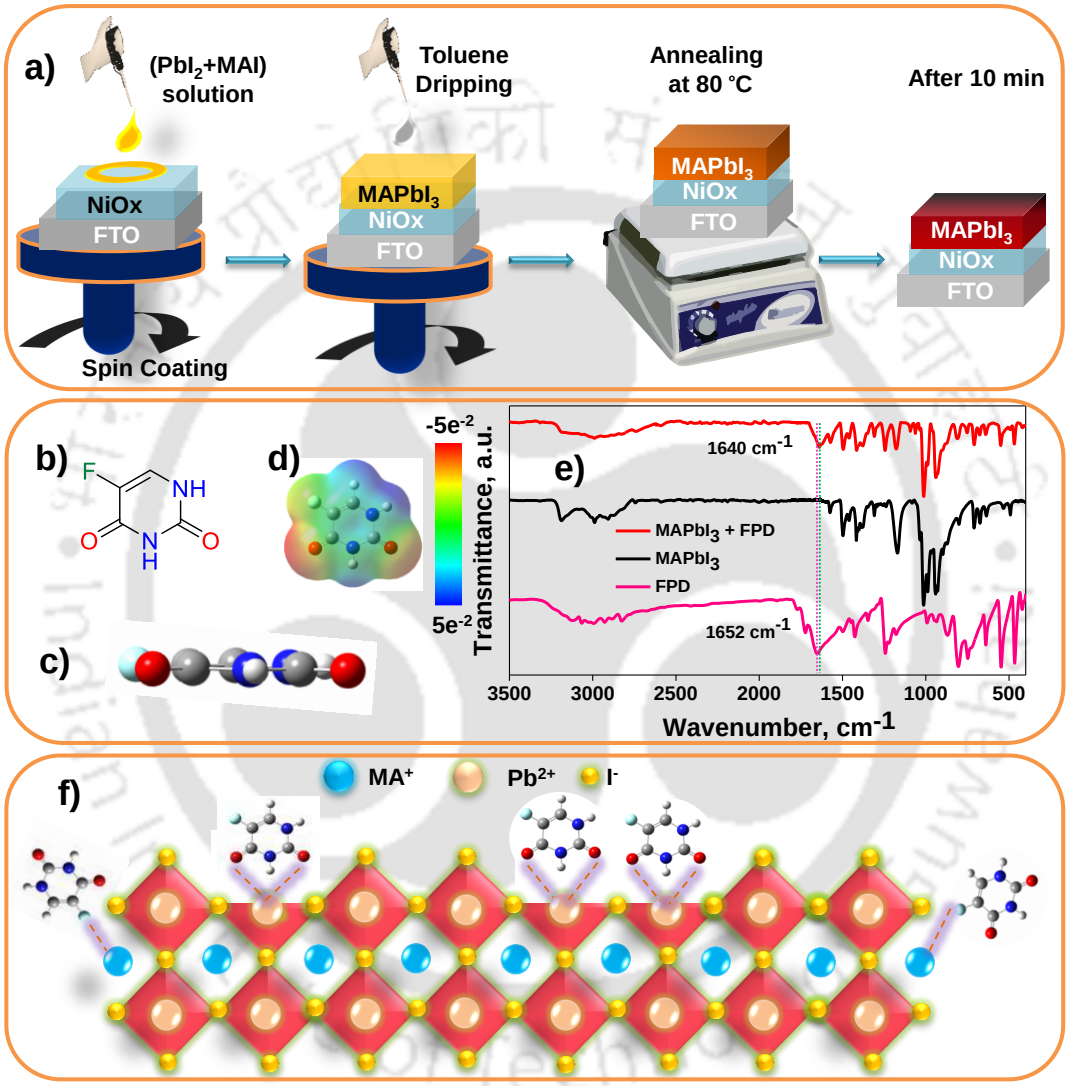

Figure 5.1: a) Schematic representation of perovskite thin film coating method, b) molecular structure of FPD, c) side view of optimized structure of FPD, d) ESP profile of FPD, e) FTIR spectra of FPD, $MAPbI_3$, and $MAPbI_3$ + FPD, and f) Schematic representation of plausible interactions between FPD with perovskite crystal lattices.

In Figure 5.1a, the fabrications steps for perovskite films are depicted. To analyze the impact of molecular passivation, varied concentrations of FPD were incorporated in precursor solution (PbI_2+MAI) to understand the combined effect of multifunctional nature of this additive on PVSCs. The precursor solution were deposited on NiOx coated FTO substrate by well explored anti-solvent dripping method. The details of fabrication method are illustrated in experimental section (5.4). The density functional theory (DFT) was utilized to gain insight about the electronic charge distribution and structural features of FPD molecule. The molecular structure, side view of optimized structure and electrostatic potential (ESP) of FPD are presented as Figure 5.1b, Figure 5.1c, and Figure 5.1d, respectively. In ESP profile of planar FPD, the carbonyl groups appeared as the most electron rich functional group which made it suitable to strongly interact with Pb^{2+} ions. Fluorine atom and amine moieties can also involve in varied non-covalent interactions with under coordinated ions in perovskite layer.

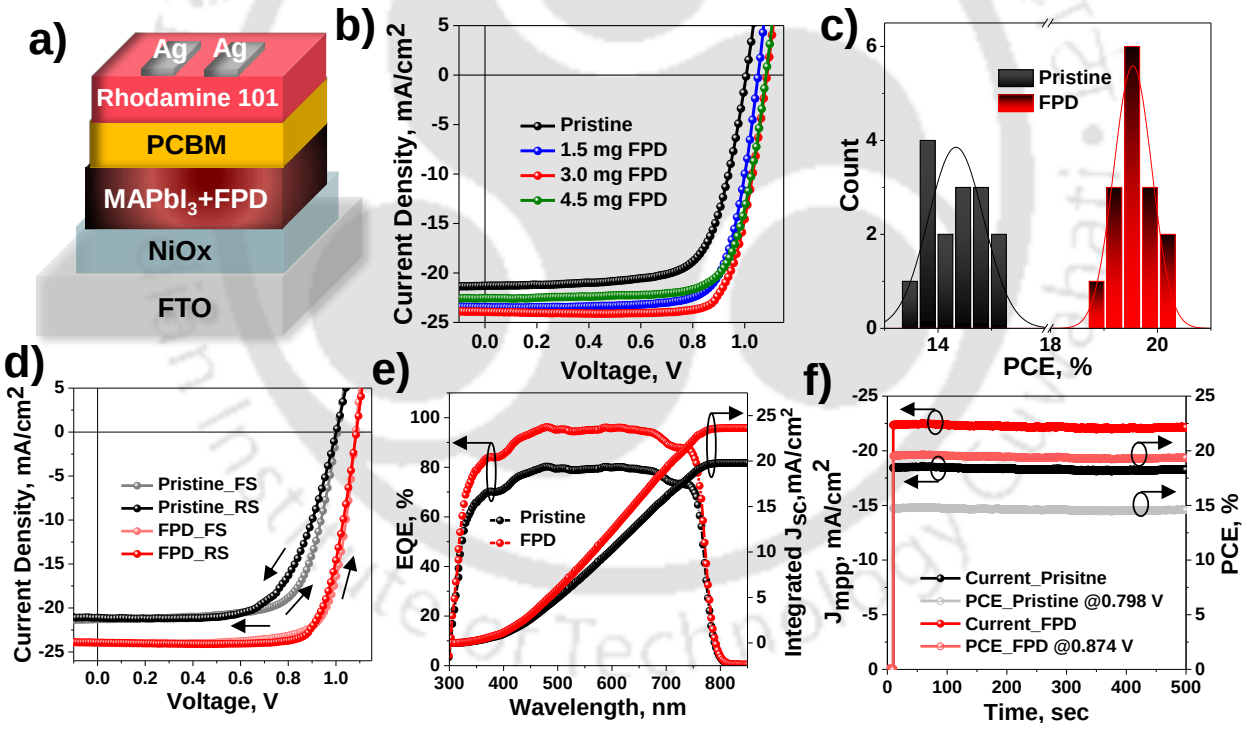

Figure 5.2: a) Schematic presentation of inverted device architecture, b) *J–V* profile of the PVSCs, c) Histogram of 15 cells of pristine and FPD passivated device, d) *J–V* profile at forward and reverse scan, e) EQE curves, and f) Steady state current study at maximum power point for pristine and FPD passivated PVSCs.

To confirm the interactions between FPD and perovskite, Fourier transform infrared spectroscopy (FTIR) was executed (Figure 5.1e). A considerable shift in $\upsilon_{C=O}$ band of FPD was observed from 1652 cm^{-1} (for only FPD) to 1640 cm^{-1} (for FPD+$MAPbI_3$) due to the strong interaction between the lone pairs of carboxylic acid groups of FPD and Pb^{2+} ions of perovskite crystal. A schematic of plausible interactions between FPD with perovskite crystal lattice is also presented in Figure 5.1f. The device architecture of PVSCs is displayed in Figure 5.2a. Consequently, PVSCs were fabricated utilizing the inverted architecture of FTO/NiOx/$MAPbI_3$/$PC_{61}BM$/Rhodamine 101/Silver. Figure 5.2b displays the current density versus voltage (*J–V*) plot of pristine and passivated PVSCs with varied concentration of FPD. The photovoltaic parameters for PVSCs are summarized in Table 5.1. The PCE of 15.10% was achieved for the pristine device with J_{SC} = 21.32 mA/cm^2, V_{OC} = 1.006 V, and FF= 70.4%.

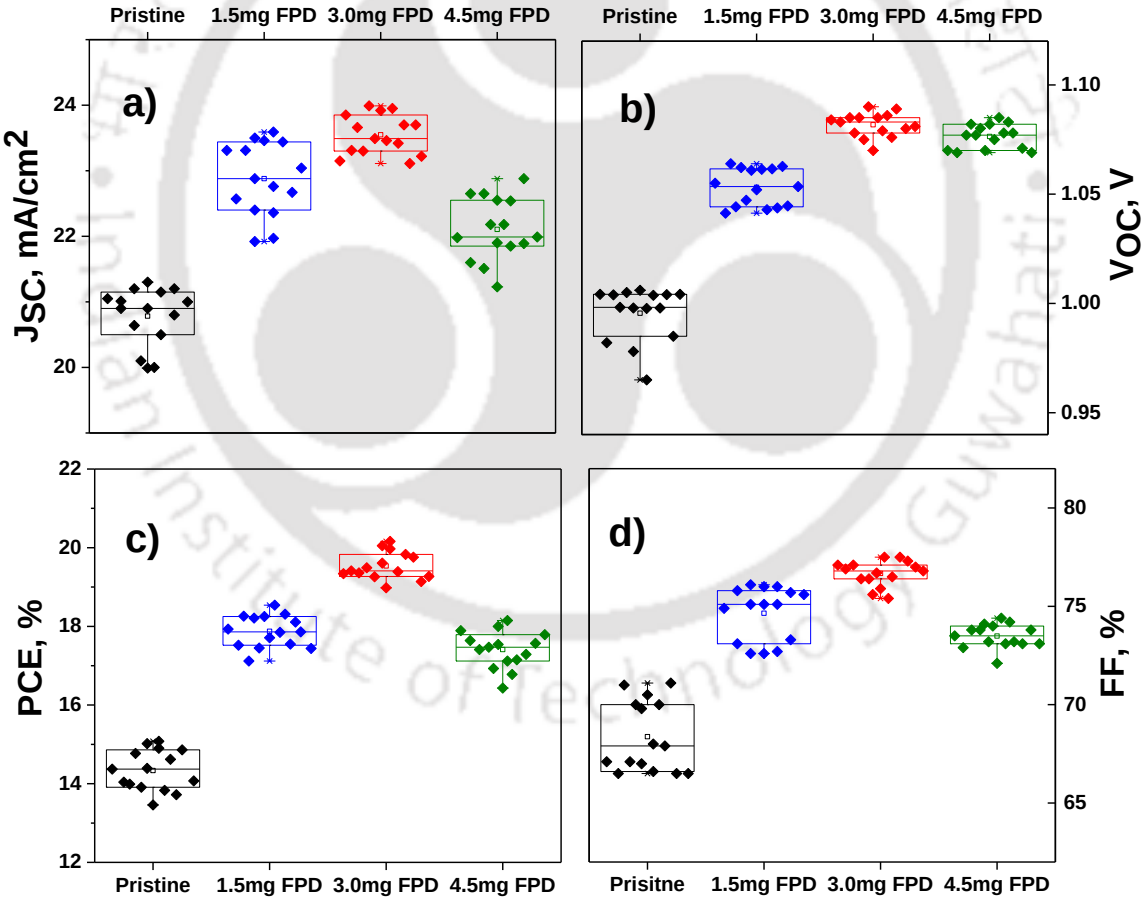

Figure 5.3: Box chart of a) J_{SC}, b) V_{OC}, c) PCE, and d) FF for pristine and FPD passivated device with varied concentrations.

Table 5.1: Photovoltaic parameters for pristine and FPD passivated devices

Device	J_{SC}, mA/cm^2	*Voc*, V	FF, %	PCE (average)[a], %
Pristine	21.32	1.006	70.4	15.10 (14.34±0.54)
1.5 mg/ml FPD	23.46	1.052	75.1	18.54 (18.01±0.40)
3.0 mg/ml FPD	23.97	1.086	77.7	20.22 (19.51±0.34)
4.5 mg/ml FPD	22.55	1.082	74.4	18.15 (17.69±0.47)

[a] Average of 15 devices.

As the concentration of FPD was increased gradually up to 3 mg/ml, the photovoltaic parameters was improved and collectively levitated the PCE up to 20.22% with *Jsc* of 23.97 mA/cm^2, V_{OC} of 1.086 V and FF of 77.7%. However, for FPD concentration above 3 mg/ml, the *Jsc* and FF decreased significantly resulting in overall inferior photovoltaic performance which can be attributed to the uncontrolled aggregation and poor conductive nature of additive within photoactive layer. In Figure 5.2c, a histogram is displayed which presents the reproducibility and enhancement in performance of passivated device, compared to the pristine counterpart. For the better understanding of FPD concentration depended reproducibility of the photovoltaic parameters, a box chart is included as Figure 5.3 which indicates about the relatively better reproducibility of photovoltaic parameters for 3 mg/ml FPD based PVSCs. Figure 5.2d presents *J-V* curves for forward and reverse scan of FPD passivated and pristine device and corresponding photovoltaic data is summarized in Table 5.2. To evaluate the extent of hysteresis in PVSCs, hysteresis index (HI) was assessed utilizing previously reported equation (5.1).[28,29]

$$\mathrm{HI} = \frac{|\mathrm{PCE}_{FS} - \mathrm{PCE}_{RS}|}{\mathrm{PCE}_{FS}} \times 100 \qquad (5.1)$$

Table 5.2: Device parameters for hysteresis study for pristine and FDP modified device

Device	**$J_{SC,}$ mA/cm^2**	**V_{OC}, V**	**FF, %**	**PCE, %**	**HI, %**
Pristine_FS	21.32	1.006	70.4	15.10	9.07
Pristine_RS	21.03	1.001	65.2	13.73	
FPD_FS	23.97	1.086	77.7	20.22	1.38
FPD_RS	24.01	1.083	76.7	19.94	

FPD passivated device had very similar *J-V* characteristic curves for both forward and reverse scan exhibiting lower hysteresis, compared to the non-passivated device. The FPD passivated device displayed lower HI of 1.38% in comparison to 9.07% of pristine device. This substantial improvement in hysteresis index can be attributed to the reduction of traps states through passivation which diminished the charge carrier accumulation at the interface.[30] Furthermore, the external quantum efficiency (EQE) of FPD passivated and pristine device was assessed and the FPD passivated device displayed the enhanced EQE, compared to the pristine counterpart (Figure 5.2e). The integrated J_{SC} values were calculated from EQE profile, which were found to be well-matched with the values presented in *J-V* analysis for both passivated and pristine device. To further evaluate the photo-responsive nature of FPD passivated PVSCs, steady-state current measurements were analyzed at maximum power point (Figure 5.2f). Both FPD passivated and pristine PVSCs demonstrated steady photo response over 500 sec. The passivated device displayed an enhanced PCE of 19.65%, compared to 14.72% of pristine device. To further analyze the impact of passivation on absorption profile, UV-vis absorption spectra were recorded for perovskite thin films which were passivated by varied concentrations of FPD (Figure 5.4a). As the FPD concentration was increased gradually, the intensity of absorption spectra of perovskite film was enhanced. However, as the FPD concentration reached beyond 3 mg/ml, a marginal decrease in absorption intensity was observed. The initial enhancement of absorption intensity after optimal FPD incorporation can be correlated with the improved quality of perovskite films where all films had comparable film thickness. It is also evident from *J-V* profile of passivated PVSCs that the enhancement of absorption intensity assisted in efficient photon harvesting. To elucidate the passivation effect on the crystalline nature of perovskite film, X-ray diffraction (XRD) was analyzed for thin films which were passivated with varied concentrations of FPD (Figure 5.4b). All perovskite films displayed polycrystalline nature with peaks at 14.11°, 28.47°, and 31.84° for (110), (220), and (310) perovskite planes, respectively. The peaks intensity for (110), (220), and (310) perovskite planes increased for FPD passivated films but as the concentration reached beyond 3 mg/ml, a slight decline was observed in peak intensity. To get a better insight of passivation effect on surface morphology, field emission scanning electron microscope (FESEM) was employed (Figure 5.4c). As the additive concentration was increased, the grain size and uniformity in grain distribution were improved

gradually. This morphological modulation by FPD can be attributed to the perovskite-additive interaction during crystallization process.

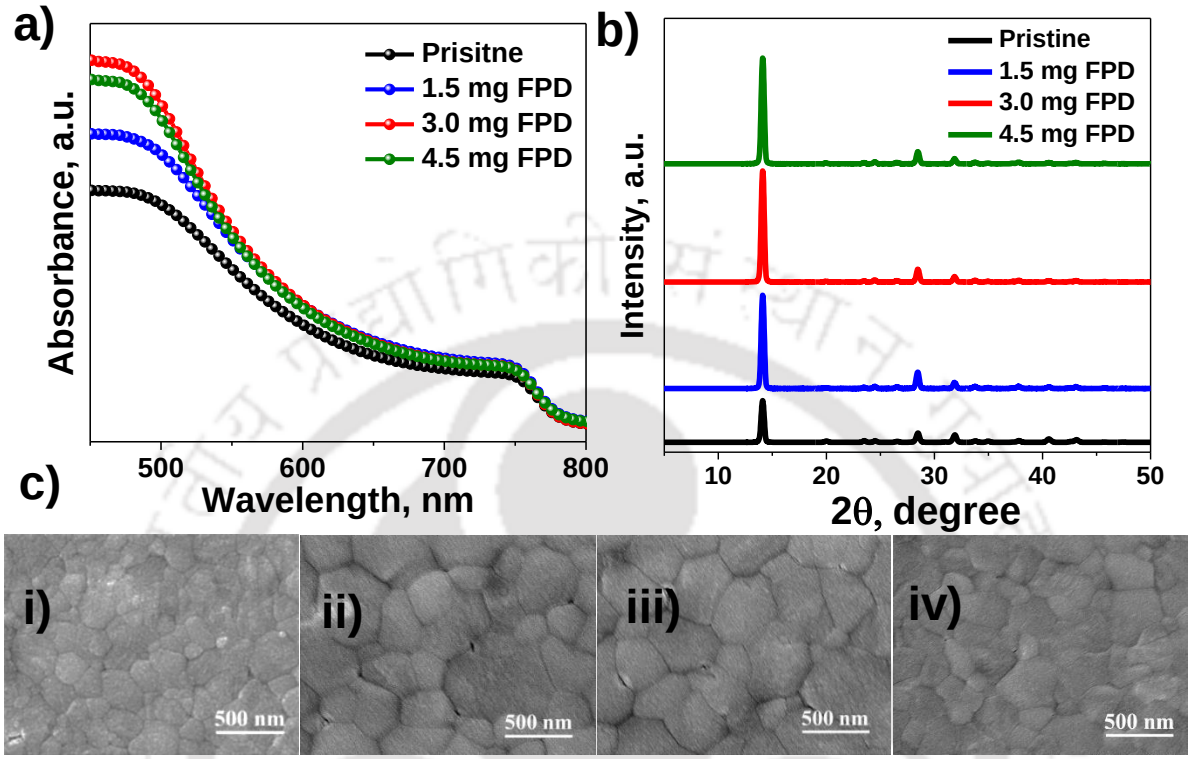

Figure 5.4: a) UV–vis absorption spectra of pristine and FPD passivated films, b) XRD patterns for perovskite thin films passivated with varied FPD concentration, and c) FESEM images of i) Pristine, ii) 1.5 mg/ml FPD, (iii) 3.0 mg/ml FPD, and iv) 4.5 mg/ml FPD based perovskite films.

However, as the FPD concentration reached beyond 3 mg/ml, the grain size and uniformity was reduced. This morphological change for higher additive concentration can be attributed to the uncontrolled overcrowding of FPD which interfered in perovskite crystal growth. The morphological dependence on FPD concentration can be correlated with the trend of photovoltaic performance of PVSCs where a sharp decline in efficiency was recorded for the device with higher additive concentration (> 3 mg/ml). Consequently, to analyze the trap passivation mechanism, few experimental studies were carried out for pristine and FPD passivated device. Initially, Urbach energy (E_u) was estimated from the band edge of perovskite absorbance profile for thin films. E_u is correlated with the defect density in the band edge region which can be measured by utilizing the well explored equation (5.2),[31,32]

$$\alpha = \alpha_0 \exp(\frac{E}{E_u}) \qquad (5.2)$$

where, α presents the absorption coefficient, α_0 is a constant and E (= hυ) is the photonic energy. Figure 5.5a depicts the ln (α) versus photon energy profile. E_u was calculated to be 52.8 meV for the pristine film utilizing the slope of the plot, which significantly reduced to 45.1 meV after passivation. The decline of E_u indicates that the FPD incorporation in perovskite significantly diminished the defect density and energetic disorders in band edge region. To further elucidate the trap passivation mechanism, steady state photoluminescence (PL) was also investigated for pristine and FPD based perovskite film (Figure. 5.5b). The intensity of PL was elevated substantially for FPD based film, compared to the pristine film.

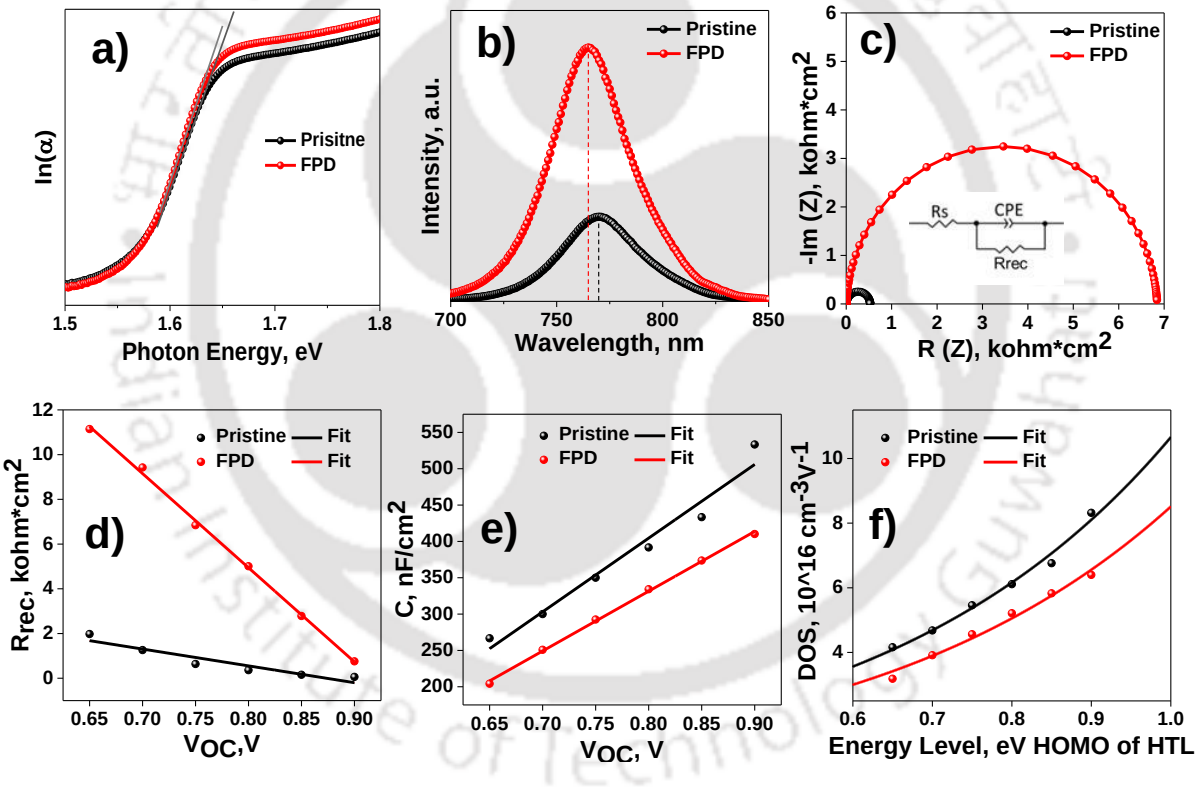

Figure 5.5: a) ln(α) versus photonic energy graph, b) Steady state PL profile for passivated and non-passivated films, c) Nyquist plots for pristine and FPD based PVSCs with fitting circuit in the inset, d) R_{rec} at varied voltage bias, e) Variation of C at varied voltage bias, and f) t-DOS versus electron energy level for pristine and FPD passivated PVSCs.

The peak maximum at 765 nm for FPD modified perovskite film was blue shifted by 5 nm, compared to the peak maxima of pristine film at 770 nm. This suggests that the passivation resulted in substantial reduction of trap density which also minimized the non-radiative recombination in photoactive layer.[10] The electrochemical impedance spectroscopy (EIS) was also analyzed for better understanding of interfacial charge carrier kinetics and recombination properties of PVSCs. The Nyquist plots of the pristine and FPD passivated devices were investigated at a bias of 0.75 V under dark condition (Figure. 5.5c). Varied parameters like series resistance (R_S), recombination resistance (R_{rec}), and capacitance (C) was determined for passivated and pristine devices from the fitted graphs utilizing equivalent circuit presented in inset. The estimated value of R_S was reduced for FPD passivated device, compared to the pristine counterpart. It indicates that the FPD incorporation in perovskite layer significantly lowered the contact resistance at the interface. Moreover, the magnitude of R_{rec} was found to be higher for FPD passivated device in comparison to the pristine one. That can be correlated with lesser extent of recombination in FPD based device which facilitated smooth charge movement in PVSCs. The magnitude of C implies the amount of charge storage at the defects of perovskite photoactive layer. The estimated lower value of C for passivated based device, compared to pristine counterpart validated the effective passivation capability of FPD to diminish the varied kinds of defects in perovskite layer. EIS measurement was also carried out at varied voltages to attain better understanding about the extent of trap passivation R_{rec} at varied voltages (0.65-0.90 V) for passivated and pristine devices were linearly fitted which depicts an inverse relation between R_{rec} and applied voltage. R_{rec} of passivated device is considerably higher, compared to pristine one at different applied voltages (Figure. 5.5d). This indicates about the efficacious passivation of traps which significantly reduced the charge carrier recombination. The lower charge carrier recombination resulted in enhanced photovoltaic parameters (J_{SC} and V_{OC}) in passivated PVSCs. Linear fitted semi log curve of capacitance at varied voltages were also displayed for both pristine and FPD based devices (Figure 5.5e). For passivated PVSCs, C was found to be lower compared to the pristine one which signifies that the passivation effectively mitigated the charge carrier accumulation at the traps. The trap density of states (t-DOS) was also analyzed from C versus applied voltage plot and FPD based device depicted substantially lower magnitude of t-DOS than pristine one which suggests about the lesser amount of charge carrier recombination in Passivated PVSCs (Figure 5.5f).[10] To further elucidate the

recombination mechanism of charge carriers, dark J–V was measured for the pristine and FPD based PVSCs which revealed that the reverse saturation current in the pristine PVSC was reduced after FPD incorporation (Figure 5.6a). This indicates about the lesser extent of recombination and smoother transport of charge carriers. Figure 5.6b displays the photocurrent density (J_{ph}) versus effective voltage (V_{eff}) profile for pristine and FPD passivated device, where $J_{ph} = J_{light} - J_{dark}$ and J_{light} and J_{dark} presents the current densities under light and dark condition respectively. $V_{eff} = V_0 - V$, where V and V_0 present the applied bias and the bias at which $J_{ph} = 0$ respectively.[33-35]

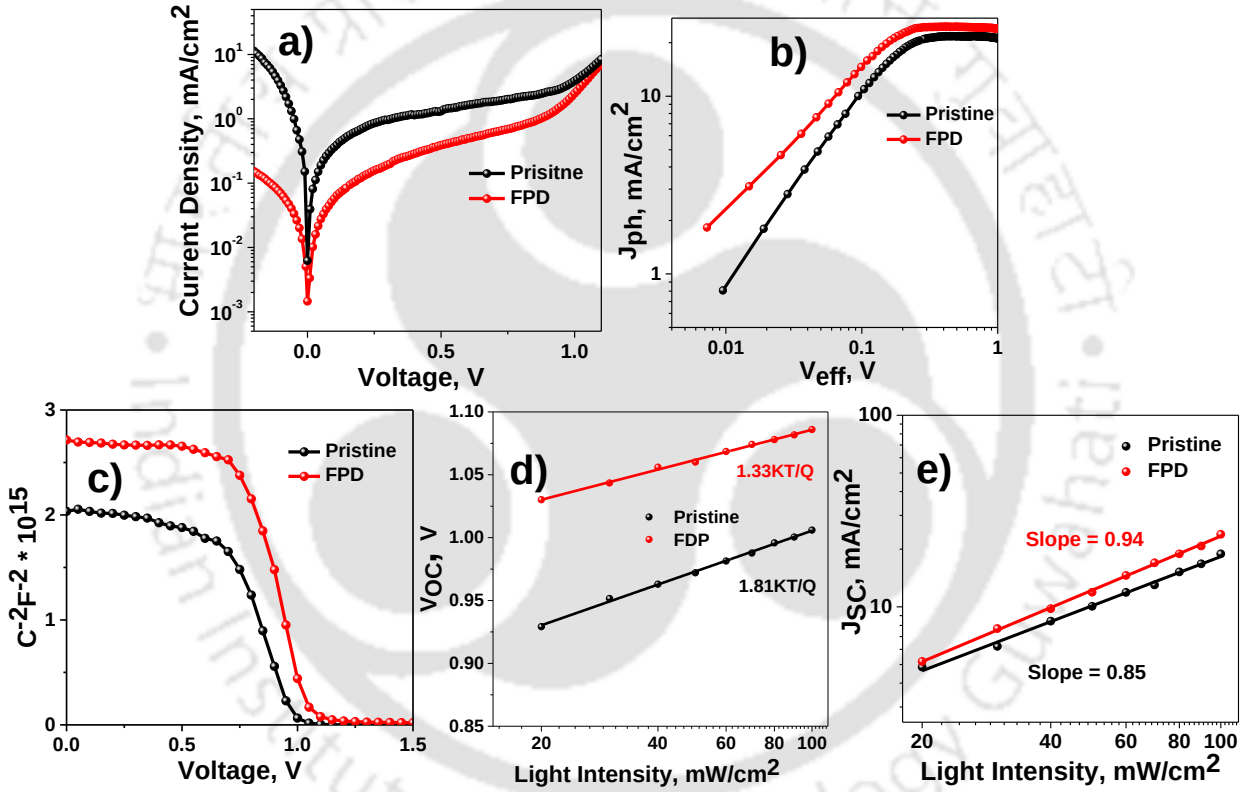

Figure 5.6: a) Dark J–V characteristics of pristine and FPD modified PVSCs b) J_{ph} versus V_{eff} plot, c) Mott–Schottky profile, d) Light intensity versus V_{OC}, and e) Light intensity versus J_{SC} for pristine and FPD passivated PVSCs.

J_{ph} for pristine and passivated devices were gradually increased at lower V_{eff} and reached up to the saturated photocurrent (J_{sat}) at higher V_{eff}. FPD incorporation enhanced the J_{sat} which is generally proportional with generation rate (G_{max}). The relatively higher J_{sat} for passivated device indicates about the better photon absorbance which further validates the

enhanced absorbance profile of passivated perovskite film. This also can be correlated with J_{SC} enhancement for FPD passivated PVSCs compared to pristine counterpart. Moreover, at lower V_{eff} region, relatively sharper rise in J_{ph}-V_{eff} plot was observed for pristine and FPD based PVSCs. At a certain V_{eff}, the J_{ph}/J_{sat} ratio is directly correlated with the transport and collection of charge carriers.[36] The effect of FPD passivation is very evident in trap suppression which significantly assisted smoother charge carrier transport in the PVSCs. To gain better insight about the mechanism behind the V_{OC} enhancement, capacitance−voltage (C−V) measurements were performed. Mott−Schottky profile is presented in Figure 5.6c for pristine and passivated PVSC. The capacitance, C of depletion layer can be presented as a dependent function of the applied bias (V) as

$$\frac{1}{C^2} = \frac{-2}{\varepsilon_0 \varepsilon q A^2 N}(V - V_{\mathrm{bi}}), \qquad (5.3)$$

where ε_0 presents the vacuum permittivity, ε is the relative dielectric constant, A is the device area (0.12 cm^2), V_{bi} is the built-in potential, and N is residual charge density.[37] V_{bi} can be determined by the intercept of the X-axis of the straight line in the curve.[38] FPD passivated device displayed an enhanced built-in potential (V_{bi}) of 1.04 V compared to pristine with 0.96 V. The higher V_{bi} for passivated device signifies the presence of a dominant electric field which can facilitate smoother transport of charge carriers through the interface which also validate the enhanced V_{OC} (1.086 V) for passivated device. The residual charge density (N) was estimated from the slope value of linearly fitted Mott−Schottky graph. The N value was found to be 3.2×10^{16} cm^{-3} for FPD passivated device compared to 4.1×10^{16} cm^{-3} for pristine photovoltaic device. The lower N value for modified device signifies that the passivation minimized the charge carrier recombination and accumulation at the interface. To further study about the recombination kinetics of charge carriers, light intensity depended V_{OC} and J_{SC} were analyzed. V_{OC} can be directly correlated with splitting of the quasi-Fermi levels of charge carriers where quasi-Fermi level is determined by free electron and hole density.[39] The equation between V_{OC} and light intensity (I) is

$$V_{OC} = \left(\frac{nkT}{q}\right)\ln\left(\frac{I}{I_o} + 1\right), \qquad (5.4)$$

where, n presents the ideality factor, k is the Boltzmann constant, and T represents temperature.[31] In light intensity depended V_{OC} profile, the magnitude of n will be close to unity for the devices with very less traps. The slope deviation of kT/q from unity signifies the dominance of trap-assisted monomolecular Shockley−Read−Hall (SRH) recombination.[31] As shown in Figure 5.6d, FPD based device displayed a lowered value of ideality factor (1.33) compared to the pristine device (1.81) which indicates about the dominant bimolecular recombination in passivated device. Contrarily, the dominance of trap-assisted SRH recombination was evident in pristine device. Figure 5.6e displays the light intensity versus J_{SC} profile, where the FPD based device depicts a higher slope of 0.94 compared to pristine counterpart with 0.85, suggesting lesser amount of trap-assisted non-radiative recombination with FPD passivated PVSCs. Light depended V_{OC} and J_{SC} profile indicates that the extent of trap assisted recombination in pristine device is higher which was significantly reduced by FPD incorporation in perovskite layer.

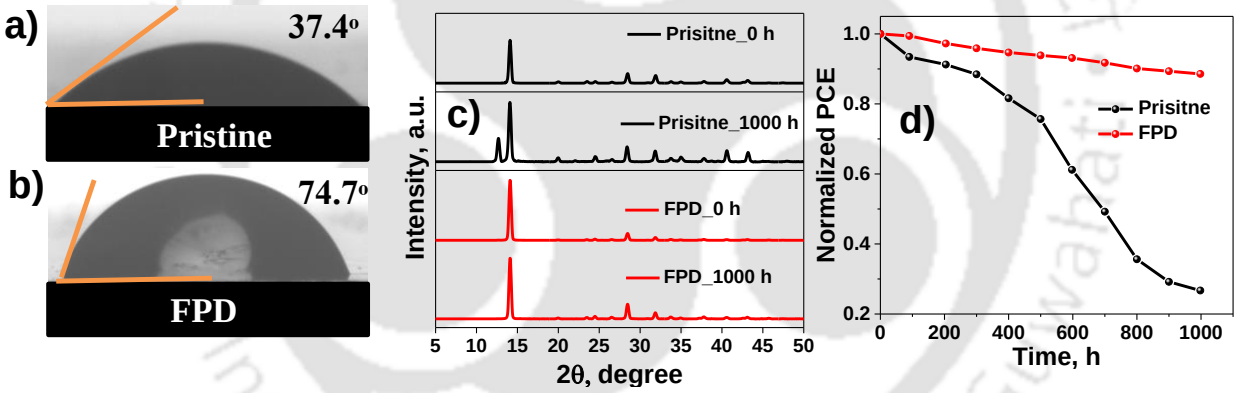

Figure 5.7: Contact angle of a) pristine and b) FPD passivated perovskite films, c) XRD patterns of perovskite films aged in a RH of 45 ± 5%, and d) Normalized efficiency of pristine and FPD passivated PVSCs aged in a RH of 45 ± 5%.

For the comparative analysis of surface hydrophobicity of pristine and FPD passivated perovskite film, contact angle was measured (Figure 5.7a-b). Pristine and FPD modified surface displayed the contact angel of 37.4° and 74.7° respectively. FPD incorporation improved the hydrophobicity of perovskite surface significantly which can resist the moisture penetration during exposure to ambient condition. This can be further validated by XRD study of perovskite films after exposure to ambient condition (RH 45 ± 5%) for 1000 h (Figure 5.7c). Though, FPD modified film displayed almost similar XRD pattern after ambient exposure but for pristine film,

an intense peak of PbI_2 phase at 12.7° was appeared. To understand the passivation effect on long term durability of PVSCs, the passivated and pristine devices were exposed to ambient condition with RH 45 ± 5%. For pristine device, a sharp decrease was observed in all photovoltaic parameters (J_{SC}, $V_{OC,}$ and FF) resulting in steep reduction of PCE in ambient condition and it retained only 27% of its PCE after 1000 h (Figure 5.7d). This decline can be attributed to the presence of PbI_2 phase in pristine film and rapid deterioration of perovskite crystal structure after ambient exposure. Contrarily, the FPD passivated PVSC exhibited stable photovoltaic performance and maintained 89% of its initial efficiency which validates the passivation capability of FPD molecule. FPD based perovskite passivation has significantly improved the photovoltaic performance and operational stability under ambient condition.

5.3 Conclusions

In summary, we have illustrated the impact of incorporating multifunctional additive molecule FPD in perovskite photoactive layer which substantially regulated the optoelectronic property, surface morphology and diminished defects in perovskite lattice structure. The PCE of 15.10% for pristine device was significantly improved up to 20.22% (J_{SC} of 23.97 mA/cm^2, V_{OC} of 1.086 V, and FF of 77.7%) for FPD passivated PVSC. The traps and the defect density in perovskite active layer were considerably suppressed due to the strong interaction between functional groups of FPD and perovskite crystal lattice. Moreover, the long term durability was improved significantly for passivated PVSCs and it retained high efficiency even in high humid conditions for longer periods in comparison to non-passivated device. This FPD passivation approach thus confirmed to be an efficacious method to enhance the PCE along with the long term stability of PVSCs to withstand unfavorable humid conditions.

5.4 Experimental Section

5.4.1 Materials

FTO coated glass substrates (13 Ω sq^{-1}), PbI_2 (99.8%), all anhydrous solvent e.g., DMF, DMSO, Isopropanol (IPA), Toluene, and Chlorobenzene along with Rhodamine 101 inner salt were purchased from Sigma-Aldrich. Methylammonium iodide (MAI) was obtained from Dyesol. Nickel nitrate hexahydrate ($Ni(NO_3)_2 \cdot 6H_2O$) and 5-fluoropyrimidine-2,4(1H,3H)-dione was obtained from TCI. All other chemicals were utilized as received.

5.4.2 NiO_x Film Preparation

NiO_x solution was prepared by dissolving Nickel nitrate hexahydrate and Ethylenediamine (in 1:1 molar ratio) in Ethylene glycol (1 ml). Then, the NiO_x layer was coated as hole transporting layer (HTL) on the cleaned FTO. FTOs were cleaned with detergent and followed by deionized (DI) water, Acetone, and IPA for 15 min for each solvent, then dried and treated with UV-ozone for half an hour. NiO_x precursor solution was spin coated onto the FTO substrates at 3500 rpm for 45 sec. Lastly, the FTOs were annealed at 300 °C for 60 min under ambient condition.

5.4.3 Device Fabrication

The $MAPbI_3$ precursor solution was prepared by mixing 209 mg of MAI, 581 mg of PbI_2 in a solvent mixture of γ-Butyrolactone and DMSO (7:3, v/v) in a glovebox .The solution was heated for 5-6 h at 70 °C. For the passivated device varied concentrations (1.5 mg/ml to 4.5 mg/ml) of FPD were added to the precursor solution. The filtered solution was spin coated on the NiO_x coated FTO in a two-step spin coating process i.e. 750 rpm for 20 sec and 4000 rpm for 60 sec. In the second step, 150 μL anhydrous Toluene was dripped dropwise after 20 sec as anti-solvent and after that the substrates were annealed at 80 °C for 10 min on a hotplate. Then, for both passivated and pristine devices, 12 mg/ml $PC_{61}BM$ solution was coated at 1200 rpm as electron transporting layer (ETL) and again annealed at 80 °C for 5 min on a hotplate. After that a thin layer of Rhodamine 101 inner salt was spin coated at 4000 rpm from a solution of 0.5 mg/ml in IPA. Lastly, silver was thermally deposited by utilizing a shadow mask to obtain the devices with active area of 0.12 cm^2.

5.4.4 Device Characterization

The XRD patterns of the perovskite films were studied using a Rigaku Micromax-007HF diffractometer equipped with Cu Kα1 irradiation (λ = 1.54184 Å). The perovskite films were analyzed by UV-vis absorption spectroscopy (Perkin Elmer Lambda-35) and FTIR spectroscopy (LabRam HR) in ATR mode. The film morphology of the samples were investigated by scanning electron microscopy (SEM, JEOL JSM-7610F). The current density−voltage (*J*−*V*) characteristic curves were recorded utilizing a Keithley 2400 source meter under argon atmosphere by illuminating the device with a solar simulator (AM 1.5G, 100 mW/cm^2, Oriel Sol 3A solar simulator, Newport). The incident external quantum efficiency (EQE) was obtained by using an Oriel IQE-200 instrument under ambient condition. Electrochemical measurements were conducted using a CH Instruments 760D.

5.5 References

(1) Kojima, K. Teshima, Y. Shirai and T. Miyasaka, *J. Am. Chem. Soc*., 2009, **131**, 6050-6051.

(2) M. M. Lee, J. Teuscher, T. Miyasaka, T. N. Murakami and H. J. Snaith, *Science*, 2012, **338**, 643.

(3) D. Zhao, C. Chen, C. Wang, M. M. Junda, Z. Song, C. R. Grice, Y. Yu, C. Li, B. Subedi, N. J. Podraza, X. Zhao, G. Fang, R.-G. Xiong, K. Zhu and Y. Yan, *Nat. Energy*, 2018, **3**, 1093-1100.

(4) Z. Chen, B. Turedi, A. Y. Alsalloum, C. Yang, X. Zheng, I. Gereige, A. AlSaggaf, O. F. Mohammed and O. M. Bakr, *ACS Energy Lett*., 2019, **4**, 1258-1259.

(5) NREL, https://www.nrel.gov/pv/cell-efficiency.html, 2019.

(6) C. Besleaga, L. E. Abramiuc, V. Stancu, A. G. Tomulescu, M. Sima, L. Trinca, N. Plugaru, L. Pintilie, G. A. Nemnes, M. Iliescu, H. G. Svavarsson, A. Manolescu and I. Pintilie, *J. Phys. Chem. Lett*., 2016, **7**, 5168-5175.

(7) D. Xin, S. Tie, R. Yuan, X. Zheng, J. Zhu and W.-H. Zhang, *ACS Appl. Mater. Interfaces*, 2019, **11**, 44233-44240.

(8) X. Zheng, B. Chen, J. Dai, Y. Fang, Y. Bai, Y. Lin, H. Wei, Xiao C. Zeng and J. Huang, *Nat. Energy*, 2017, **2**, 17102.

(9) M. A. Afroz, N. Ghimire, K. M. Reza, B. Bahrami, R. S. Bobba, A. Gurung, A. H. Chowdhury, P. K. Iyer and Q. Qiao, *ACS Appl. Energy Mater*., 2020, **3**, 2432-2439.

(10) R. Garai, M. A. Afroz, R. K. Gupta and P. K. Iyer, *Adv. Sustainable Syst*., 2020, **4**, 2000078.

(11) F. Gao, Y. Zhao, X. Zhang and J. You, *Adv. Energy Mater*., 2020, **10**, 1902650.

(12) K. Choi, H. Choi, J. Min, T. Kim, D. Kim, S. Y. Son, G.-W. Kim, J. Choi and T. Park, *Sol. RRL*, 2020, **4**, 1900251.

(13) C. Hu, Y. Bai, S. Xiao, T. Zhang, X. Meng, W. K. Ng, Y. Yang, K. S. Wong, H. Chen and S. Yang, *J. Mater. Chem. A*, 2017, **5**, 21858-21865.

(14) L. Xie, P. Song, L. Shen, J. Lu, K. Liu, K. Lin, W. Feng, C. Tian and Z. Wei, *J. Mater. Chem. A*, 2020, **8**, 7653-7658.

(15) R. K. Gupta, R. Garai, M. Hossain, A. Choudhury and P. K. Iyer, *ACS Sustain. Chem. Eng*, 2021, **9**, 7993-8001.

(16) M. A. Afroz, R. K. Gupta, R. Garai, M. Hossain, S. P. Tripathi, P. K. Iyer, *Org. Electron*. 2019, **74**, 172-178.

(17) Z. Yang, J. Dou, S. Kou, J. Dang, Y. Ji, G. Yang, W.-Q. Wu, D.-B. Kuang and M. Wang, *Adv. Funct. Mater*, 2020, **30**, 1910710.

(18) Q. Chen, W. Wang, S. Xiao, Y.-b. Cheng, F. Huang and W. Xiang, *ACS Appl. Mater. Interfaces*, 2019, **11**, 27145-27152.

(19) H. Zheng, G. Liu, W. Wu, H. Xu and X. Pan, *J. Energy Chem*., 2021, **57**, 593-600.

(20) S. Zhao, J. Xie, G. Cheng, Y. Xiang, H. Zhu, W. Guo, H. Wang, M. Qin, X. Lu, J. Qu, J. Wang, J. Xu and K. Yan, *Small*, 2018, **14**, 1803350.

(21) J. Yang, C. Liu, C. Cai, X. Hu, Z. Huang, X. Duan, X. Meng, Z. Yuan, L. Tan and Y. Chen, *Adv. Energy Mater*., 2019, **9**, 1900198.

(22) N. A. N. Ouedraogo, H. Yan, C. B. Han and Y. Zhang, *Small*, 2021, **17**, 2004081.

(23) M. Hossain, M. A. Afroz, R. Garai and P. K. Iyer, *Sustainable Energy Fuels*, 2021, **5**, 874-879.

(24) M. Hossain, R. Garai, R. K. Gupta, R. Narasimhan and P. K. Iyer, *J. Mater. Chem. C*, 2021, DOI: 10.1039/D1TC02335G.

(25) R. Garai, R. K. Gupta, A. S. Tanwar, M. Hossain, P. K. Iyer, *Chem. Mater*. 2021, **33**, 5709–5717.

(26) J. L. Grem, *Invest. New Drugs*, 2000, **18**, 299-313.

(27) D. B. Longley, D. P. Harkin and P. G. Johnston, *Nature Reviews Cancer*, 2003, **3**, 330-338.

(28) J. Cao, S. X. Tao, P. A. Bobbert, C.-P. Wong and N. Zhao, *Adv. Mater*., 2018, **30**, 1707350.

(29) R. Azmi, N. Nurrosyid, S.-H. Lee, M. Al Mubarok, W. Lee, S. Hwang, W. Yin, T. K. Ahn, T.-W. Kim, D. Y. Ryu, Y. R. Do and S.-Y. Jang, *ACS Energy Lett*., 2020, **5**, 1396-1403.

(30) J. Cao, B. Wu, R. Chen, Y. Wu, Y. Hui, B.-W. Mao and N. Zheng, *Adv. Mater.*, 2018, **30**, 1705596.

(31) N. Ghimire, R. S. Bobba, A. Gurung, K. M. Reza, M. A. R. Laskar, B. S. Lamsal, K. Emshadi, R. Pathak, M. A. Afroz, A. H. Chowdhury, K. Chen, B. Bahrami, S. I. Rahman, J. Pokharel, A. Baniya, M. T. Rahman, Y. Zhou and Q. Qiao, *ACS Appl. Energy Mater*., 2021, **4**, 1731-1742.

(32) Y. Zhang, P. Wang, X. Yu, J. Xie, X. Sun, H. Wang, J. Huang, L. Xu, C. Cui, M. Lei and D. Yang, *J. Mater. Chem. A*, 2016, **4**, 18509-18515.

(33) X. Hou, S. Huang, W. Ou-Yang, L. Pan, Z. Sun and X. Chen, *ACS Appl. Mater. Interfaces*, 2017, **9**, 35200-35208.

(34) Y. Zhang, S. Chen, H. Chen, G. Zhang, M. Zhao, C. Zhao, W. Guo, W. Ji, Z. Shi and T. Jiu, *J. Mater. Chem. C*, 2020, **8**, 5894-5903.

(35) V. D. Mihailetchi, J. Wildeman and P. W. M. Blom, *Phys. Rev. Lett*., 2005, **94**, 126602.

(36) V. D. Mihailetchi, L. J. A. Koster, J. C. Hummelen and P. W. M. Blom, *Phys. Rev. Lett*., 2004, *93*, 216601.

(37) O. Almora, C. Aranda, E. Mas-Marzá and G. Garcia-Belmonte, *Appl. Phys. Lett*., 2016, **109**, 173903.

(38) W. Zhang, L. Wan, S. Fu, X. Li and J. Fang, *J. Mater. Chem. A*, 2020, **8**, 6546-6554.

(39) A. Rajagopal, P.-W. Liang, C.-C. Chueh, Z. Yang and A. K. Y. Jen, *ACS Energy Lett*., 2017, **2**, 2531-2539.

Chapter 6

Conclusions and Future Prospects

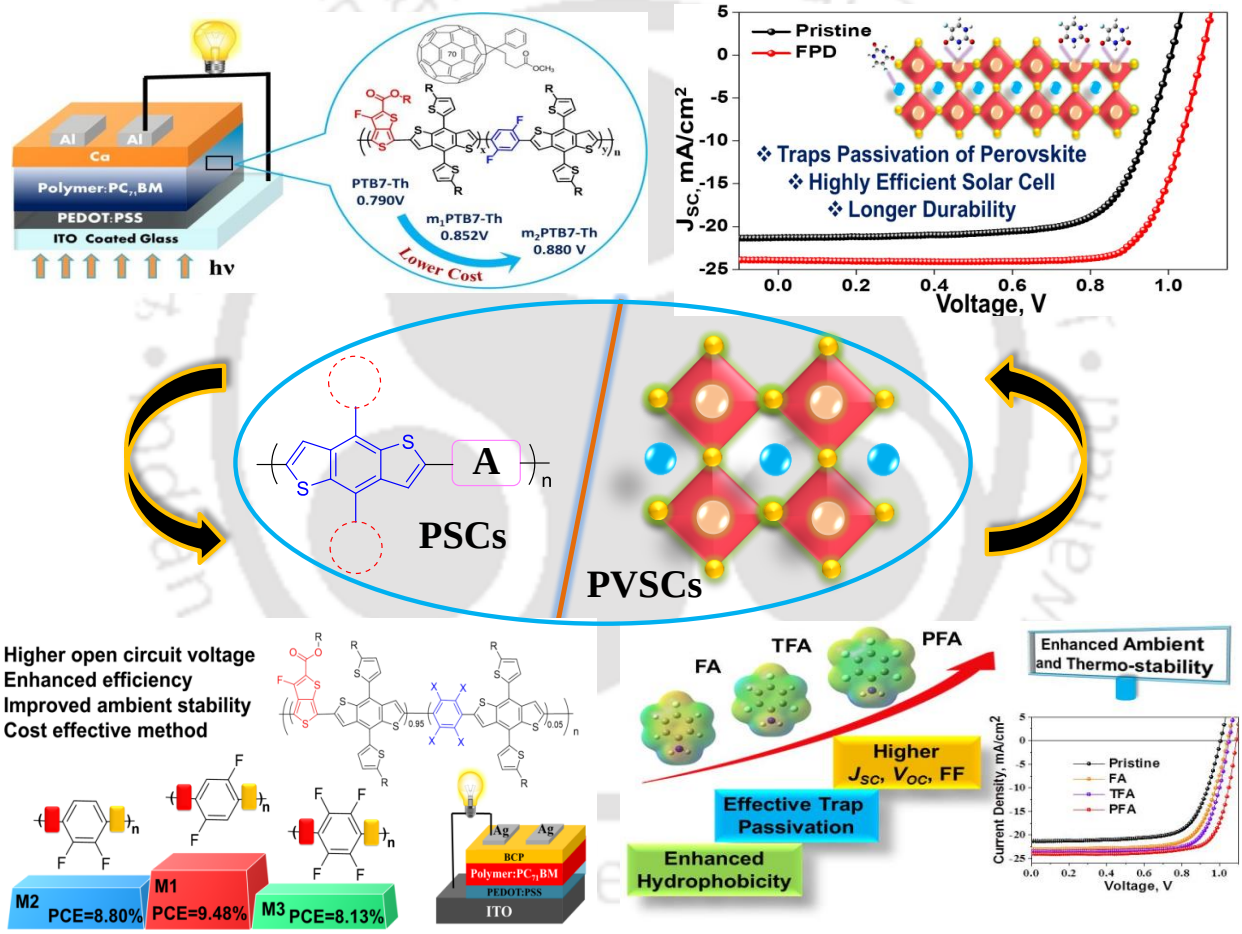

6.1 Conclusions

Amid the continuous upsurge in demand of sustainable energy source in recent time, solar technologies have emerged as the frontrunner to substitute the conventional fossil fuels. The polymer solar cells (PSCs) and perovskite solar cells (PVSCs) have gained incredible attention as one of most promising technology for clean energy revolution. Herein, we have focused on materials and methods to overcome the shortcomings of PSCs and illustrated the structure-property relationship of terpolymers in the first part of the thesis. In next part, the focus was to analyze the crystallization process and trap states of perovskite films to enhance the device performance and stability of PVSCs by the incorporation of multifunctional additives.

The first chapter of this thesis highlighted the rising demand of green energy, a brief history of PSCs and PVSCs development, working principle, their device architectures including its components. Then, varied techniques utilized for the measurement of photovoltaic performance is described. Finally, the methods to modulate the photoactive layer of PSCs and PVSCs are presented.

The second chapter elucidated the impact of third monomer (2,5-difluorobenzene, FBZ) incorporation in PTB7-Th backbone. FBZ incorporation significantly tuned the backbone planarity, energy level alignments and blend morphology. The details of optoelectronic property and photovoltaic performance were analyzed to understand the structure-property relationship of terpolymers.

In third chapter, a comparative study was carried on the impact of three fluoroarenes (2,5-difluorobenzene, 2,3-difluorobenzene, and 2,3,5,6-tetrafluorobenzene) by incorporating them in PTB7-Th backbone. The device performance and ambient stability was studied for the photovoltaic devices. The charge carrier transport and interfacial charge recombination mechanism in the photovoltaic devices were studied. Finally, blend morphology was thoroughly analyzed during 1000 h exposure of ambient condition to understand the impact of fluoroarene in improving morphological stability.

Fourth Chapter focused on the trap passivation of $MAPbI_3$ based solar cells by fluoroarene derivatives. Three fluorinated aromatic amines (4-fluoroaniline, 2,4,6-trifluoroaniline, and 2,3,4,5,6-pentafluoroaniline) were incorporated on the perovskite surface. Pentafluoroaniline

most effectively controlled the recrystallization of perovskite top surface and passivated the traps states. An insight on the crystallization, morphology, charge carrier dynamics, and trap mitigation of perovskite layer has been provided. The ambient and thermal stability was enhanced significantly along with photovoltaic efficiency of passivated PVSCs.

Chapter five demonstrated 5-fluoropyrimidine-2,4(1H,3H)-dione (FPD) assisted trap passivation of PVSCs. The multifunctional additive modulated perovskite crystallization and overall morphology. FPD substantially passivated the trap states in perovskite layer and facilitated the charge transport. The detailed study on how FPD regulated the perovskite formation along with device performance and ambient stability has been presented.

6.2 Future prospects

Extensive studies on PSCs have been conducted on various factors, such as absorption, energy band gap, interfacial contacts and morphology. Different materials and methods were developed to enhance the performance of PSCs. These advancements have stimulated rapid growth of PSCs in last decade. Nevertheless, quite a few challenges persist to further enhance the efficiency and device stability to match the criterion of commercialization.

With regard to the active layer, numerous donor polymers and acceptors have been developed with suitable photovoltaic properties. To further improve efficiency of PSCs, design and development of new materials are essential which can enhance the photon absorption at near IR region and provide well matched energy band alignment. However, till now comparably less effort is made to enhance the long term stability of PSCs. To be commercially viable, both device performance and stability are equally important. Fluorinated fused moieties can be incorporated in donor and acceptor materials to boost the stability of PSCs.

Till now, incredible advancements have been achieved on all fronts for PVSCs. However, the instability of perovskite materials as well as toxicity of lead hinders its progress towards commercialization. For further advancements, the following strategies can be implemented to overcome the present day challenges.

Further enhancements in Power conversion efficiency (PCE) can be obtained by mitigating the charge carrier recombination through trap passivation. Additive engineering for trap passivation can be more useful after having better insight of recombination mechanism in

photovoltaic devices. Structural evolution of additives and insightful analysis of device properties are required for further progress in PCE.

The notorious instability of PVSCs is the major obstacle for its commercialization. This disadvantage can be overcome in two ways; 1) by improving the crystal lattice stability of perovskite materials and 2) by enhancing ambient stability through improving the bonding of cations (MA^+ and FA^+) with PbX_2 and restricting moisture and oxygen penetration by additive engineering. On heating perovskite materials undergoes crystal expansion and its thermal instability is attributed to the weaker bonding between organic ion and inorganic sub lattice. By strengthening the interaction between the organic cations and inorganic ions, the thermal stability can be enhanced significantly. The ambient stability of perovskite materials can be enhanced by introducing hydrophobic additives or by preparing 2D/3D mixed perovskite through incorporation of bigger organic cations. The development of new materials for electron transport layer or hole transport layer can further improve efficiency and stability PVSCs. The fabrication of tandem solar cells using silicon with perovskite materials and suitable encapsulation also can be an effective strategy to boost efficiency as well as long term durability of photovoltaic devices.

Toxicity of lead is another major obstacle for commercialization of oragnolead halide perovskite based photovoltaics. Though, tin (Sn)-based perovskite materials have the potentials to be used in photovoltaic devices, their stability and efficiency is much inferior to the Pb-based perovskites. Some additives like H_3PO_2, SnF_2, and $SnCl_2$ have been explored to improve the stability of Sn-based perovskites. Further study to comprehend Sn-based perovskites might lead to the progress in the performance and stability of Sn-based PVSCs.

In summary, the research work of this thesis illustrates the strategies to design and synthesize terpolymers with finely tuned optoelectronic property to achieve higher device performance as well as longer durability. It also presents the techniques to prepare high quality oragnolead halide based perovskite films with larger grains and mitigated trap states. The purpose of these approaches was to enhance the photovoltaic performance and stability of the device. The observations of these research works can surely motivate the researchers to further explore various dimensions of PSCs and PVSCs to contribute in the quest of affordable green energy for next generation.

Maimur Hossain

Senior Research Fellow
CHEL 304, Department of Chemistry
Indian Institute of Technology Guwahati,
Assam-781039, India
h.maimur@iitg.ac.in, maimur.iitg@gmail.com
+91 9093 287 056, +91 361 258 2339

Education

Indian Institute of Technology Guwahati **Guwahati, Assam**

- **PhD** in Chemistry — March, 2022
  Advisor: Prof. Parameswar K Iyer — (Course work CPI: 8.5)

Aligarh Muslim University **Aligarh, Uttar Pradesh**

- **MSc** in Chemistry — (Percentage: 74.75%, 2015)
- **BSc** in Chemistry — (Percentage: 74.40%, 2013)

Research Experience

Indian Institute of Technology Guwahati **(2015-2021)**

Advisor: Prof. Parameswar K Iyer

Title: Photoactive Layer Modulation for High Performance Polymer and Perovskite Solar Cells.

- Design, synthesis and characterization of new terpolymers for fabrication of **polymer solar cells**.
- Analysis of the impact of fluoroarene incorporation on morphology, device stability and photovoltaic performance of polymer and perovskite solar cells.
- Design and development of additives (**small molecule and polymers**) for perovskite passivation to mitigate the trap and defect states to enhance the stability and photovoltaic performance.
- Development of NiOx, TiO_2, and SnO_2 based transport layers for the fabrication of the optoelectronic devices.
- Analysis of growth and degradation mechanism of halide perovskite grain utilizing FESEM, FETEM, and XRD.
- Development of **2D/3D perovskite** materials.
- Development of **hot-casted** large area perovskite based optoelectronic devices.

Teaching experience

Teaching duty July 2016 – March 2020

Department of Chemistry — Indian Institute of Technology, Guwahati

Course: Organic Chemistry Practical Course, CH 101 — (B.tech, IIT Guwahati)

Organic Chemistry Practical Course, CH 425 — (MSc, IIT Guwahati)

- Guided Two master's projects — 2018-2019, June-August 2018
- Guided Five undergraduate projects — 2016-2017, 2017-2018, 2018-2019

Research Interests

- Perovskite Materials, Conjugated Polymers, Photovoltaics, LEDs and Photodetectors.

Publications

1. Maimur Hossain, Mohammad Adil Afroz, Rabindranath Garai, Parameswar Krishnan Iyer "*Tuning the Open Circuit Voltage by Incorporating a Difluorophenyl Unit into a Polymer Backbone to Achieve High Efficiency Polymer Solar Cells*", ***Sustainable Energy Fuels*, 2021, 5, 874-879.**

2. Maimur Hossain, Rabindranath Garai, Ritesh Kant Gupta, Rahul Narasimhan, Parameswar Krishnan Iyer *"Fluoroarene Derivative based Passivation of Perovskite Solar Cell Exhibiting Excellent Ambient and Thermo-Stability Achieving Efficiency > 20%"*, ***J. Mater. Chem. C,* 2021**, **9, 10406-10413.**

3. Maimur Hossain, Rabindranath Garai, Rahul Narasimhan, Mohammad Adil Afroz, Parameswar Krishnan Iyer *"Backbone Engineering with Fluoroarene to Mitigate Morphological Disorder for High Performance Polymer Solar Cells"*, ***ACS Appl. Polym. Mater. 2021,* XX, XX-XX. *(In Press)***

4. Rabindranath Garai, Ritesh Kant Gupta, Arvin Sain Tanwar, **Maimur Hossain**, Parameswar Krishnan Iyer, "*Conjugated Poly-electrolyte Passivated Stable Perovskite Solar Cells for Efficiency Beyond 20%*", ***Chem. Mater. 2021*, 33, 5709-5717.**

5. Maimur Hossain, Rahul Narasimhan, Rabindranath Garai, Ritesh Kant Gupta,and Parameswar Krishnan Iyer, *"Enhancing Efficiency and Ambient Stability of Perovskite Solar Cells via Multifunctional Trap Passivation Molecule"*, ***J. Mater. Chem. C,* 2021, XX, XX-XX. *(In Press)***

6. Ritesh Kant Gupta, Rabindranath Garai, **Maimur Hossain**, Anwesha Choudhury, and Parameswar Krishnan Iyer, "*Halide Engineering for Mitigating Ion Migration and Defect States in Hot-Cast Perovskite Solar Cells"*, ***ACS Sustainable Chem. Eng.* 2021**, **9, 7993–8001.**

7. Ritesh Kant Gupta, Rabindranath Garai, **Maimur Hossain**, Mohammad Adil Afroz, Dibashmoni Kalita, and Parameswar Krishnan Iyer, *"Engineering Polymer Solar Cells: Advancement in Active Layer Thickness and Morphology"*, ***J. Mater. Chem. C, 2021*, *2021, 9, 8746-8775.***

8. Mohammad Adil Afroz, Ritesh Kant Gupta, Rabindranath Garai, **Maimur Hossain**, Suyashpati Tripathi, and Parameswar Krishnan Iyer, "*Crystallization and Grain Growth Regulation Through Lewis Acid-Base Adduct Formation in Hot Cast Perovskite-based Solar Cells*", ***Org. Electron.*, 2019, 74, 172-178.**

9. Ritesh Kant Gupta, Rahul Narasimhan Arunagirinathan, Mohammad Adil Afroz, Rabindranath Garai, Anwesha Choudhury, **Maimur Hossain**, Ramesh Babu Yathirajula, and Parameswar Krishnan Iyer, "Functional materials for various organic electronic devices", *Chemical Solution Synthesis for Materials Design and Thin Film Device Applications*, ***Elsevier***, **2021**, 119-165. (Book Chapter)

10. Rabindranath Garai, Ritesh Kant Gupta, **Maimur Hossain**, and Parameswar Krishnan Iyer, Surface recrystallized stable 2D–3D graded perovskite solar cells for efficiency beyond 21%", ***J. Mater. Chem.***

***A*, 2021, 9, 26069-26076.**

11. Chandan Dawo, **Maimur Hossain**, Parameswar Krishnan Iyer, and Harsh Chaturvedi, *"Rapid and Low Temperature Processing of Mesoporous TiO_2 Electron Transport Layer for Dye Sensitized Solar Cell on Flexible Substrates"*, ***(About to Submit).***

12. Rahul Narasimhan, **Maimur Hossain**, Ramesh Babu Yathirajula, and Parameswar Krishnan Iyer *"Effect of Coulomb Blockade in Carrier Transport of a Trap Containing Organic Resistive Random Access Memory Devices"*, ***(About to Submit).***

13. Chandan Dawo, **Maimur Hossain**, Parameswar Krishnan Iyer, and Harsh Chaturvedi *"Polyelectrolyte Doped Polyaniline based Counter Electrode for High Performance Dye-Sensitized Solar Cells,"* (***manuscript under preparation***).

14. Chandan Dawo, **Maimur Hossain**, Parameswar Krishnan Iyer, and Harsh Chaturvedi *"Caesium Halide Modified TiO_2 for High Performance Dye-Sensitized Solar Cells"*, (***manuscript under preparation***).

Fellowships & Awards

- Junior and Senior Research Fellowship, Ministry of Human Resource Development, Government of India, 2015-2020.
- "ACS Applied Polymer Materials Best Poster Award", 26th National Symposium in Chemistry / 14th CRSI-RSC Joint Symposium 2020**,** Vellore Institute of Technology, Vellore, India.
- "Institute Best Poster Award", Research Conclave 2019 at IIT Guwahati, Guwahati, Assam.
- Qualified GATE 2015 and CSIR UGC NET 2014 DEC in Chemical Science.

Conferences and Workshops

1. Presented poster in 26th National Symposium in Chemistry / 14th CRSI-RSC Joint Symposium at Vellore Institute of Technology, Vellore, February 6-9, 2020.
2. Attended Anton Paar Workshop on Sophisticated Instruments 2020 at IIT Guwahati, Guwahati, Assam, February 26, 2020.
3. Presented poster in 6th International Conference on Advanced Nanomaterials and Nanotechnology (ICANN 2019), at IIT Guwahati, Guwahati, Assam, Decemeber 18-21, 2019.
4. Presented poster in Research Conclave 2019, at IIT Guwahati, Guwahati, Assam, March 14-17, 2019.
5. Participated in 5th National Workshop on MEMS/NEMS and Theranostic Devices (NWNTD 2019) organized by Centre for Nanotechnology, at IIT Guwahati, Guwahati, Assam, February 21-23, 2019.
6. Participated in 4th National Workshop on MEMS/NEMS and Theranostic Devices (NWNTD 2018) organized by Centre for Nanotechnology at IIT Guwahati, Guwahati, Assam, February 26-28, 2018.
7. Presented poster in International Conference on Advanced Nanomaterials and Nanotechnology (ICANN 2017), at Indian Institute of Technology Guwahati, Assam, December 18-21, 2017.
8. Participated in 3rd National Workshop on MEMS/NEMS and Theranostic Devices (NWNTD

2017) organized by Centre for Nanotechnology at IIT Guwahati, Assam, February 21-23, 2017.

9. Attended Indian Nano-electronics Users Program (INUP-2019) at NIT Silchar, January 28-29, 2019.
10. Attended ACS on Campus at IIT Guwahati, Guwahati, Assam, January 16, 2017.

End